Comparative petrology of silicates in the Udei Station (IAB) and Miles (IIE) iron meteorites: Implications for the origin of silicate-bearing irons

Alex Ruzicka *, Melinda Hutson

Cascadia Meteorite Laboratory, Portland State University, Department of Geology, 17 Cramer Hall, 1721 SW Broadway, Portland, OR 97207-0751, USA

Abstract

The textures and mineral chemistries of silicate inclusions in the Udei Station (IAB) and Miles (fractionated IIE) iron meteorites were studied using optical and electron microscopy, SEM, EMPA, and LA-ICP-MS techniques to better understand the origin of silicate-bearing irons. Inclusions in Udei Station include near-chondritic, basaltic/gabbroic, feldspathic orthopyroxenitic, and harzburgitic lithologies. In Miles, most inclusions can be described as feldspathic pyroxenite or pyroxene-enriched basalt/gabbro. The trace-element compositions of both orthopyroxene and plagioclase grains are similar in different lithologies from Udei Station; whereas in different inclusions from Miles, the compositions of orthopyroxene grains are similar, while those of clinopyroxene, plagioclase, and especially Cl-apatite are variable. Orthopyroxene in Miles tends to be enriched in REE compared to that in Udei Station, but the reverse is true for plagioclase and clinopyroxene.

The data can be explained by models involving partial melting of chondritic protoliths, silicate melt migration, and redox reactions between silicate and metal components to form phosphate. The extent of heating, melt migration, and phosphate formation were all greater in Miles. Silicates in Miles were formed from liquids produced by ∼30% partial melting of a chondritic precursor brought to a peak temperature of ∼1250 °C. This silicate melt crystallized in two stages. During Stage 1, crystallizing minerals (orthopyroxene, clinopyroxene, chromite, and olivine) were largely in equilibrium with an intercumulus melt that was evolving by igneous fractionation during slow cooling, with a residence time of ∼20 ka at ∼1150 °C. During Stage 2, following probable re-melting of feldspathic materials, and after the silicate "mush" was mixed with molten metal, plagioclase and phosphate fractionally crystallized together during more rapid cooling down to the solidus. In Udei Station, despite a lower peak temperature (<1180 °C) and degree of silicate partial melting (∼3–10%), silicate melt was able to efficiently separate from silicate solid to produce melt residues (harzburgite) and liquids or cumulates (basalt/gabbro, feldspathic orthopyroxenite) prior to final metal emplacement. Olivine was generally out of equilibrium with other minerals, but orthopyroxene and plagioclase largely equilibrated under magmatic conditions, and clinopyroxene in basalt/gabbro crystallized from a more evolved silicate melt.

We suggest that a model involving major collisional disruption and mixing of partly molten, endogenically heated planetesimals can best explain the data for IAB and fractionated IIE silicate-bearing irons. The extent of endogenic heating was different (less for the IABs), and the amount of parent body disruption was different (scrambling with collisional unroofing for the IAB/IIICD/winonaite body, more complete destruction for the fractionated IIE body), but both bodies were partly molten and incompletely differentiated at the time of impact. We suggest that the post-impact secondary body for IAB/IIICD/winonaite meteorites was mineralogically zoned with Ni-poor metal in the center, and that the secondary body for fractionated IIE meteorites was a relatively small melt-rich body that had separated from olivine during collisional break-up.
© 2009 Elsevier Ltd. All rights reserved.

---

* Corresponding author. Tel.: +1 503 725 3372; fax: +1 503 725 3025.
  E-mail address: ruzickaa@pdx.edu (A. Ruzicka).

1. INTRODUCTION

The standard conception of differentiation in asteroidal bodies entails the formation of a density-stratified object with a core–mantle–crust structure (e.g., McCoy et al., 2006; Chabot and Haack, 2006). However, this model may not apply to those iron meteorite groups that contain silicate inclusions, of which the IAB and IIE groups are the most prominent examples (Mittlefehldt et al., 1998; Haack and McCoy, 2005). Unlike other iron meteorites that are likely to be samples of cores (Chabot and Haack, 2006), silicate-bearing irons are more enigmatic. Specifically, it is unclear why silicate would not have separated from metal if the latter were molten (e.g., Fish et al., 1960), as textures suggest (e.g., Bunch et al., 1970). The silicate inclusions in IABs and IIEs are highly diverse both within and between the groups, which has complicated their interpretation (Mittlefehldt et al., 1998). However, partial melting and melt migration were important processes for silicate inclusions in both groups (e.g., Bild, 1977; Ikeda and Prinz, 1996; Ikeda et al., 1997; Ebihara et al., 1997; Mittlefehldt et al., 1998; Ruzicka et al., 1999; Benedix et al., 2000; Bogard et al., 2000; Takeda et al., 2000, 2003). IAB irons may have formed on the same parent body as winonaites (Bild, 1977; Benedix et al., 1998, 2000) and the IIICD irons (Choi et al., 1995; Wasson and Kallemeyn, 2002), possibly from a carbonaceous chondrite protolith (Choi et al., 1995; Wasson and Kallemeyn, 2002). The IIE irons form two different subgroups (here referred to as fractionated and unfractionated) based on silicate characteristics (Mittlefehldt et al., 1998; Bogard et al., 2000), although both have similar oxygen isotopic and metal compositions not far removed from H-group chondrites (e.g., Wasson and Wang, 1986; Clayton and Mayeda, 1996; Ebihara et al., 1997). It is uncertain whether the fractionated and unfractionated IIEs formed in a single or multiple parent bodies (e.g., Ruzicka et al., 1999; Bogard et al., 2000).

The nature of the melting process that affected the silicate-bearing irons is uncertain, with both exogenic (impact), endogenic, and hybrid models proposed. The impact models envision the solidification of IAB/IIICD and IIE irons in small impact-melt pools in near-surface environments beneath the regoliths on chondritic parent bodies (Wasson et al., 1980; Wasson and Wang, 1986; Olsen et al., 1994; Choi et al., 1995; Ikeda et al., 1997; Wasson and Kallemeyn, 2002). These models assume the selective formation and mobilization of metallic melts by impact processes. Each iron potentially could have formed in a separate melt pool and impact event, with multiple re-melting and mixing events hypothesized (Wasson and Wang, 1986; Choi et al., 1995; Wasson and Kallemeyn, 2002). Other models assume that endogenic heating was responsible for producing IAB/IIICD irons and the fractionated IIE irons (Wasserburg et al., 1968; Kracher, 1985; McCoy et al., 1993; Bogard et al., 2000). Kracher (1985) proposed that the IAB/IIICD irons represent a partially differentiated, S-rich metallic core with a more primitive outer winonaite layer. According to this model, global temperatures were sufficiently high to create a metallic melt but not to significantly melt silicates. Sulfur-rich metallic melts drained to the center of the parent body. In the case of the fractionated IIEs, the meteorites may have originated by local differentiation in "melt plums" surrounded by chondritic material in the upper portion of a parent body (Wasserburg et al., 1968), or by endogenic heating and mixing of materials within the deep interior of a differentiated parent body (Bogard et al., 2000). Finally, hybrid models involving endogenic heating as well as major collisions have been proposed. For the IABs, collisional disruption and reassembly of the IAB/winonaite parent body during endogenic heating could explain the diversity and textures of inclusions (Benedix et al., 2000) as well as the variable ^{39}Ar–^{40}Ar ages of plagioclase within a given meteorite (Vogel and Renne, 2008). For IIEs, proposed hybrid models include (a) collisional mixing between variably differentiated impactor and target bodies (Casanova et al., 1995; Ruzicka et al., 1999; Hsu, 2003), (b) impact-induced mixing of metallic and silicate melts while the parent body was being endogenically heated (Takeda et al., 2003), and (c) collisional disruption of a warm, partly differentiated parent body with reassembly of molten materials (Ruzicka et al., 2006). This latter model is similar to that proposed by Benedix et al. (2000) for IABs, except that liquids and solids become separated during the parent body disruption process. In all the hybrid models, metal–silicate mixing is induced by an impact process.

To better elucidate the origin of silicate-bearing iron meteorites, we used optical microscopy, scanning electron microscopy (SEM), electron microprobe analysis (EMPA), and laser ablation-inductively coupled plasma-mass spectrometry (LA-ICP-MS) techniques to analyze and compare two silicate-bearing irons representative of contrasting types, namely Udei Station from the IAB group containing Copiapo-type inclusions (Bunch et al., 1970; Benedix et al., 2000, 2005), and Miles from the fractionated IIE group (Ikeda and Prinz, 1996; Ikeda et al., 1997; Ebihara et al., 1997; Hsu, 2003). Our results are considered in the context of previous work on silicate-bearing iron meteorites to derive a unified model for the formation of these meteorites.

2. SAMPLES AND METHODS

We studied four polished thin-sections of Udei Station (Sections CML0264-1A, -1B, -3A, and -3B) created from two slabs that contain six larger silicate inclusions (Udei-1A-1, -2, -3, -1B, -3A, and -3B), two thin slices of Miles (Sections CML0065-3 and -4) prepared from a single, typical fragment that contains 12 small inclusions (Miles-1, -2, -2A, -3, -4, -5, -6, -7, -8A, -8B, -8C, and -9), a thicker slice of Miles (CML0065-5) that contains an unusually large inclusion (Miles-10), and a polished thin-section (CML0065-5B) of the large Miles inclusion. Samples of Miles and Udei Station were obtained from Marvin Killgore and Eric Twelker, respectively.

Optical microscopy and backscattered electron (BSE) imaging was performed at the Department of Geology in Portland State University using a JEOL JSM-35C SEM with a Kevex energy dispersive detector and 4pi digital imaging/spectrum acquisition system. Petrographic data for the inclusions studied are given in Table 1. Modal data for inclusions were obtained by manual point counting, using Adobe Photoshop to lay a grid over the images (see

Table 1
Silicate inclusions in Udei Station and Miles.[a]

Inclusion	Diameter (mm)	Texture
Udei-1A-1	>23	Granular ol, opx, plag, and cpx (~100 μm and up to 250–500 μm across)
Udei-1A-2	2.8 × 3.8	Granular opx and plag (~150–350 μm across), troilite in silicate interstices
Udei-1A-3	5.3	Granular to poikilitic with subhedral–euhedral opx (~100–450 μm) and anhedral plag (~100–900 μm)
Udei-1B	6 × 8	Granular core with equant cpx (~0.1–1.2 mm) and plag (~0.1–1.4 mm)
Udei-3A	24 × 32	Similar to Udei-1A-1
Udei-3B	>10 × >38	Variably textured, including (1) metal- & troilite-poor, feldspar-rich poikilitic area (~2.5-mm diameter plag enclosing 250–750 μm opx) adjacent metal host, (2) granular, troilite-rich "lherzolitic" area (100–500 μm ol and opx, minor plag) [granular #1], and (3) metal-rich "harzburgitic" area (100–1500 μm ol and opx) [granular #2]
Miles-1	0.6 × 6	Subhedral opx–cpx glomerocrysts (~100–200 μm across) and anhedral plag
Miles-2	1.4 × >0.8	opx glomerocrysts (~50–150 μm across); apat and Si-mineral at inclusion edge
Miles-2A	0.75	opx glomerocrysts (~30–150 μm across); plag at inclusion edge
Miles-3	1.4 × 2.6	Subhedral cluster opx and cpx; feldspar, Si-mineral, phos at inclusion edge
Miles-4	1.8 × >4.0	cpx-rich px cluster with plag, Si-mineral, phos at inclusion edge
Miles-5	0.8 × >1.4	cpx–opx cluster with phos, plag, Si-mineral at inclusion edge
Miles-6	9.2 × >3.2	Subhedral opx–cpx glomerocrysts (~150–800 μm across) and anhedral–subhedral plag and Kfeld (200–1100 μm across); segmented inclusion
Miles-7	1.0 × 1.6	Subhedral cpx cluster and anhedral plag
Miles-8A	6.4 × >1.4	Subhedral cpx cluster and anhedral plag
Miles-8B	3.2 × >10	Cpx-rich clusters, often surrounded by plag, with phos and Si-minerals at inclusion edge; segmented inclusion
Miles-8C	2.5 × >2.4	cpx-rich px cluster and adjacent plag, with phos at inclusion edge
Miles-9	1.4 × >0.8	Subhedral plag and anhedral Kfeld, intergrown with adjacent troilite-rich area
Miles-10	13 × >29	Subhedral opx–cpx glomerocrysts (~0.1–1.6 mm across) and interstitial plag (0.1–>3 mm across); phos concentrated at inclusion edge

[a] Diameters approximate, measured in polished sections; ol, olivine; px, pyroxene; opx, orthopyroxene; cpx, clinopyroxene; plag, plagioclase; Kfeld, K-feldspar; phos, phosphate.

Supplementary Section 1 of Electronic Annex for more details). Bulk compositions were calculated using modal reconstruction by combining modal data with measured phase compositions and estimates of mineral densities.

Electron microprobe analyses for major and minor elements were obtained with a Cameca SX-50 for Miles and with a Cameca SX-100 for Udei Station, both housed at Oregon State University in Corvallis, Oregon. Phases were analyzed using quantitative wavelength dispersive EMPA, using well-characterized mineral and glass standards and an accelerating voltage of 15 keV.

Trace elements were analyzed using LA-ICP-MS methods following a procedure similar to that described by Ruzicka and Hutson (2006). Data for olivine, orthopyroxene, clinopyroxene, plagioclase, K-feldspar, phosphate minerals, and inclusion mesostasis were acquired with a Thermo PQ ExCell quadrupole ICP-MS fitted with a New Wave Instruments DUV193 ArF excimer laser in the W.M. Keck Collaboratory for Plasma Spectrometry at Oregon State University. Analyses had a nominal effective spot diameter on the samples of ~80 μm, although spots for Miles-10 were elongate owing to a thick-section that placed the sample above the laser focal plane. Selection criteria were employed to improve the overall quality of the data set by excluding suspect values (see Electronic Annex, Section 1). In CI-normalized plots of trace-element data, the average CI-chondrite abundances of Anders and Grevesse (1989) were used for normalization.

We created a database of mineral/melt partition coefficients (D-values) for 35 elements, which is given in Section 2 of Electronic Annex. Table EA-1 presents D-values for olivine, orthopyroxene, clinopyroxene, plagioclase, phosphate, and chromite. Both averages and standard deviations are tabulated, with the average values used in models and the standard deviation taken to represent the uncertainty in these values.

3. RESULTS

3.1. Mineralogy, textures, and modes

3.1.1. Overall petrography of Udei Station and Miles

Inclusions in Udei Station (hereafter "Udei") range in size and shape, from cm- to mm-sized subangular to subrounded polymineralic inclusions, to smaller, often single euhedral grains (Fig. 1a and b). In Miles, inclusions tend to be small (<1 cm across), although one exceptionally large (nearly ~3 cm long) inclusion with a complex shape (Miles-10) is present (Fig. 1c and d). Inclusions in both meteorites have irregular margins in detail, where mineral grains project into the adjacent metal host. In Udei, metal-rich veins with subequal troilite cross inclusions (Fig. 1a and b). Miles inclusions typically occur along metal grain boundaries, which often form crack-like features filled with weathering products (Fig. 1d). It appears that most if not all of the smaller Miles inclusions physically interconnect: silicates or their likely weathering products are in direct contact between Miles-4 and -5, and between Miles-8A, -8B, and (before sectioning) -8C; and sectioning also suggests that Miles inclusions 1, 2, 2A, 3, and possibly 6 interconnect in the third dimension. As is typical for IAB and IIE irons, troilite is relatively uncommon in Miles and more abundant in Udei (Wasson and Wang, 1986; Choi et al., 1995). In Udei troilite is locally concentrated in silicate inclusions (Fig. 1a). In contrast, schreibersite is more common than troilite in Miles and usually occurs at the edges of inclusions or metal grains.
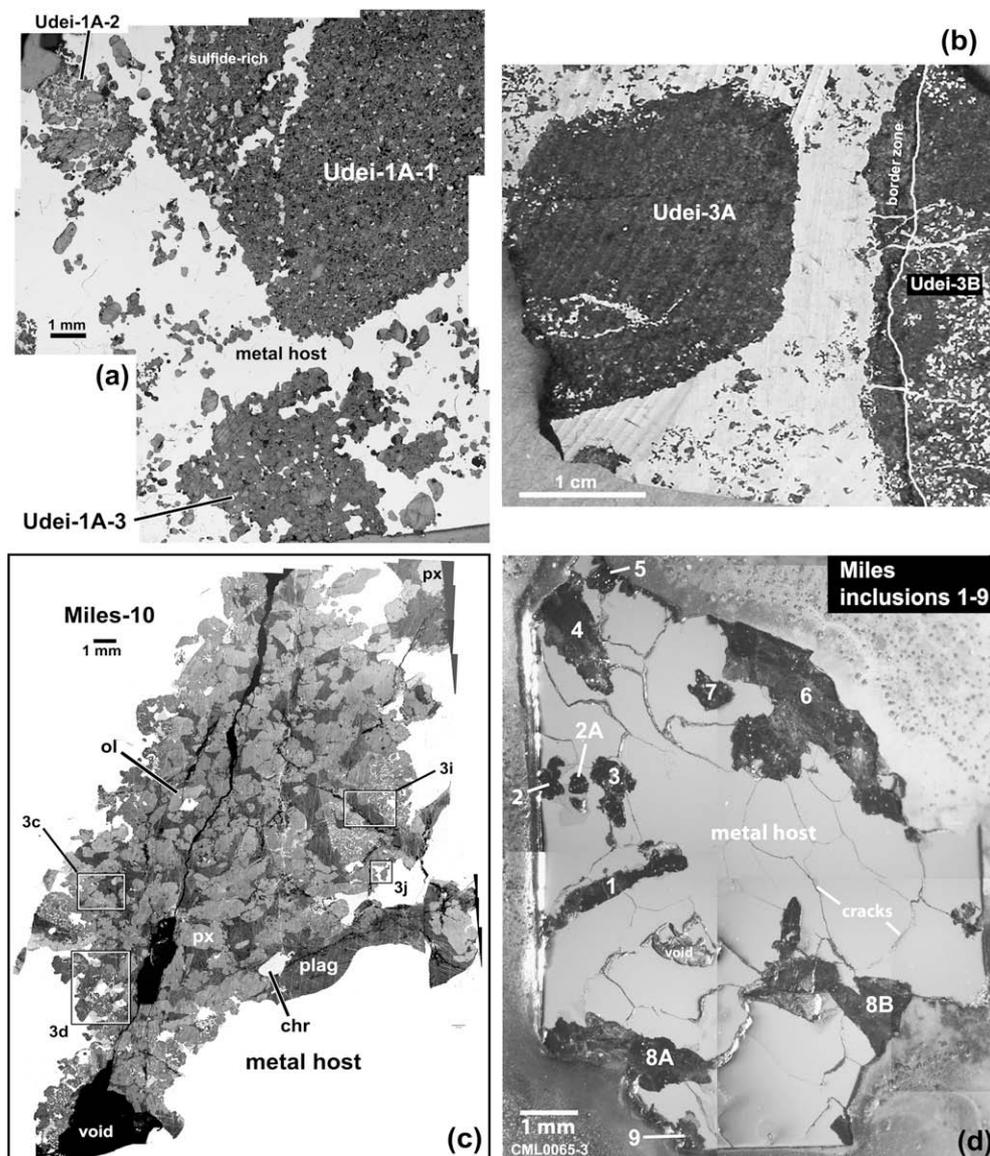
Fig. 1. Images of silicate inclusions in Udei Station (a and b) and Miles (c and d) observed on a large scale. (a) Reflected light image mosaic of a portion of CML0264-1A showing a portion of inclusions Udei-1A-1, -1A-2, and -1A-3, and the many individual grains and grain clumps enclosed in the metal host. Metal appears white, silicates dark grey, and troilite an intermediate grey. (b) Handheld digital camera image showing inclusion Udei-3A and Udei-3B and smaller silicate grains prior to thin-sectioning. Silicates appear dark grey and metal appears white. (c) BSE image mosaic of CML0065-5 showing Miles-10, which is composed primarily of pyroxene (px, including both orthopyroxene and clinopyroxene) and plagioclase (plag). The largest grains of olivine (ol) and chromite (chr) are indicated. Boxes show the locations of close-ups given in Fig. 3c, d, i, and j. (d) Binocular microscope image mosaic of CML0065-3, showing inclusions Miles-1 through -9. Metal appears light grey and silicate inclusions dark. Epoxy is visible around the slice. Cracks in the metal host correspond to metal grain boundaries.

3.1.2. Udei Station inclusions

Inclusions in our samples of Udei have large variations in textures, mineralogy, and modal compositions (Fig. 2 and Tables 1, 2a). Two of the larger inclusions, Udei-1A-1 and Udei-3A (Fig. 1a and b), consist of a relatively fine-grained, granular assemblage rich in olivine (ol), low-Ca pyroxene (opx), plagioclase (plag), and a diopsidic clinopyroxene (cpx) (Fig. 2a). Grain sizes and troilite abundances vary spatially within these inclusions (Fig. 1a). Moreover, some areas within Udei-3A contain pockets of coarser cpx. BSE images and modes were obtained for Udei-1A-1 in the finer-grained, less troilite-rich portion that is typical for the inclusion (Fig. 2a and Table 2a). Triple junctions between minerals are common, suggesting an approach to textural equilibrium.

Inclusions Udei-1A-2 and Udei-1A-3 are distinctly coarser-grained and richer in plag than Udei-1A-1 and Udei-3A (Fig. 2b). Udei-1A-2 has an overall granular texture with obvious triple junctions, and Udei-1A-3 has a texture that varies from granular to poikilitic, with plag grains partly

enclosing opx (Fig. 2b). More troilite is present in Udei-1A-2, where it fills interstices between silicate grains (Fig. 1a). Clinopyroxene grains in near-contact with metal in both inclusions typically have narrow (~1–20-μm wide) selvages of opx that separate metal from cpx (Fig. 2b). This texture was also observed around individual cpx grains enclosed by the metal host and around rare cpx grains in Udei-3B, but was not observed in Udei-1A-1.

Udei-3B is a remarkable inclusion that dramatically varies in texture and mineralogy from one area to another (Table 1). Clinopyroxene is limited to small patches within opx and to two grains that occur on the edge of the inclusion (Fig. 2c). The inclusion has a feldspathic border zone adjacent to the metal host that contains little metal or troilite (Fig. 1b). This border zone has a poikilitic texture, with mm-sized anhedral plag grains that enclose opx grains that
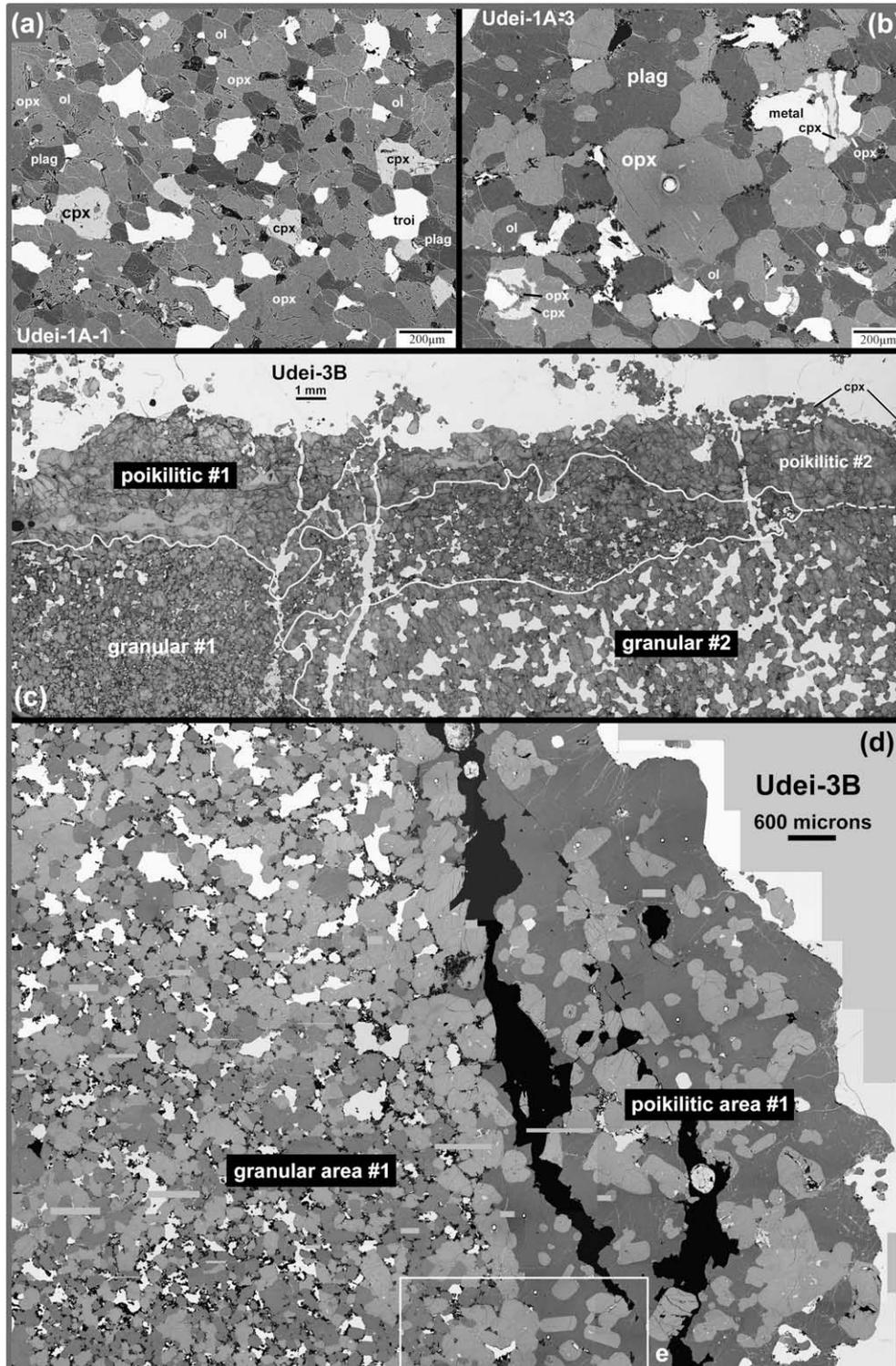
range from euhedral to subhedral (Fig. 2c–e). Some opx grains in the poikilitic area enclose ol grains (Fig. 2e). Modes determined for two representative areas in the poikilitic border zone (poikilitic #1 and #2, Fig. 2c) show that it contains ~40–60 vol% plag and ~37–50 vol% opx, similar to that in Udei-1A-3 (Table 2a). Based on comparisons with norms for various terrestrial rock types (Le Maitre, 1976), these poikilitic areas can be described as feldspathic orthopyroxenite.

In Udei-3B, the feldspathic border zone is in sharp contact with a granular area that is rich in ol and opx (Figs. 1b and 2c–e). At the contact with the poikilitic area, a semi-continuous chain of opx marks the edge of the granular zone (Fig. 2d and e). On one side of the contact, coarse plag in the poikilitic zone is present. On the other in the granular area, plag is much less abundant and occurs as small pockets between other grains, often in contact with troilite (Fig. 2e and f).

Two different granular facies are present in Udei-3B that intergrade slightly and which differ in grain size and modes. One facies ("granular #1") is comparatively fine-grained, troilite-rich, metal-poor, and tends to occur in contact with the poikilitic border (Fig. 2c). Granular #1 is rich in equant ol and opx grains typically ~100–500 μm across, and contains ~2 vol% plag and ~11 vol% troilite (Fig. 2d, e and Table 2a). The overall silicate mineralogy of this facies can be described as that of a plagioclase-bearing harzburgite. The other granular facies in Udei-3B ("granular #2") is comparatively coarse-grained, troilite-poor, metal-rich, and is mostly but not always separated from the poikilitic border zone by the granular #1 zone (Fig. 2c). Granular #2 is rich in equant ol and opx ~0.1–1.5 mm across and contains ~0.2 vol% plag and ~1.5 vol% troilite (Fig. 2f and Table

2a). The mineralogy is that of a harzburgite. Triple junctions between ol and opx grains are especially evident in this facies, as are grains of ol or opx that are fully enclosed within the other phase in a poikilitic or poikiloblastic texture (Fig. 2f).

Another noteworthy feature of Udei-3B is a concentration of graphite in granular #1, where it has an abundance of ~8 vol% (Fig. 2d and Table 2a). Graphite is typically found interstitial to ol, opx, and metal, and intergrown with troilite and plag (Fig. 2e–g). Sometimes it appears as individual elongate grains or laths ~2–20-μm wide and ~20–60-μm long, but usually it appears as aggregates ~40–500 μm across, which often show a radiating or fan-shaped botryoidal texture with convex-outward terminations against troilite (Fig. 2h and i). Troilite locally appears to form "islands" within graphite (Fig. 2g–i), but section re-polishing suggests that island troilite is physically interconnected with adjacent larger troilite areas (Fig. 2i). This implies that graphite and troilite are intergrown in a complex pattern in three dimensions. Graphite crystals or patches also occur within silicate grains, most commonly in plag, less frequently in opx, and rarely in ol (Fig. 2i). In one area, plag is idiomorphic against graphite and troilite but also contains some graphite inclusions (Fig. 2i). Altogether the observations imply some co-formation of graphite with opx and especially with plag, but most graphite formed after most silicates had crystallized. A strong tendency for troilite to be xenomorphic or interstitial to all other phases in Udei-3B, including graphite, implies that it was the last major phase to form.

Inclusion Udei-1B contains clinopyroxene visible as a green mineral in hand specimen and in thin-section viewed under transmitted light. The clinopyroxene is intergrown

Fig. 2. Images showing the textures of inclusions in Udei Station. *Abbreviations:* ol, olivine; opx, orthopyroxene; cpx, clinopyroxene; troi, troilite. (a) BSE image mosaic of Udei-1A-1 showing an overall fine-grained granular texture for silicates and troi. (b) BSE image mosaic for Udei-1A-3 showing a poikilitic texture with anhedral plag enclosing subhedral–euhedral opx. Rare ol is present. At upper right and lower left, thin selvages of opx separate cpx from metal. A laser ablation pit (bright) is visible in the central opx grain. (c) Reflected light image mosaic for Udei-3B showing the contacts between poikilitic areas #1 and #2 and granular areas #1 and #2. Metal appears white, troi a slightly darker light grey, and silicates grey. Metal–troi veins cross-cut all zones and connect to the metal host at top. Minor cpx occurs at the edge of the metal host at upper right. (d) BSE image mosaic for Udei-3B showing drastically different textures between poikilitic and granular areas (image here and in parts (e) and (f) rotated 90° clockwise relative to part (c)). The metal host is at the extreme right edge. Plag is the prominent dark grey phase in the poikilitic area but is too fine-grained and minor to see in the granular area. Opx appears a medium grey and is visible in both the poikilitic and granular portions; ol is visible as a slightly darker shade of grey in the granular area. The large black areas in the poikilitic region are voids produced during sample preparation, whereas the numerous small black areas visible in the granular zone largely correspond to the presence of graphite. The rectangle shows the location of part (e). (e) Closer BSE view of the contact (dashed line) between the granular zone (left) and poikilitic zone in Udei-3B. In the granular zone, small pockets of plag are associated with troi and graphite (black). In the poikilitic area, euhedral–subhedral opx is enclosed by coarse, anhedral plag. Three laser pits (white, with dark edges) are visible in plag near the contact. (f) BSE image mosaic of Udei-3B, showing coarse granular area #2 grading into fine granular area #1 to the right, fining towards the poikilitic zone. Graphite (black) and plag are largely restricted to the finer-grained granular area. White areas are metal grains except for the grains labeled as troilite. The left black arrow shows an example of metal filling interstices between silicate grains. This metal forms one end of a thin (<10 μm) semi-continuous metal vein that "wets" opx and ol grain surfaces, and connects to another metal grain ~1.6 mm distant (right black arrow). (g) SE image showing graphite–troi intergrowths in the Udei-3B granular #1 zone. The rectangle shows the field-of-view for part (h). (h) Reflected light image enlargement of the boxed area from part (g) showing graphite with radiating, fan-shaped textures (arrows point down symmetry axes of fans) as well as an elongate grain. A pit occurs just below the leftmost black arrow in graphite, which marks the location of an area that was plucked during re-polishing following a long EDS analysis at the same location. (i) Reflected light image of Udei-3B showing graphite with botryoidal terminations against troi. The white arrows show intergrowths of graphite with opx; the black arrow shows an idiomorphic projection of plag against graphite. The "i" symbols mark locations of apparent troi islands enclosed in graphite that are interconnected with one another in the third dimension. (j) Cross-polarized transmitted light mosaic of Udei-1B, showing a granular assemblage of cpx and plag. Black areas within and around the inclusion are primarily metal. The inclusion becomes finer-grained towards the upper left. Individual cpx and plag grains project into the surrounding metal.
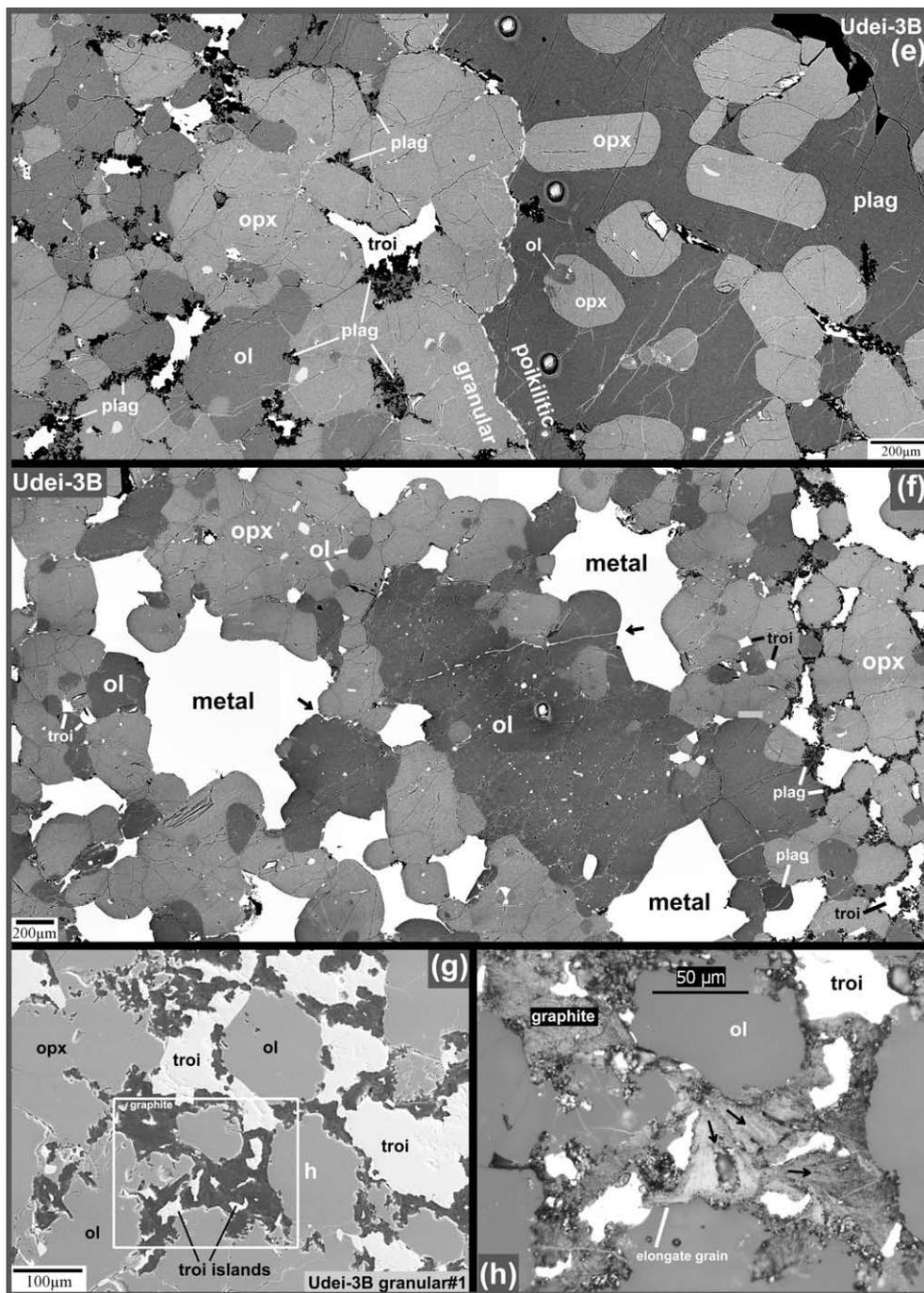
Fig. 2 (*continued*)

with plag in an overall granular texture (Fig. 2j). The grain size is coarsest (∼1 mm across for both cpx and plag) in the core and on one side of the inclusion, and progressively finer-grained towards the other edge (towards the upper left in Fig. 2j). Both plag and cpx grains project into the metal host (Fig. 2j). Triple junctions are common. Much more cpx (∼37 vol%) occurs in this inclusion than anywhere else in the Udei samples that were studied (Table 2a). The mineralogy of Udei-1B is similar to that of basalt or gabbro.

3.1.3. Miles inclusions

Inclusions in Miles generally have a more limited range in texture and mineralogy than inclusions in Udei (Table 1). Most inclusions in Miles are rich in pyroxene and plagioclase, and unlike those in Udei, they sometimes contain K-feldspar, a silica phase that forms elongate grains which is probably tridymite, a mesostasis rich in silica and an alkali feldspar, and one or more phosphate minerals (Table 2b). Olivine is uncommon.
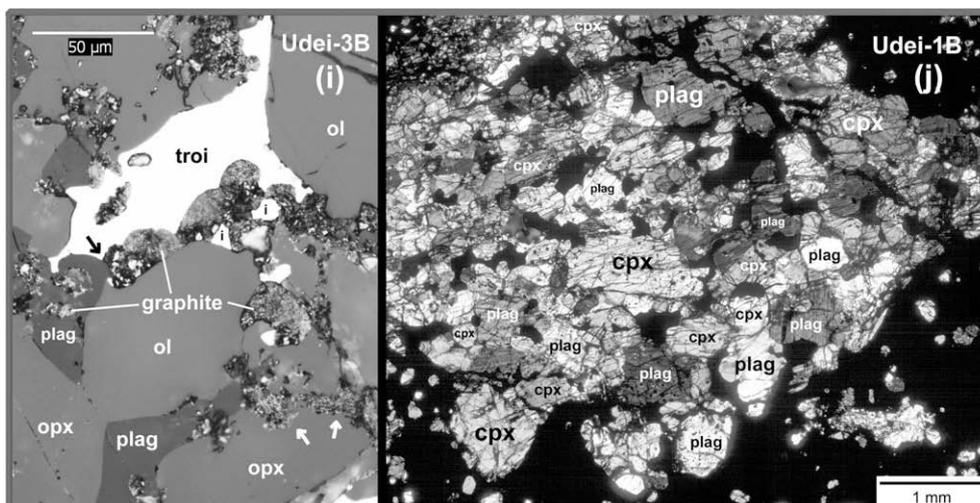
Fig. 2 (*continued*)

Orthopyroxene and clinopyroxene usually show a subhedral texture, with crystal faces well-developed against plag but forming intergrowths with other pyroxene grains to produce a glomerocrystic assemblage of either opx alone, cpx alone, or both opx and cpx (Fig. 3a–c). These glomerocrysts appear to be composed of opx grains ~50–300 μm across, and have cusps between individual opx grains filled by metal at inclusion edges (Fig. 3a–c and j). In Miles-10, some regions close to the metal host contain a distinctive fine-grained assemblage of opx grains that are more substantially enclosed in metal, with this assemblage poikilitically enclosed by coarse plag (Fig. 3i). Clinopyroxene–metal contacts in Miles are relatively uncommon, with cpx almost always separated from metal by opx (Fig. 3d, e, i, and j). Sometimes cpx appears to form overgrowths on opx (Fig. 3a), whereas in other places, opx forms overgrowths on cpx (Fig. 3e).

Olivine was identified and chromite is abundant only in the exceptionally large Miles inclusion, Miles-10 (Table 2b). In this inclusion, ol has euhedral–subhedral textures, forming ol–opx clusters that are surrounded by plag (Fig. 3c), ol grains enclosed in opx, or ol-chromite clusters surrounded by plag. Olivine grains vary in size, from ~200 μm to ~2 mm across (Figs. 1c and 3c). Chromite in Miles-10 is present as irregularly shaped grains up to ~2–3 mm across (Fig. 1c). Other oxide minerals, including ilmenite and rutile, are present in various Miles inclusions. For instance, rutile was identified in fine-grained opx–metal intergrowth areas in Miles-10 (Fig. 3i).

Plagioclase always appears xenomorphic to opx, cpx, and ol in Miles (Fig. 3a–c, e, and i). Plagioclase grains in Miles-10 reach >3 mm across and poikilitically enclose pyroxene glomerocrysts. Grain sizes of plag in other inclusions were not determined, but pyroxene–plag textures in all Miles inclusions appear to be identical. In contrast to opx–metal contacts, plag–metal contacts are usually smooth on a larger scale with no evidence of metal filling plag grain interstices (Figs. 3a, b and 1c).

Phosphate minerals include primarily Cl-apatite as well as merrillite and an unidentified phosphate, all of which oc-

cur adjacent to metal (Fig. 3d). Silica also tends to occur adjacent to metal, at or near inclusion-host contacts (Fig. 3a and e).

Most inclusions in Miles contain a mesostasis rich in alkali feldspar and a silica phase, although it is abundant only in Miles-6 (Fig. 3f and Table 2b). The silica phase forms equant to elongate grains. It is often cross-cut by one or more terrestrial weathering products that are rich in Fe and which appear bright in BSE images (Fig. 3f). Alkali feldspar in mesostasis was much less affected by weathering (Fig. 3f).

Well-formed K-feldspar grains are present in Miles-6 and Miles-9. In the former inclusion, one grain shows crystal faces against mesostasis but appears to be xenomorphic against plagioclase (Fig. 3g). In Miles-9, K-feldspar occurs interstitial to the silica phase and is also present as a ~100–150-μm thick mantle on plag (Fig. 3h).

Most inclusions in Miles have a mineralogy that can be described as being that of a feldspathic pyroxenite or a pyroxene-enriched basalt/gabbro, but the proportions of opx, cpx, and plag in the inclusions vary significantly, and small inclusions have more divergent mineralogies (Table 2b). Among the small inclusions, Miles-2 and -2A consist chiefly of opx and are better described as orthopyroxenites; Miles-5 is rich in Cl-apatite and pyroxene and could be termed a phosphatic pyroxenite. Miles-9, which contains plag, K-feldspar, silica, and silica-alkali feldspar mesostasis, is clearly different; it represents a rhyolitic assemblage.

3.2. Mineral chemistry

Tables 3–5 give the average composition of phases in Udei and Miles as determined by EMPA and LA-ICP-MS. Below we discuss the composition of each phase separately, comparing the data for Udei and Miles, focusing on the results for trace elements as our data for major-element compositions largely agree with previous reports for these meteorites (Bunch et al., 1970; Ikeda and Prinz, 1996; Ikeda et al., 1997). Major- and minor-element mineral chemistry is discussed in more detail in Section 3 of Electronic Annex.

3.2.1. Orthopyroxene

Orthopyroxene grains in Udei ($Wo_{1.5-3.1}Fs_{7.8-10}$) and Miles (mainly $\sim Wo_{2.4-3.3}Fs_{20-23}$) have similar compositions for most elements determined by EMPA (Table 3). For Miles, Wo and Fs values co-vary (Fig. EA-1), often with similar ranges in different inclusions, with less calcic and ferrous opx (down to $Wo_{0.8}Fs_{13}$) occurring adjacent to metal grains, and more calcic and ferrous grains (up to Wo_4Fs_{27}) further from metal or in grain centers. Two-pyroxene thermometry for opx in Udei and Miles yields similar temperatures in the two meteorites (Table 6). The average apparent equilibration temperature for opx in both meteorites is $\sim$960–970 °C, but apparent temperatures range from $\sim$900 to 1100 °C in Udei and $\sim$800 to 1100 °C in Miles (Table 6). Lower inferred temperatures generally correspond to less calcic opx.

Trace-element LA-ICP-MS analyses of opx in Udei and Miles show that average concentrations are higher in Miles for most REE (except Eu), Co, Ga, Rb, Sr, Y, Nb, and Ba (Table 4 and Fig. 4a). Three chemical–textural groups are identified for opx in Miles. The most prevalent group (Group A) occurs for opx not immediately adjacent to metal and is present in all Miles inclusions analyzed for opx. Group A opx is relatively enriched in HREE, Y, Ca, and Cr, and has a well-defined negative Eu anomaly (Fig. 4b). Group B opx is less enriched in the HREE, Y, Ca, and Cr and has a smaller or no Eu anomaly (Fig. 4b). This opx was identified in Miles-10 and occurs within $\sim$100 μm of the metal host or occurs as overgrowths around clinopyroxene close to metal at the edge of the inclusion (Fig. 3e). Judging from microprobe data, Group B opx probably also occurs in other Miles inclusions, but was not analyzed with LA-ICP-MS. A third group (Group C) corresponds to two analyses (GJ and GK) of opx intimately intergrown with fine-grained metal at the edge of Miles-10 (Fig. 3i). Group C opx has especially low abundances of Ca, V, Sr, Y, and

the HREE, and apparently irregular REE patterns (Fig. 4c).

3.2.2. Clinopyroxene

Chemical data for cpx were obtained in several Miles inclusions but for Udei only in the one inclusion in which it is abundant (Udei-1B). Compositions determined by EMPA for cpx in Udei ($Wo_{43-45}Fs_{3.1-3.4}$) and Miles (mainly $Wo_{39-42}Fs_{9.2-12}$) are similar for most elements (Table 3). Two-pyroxene thermometry for cpx in the two meteorites yields similar temperatures (average $\sim$1150 °C, range $\sim$1100–1210 °C) (Table 6). These temperatures are distinctly higher than shown by opx and imply formation of cpx under magmatic conditions.

Although trace-element abundances in cpx from Udei-1B and from Miles overlap for most elements, average Udei cpx is enriched in Sc, V, Y, Zr, and the LREE, and depleted in Sr, Ba, and Eu, compared to average Miles cpx (Fig. 5a and Table 4). Moreover, different trace-element compositions were measured for cpx in different inclusions in Miles. This contrasts with opx in Miles, which has no obvious difference in composition between different inclusions. For example, cpx grains in Miles-3 and Miles-6 are on average enriched in incompatible elements such as Ti, Y, the REE, and Hf compared to cpx in Miles-10 (Fig. 5b). Strontium, Th, and U, although also incompatible in cpx, show an opposite behavior compared to other incompatible elements, being least enriched in Miles-3 cpx and most enriched in Miles-10 cpx (Fig. 5b).

Miles cpx grains are sometimes zoned in certain trace elements between grain cores and rims, related to grain margin proximity as defined by the presence of plag. Clinopyroxene grain interiors ("cores" in grain centers and "mantles" closer to the rims) in Miles-10 show a huge range in abundances for some elements, including Ti, Zr, the REE, Hf, Th, and U (Fig. 5c). In contrast, grain rims

Table 2a
Modal composition of inclusions in Udei Station.[a]

	Udei-1A-1	Udei-1A-3	Udei-1B	Udei-3B poikilitic #1	Udei-3B poikilitic #2	Udei-3B granular #1 (finer)	Udei-3B granular #2 (coarser)
vol%							
Olivine	26.9	3.2	0	0.4	3.4	33.0	29.7
Orthopyroxene	40.7	43.0	0	37.4	49.0	42.3	44.4
Clinopyroxene	6.3	1.7	33.3	0.2	1.1	0.2	<0.1
Plagioclase	16.3	44.8	56.4	59.1	41.4	2.4	0.2
Oxide	0.1	0.1	<0.1	0.0	<0.1	0.1	0.1
Phosphate	0.0	0.2	0.0	0.0	0.0	0.0	0.0
Metal	1.5	5.6	7.6	1.2	2.3	2.6	23.7
Troilite	8.2	1.4	2.6	1.1	0.6	11.4	1.5
Graphite	0.0	0.0	0.0	0.6	2.1	7.9	0.2
Schreibersite	0.0	0.0	0.0	0.0	<0.1	0.0	0.2
	100	100	99.9	100	99.9	99.9	100
Original % voids	5.3	2.9	6.4	13.1	3.3	2.6	0.7
S (μm)	50.6	122.0	80.6	136	88.0	136	83.8
N	11,697	1477	4121	2160	2515	3468	2611
A (mm^2)	30.0	22.0	26.2	40.0	19.5	64.1	18.3

[a] S = grid spacing; N = number of points in principal count; A = area mapped, estimated from $A = N \cdot S^2$. Oxide minerals include chromite and possibly ilmenite. Udei-3B poikilitic #1 is adjacent to Udei-3B granular #1. Mapped Udei-1A-1 and Udei-3B areas represent portions of larger inclusions.
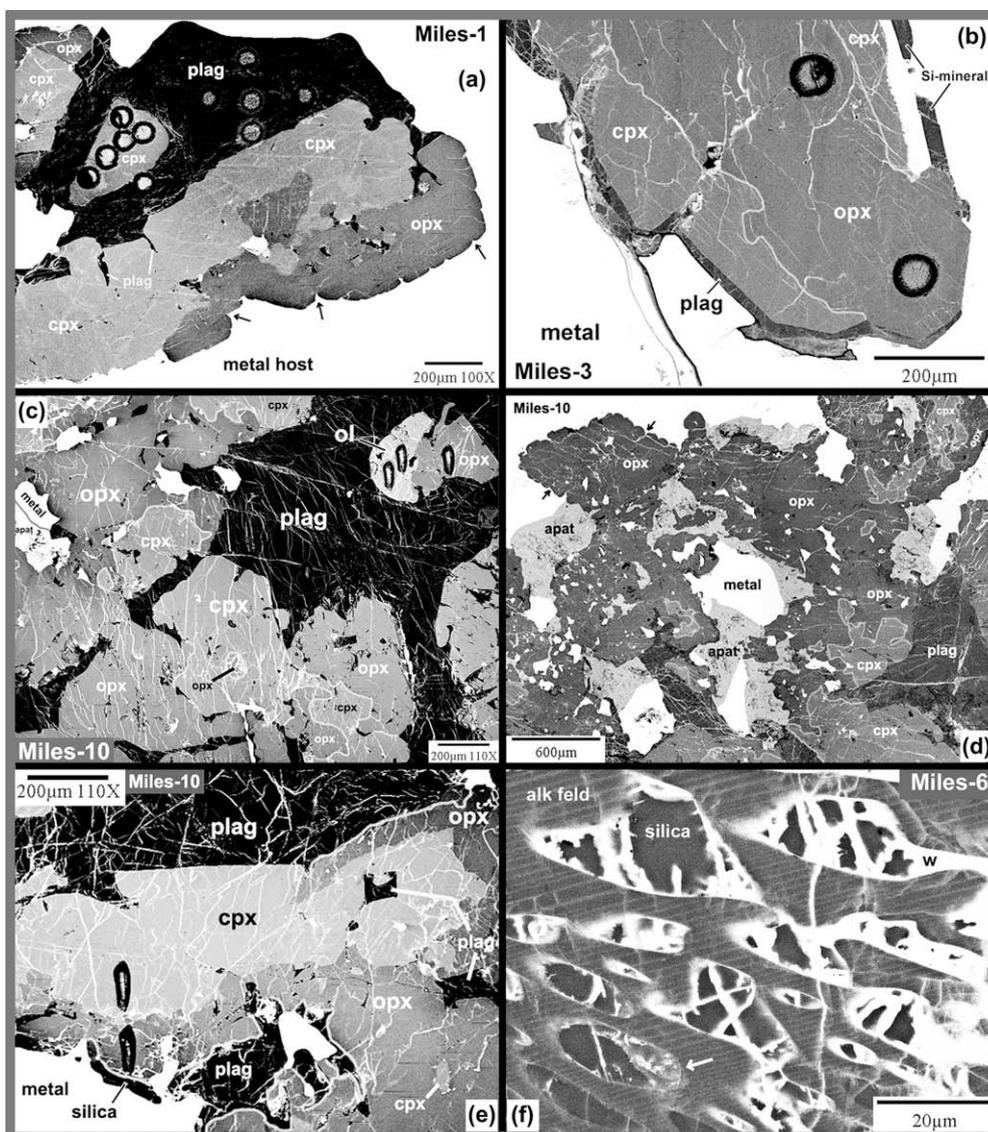
Fig. 3. Images showing the textures of inclusions in Miles. Abbreviations as in Fig. 2 and also "meso", mesostasis; "Kfeld", K-feldspar; "apat", Cl-apatite. (a) BSE image mosaic of a portion of Miles-1 showing anhedral plag with a smooth contact against host metal and subhedral cpx–opx intergrowths with metal filling interstices between opx grains (black arrows). Laser pits are visible in plag and the small cpx grain at left. (b) BSE image mosaic of a portion of Miles-3, showing subhedral cpx overgrowths on opx and a small amount of plag and Si-mineral adjacent to the metal host. Two laser pits are visible. (c) BSE image mosaic of a portion of Miles-10, showing anhedral plag and glomerocrysts of opx–cpx intergrowths as well as one grain of ol at upper right. Three laser pits are visible. (d) BSE image mosaic of a portion of Miles-10, showing apat grains in contact with metal and the presence of opx between cpx and metal. Black arrows at upper left show host metal filling interstices between opx grains. (e) BSE image of Miles-10 showing partial opx overgrowths on subhedral cpx glomerocrysts and an elongate grain of a silica mineral adjacent to metal. Plag is anhedral. Two elongate laser pits are visible, including one in Group B opx adjacent to the silica mineral and metal. (f) BSE image of mesostasis in Miles-6 consisting of a silica phase partly replaced by weathering product (w), both enclosed by a large grain of alkali feldspar ("alk feld") showing exsolution (faint banding from upper right to lower left). The white arrow shows a different, unidentified phase that is intergrown with the silica phase. (g) BSE image mosaic of a portion of Miles-6, showing subhedral glomerocrysts of cpx and opx, anhedral plag, one grain of Kfeld, and inclusion meso. Line A–B, at right edge of image, shows the location of a microprobe traverse (Fig. EA-2b). The dashed line at lower right separates regions of Miles-6 that contain cpx (top) from regions that contain opx (bottom), suggesting that Miles-6 could be a composite inclusion. Miles-7 (7) is at lower left. (h) BSE image mosaic of Miles-9, which contains a plag grain mantled by Kfeld at left, and an area containing meso and intergrown Kfeld and silica mineral (associated with bright weathering products). Rare troi occurs adjacent to the inclusion at the top. Two laser pits are visible. (i) BSE image mosaic of a portion of Miles-10 showing fine-grained intergrowths of opx and metal. The white arrow shows metal partly enclosing opx, with anhedral coarse plag (dark grey) surrounding the opx–metal intergrowths. A single grain of rutile ("rut") is present. Laser pits are visible including those for analyses GJ and GK, which have unusually irregular REE patterns (Group C). Bright lines visible in plag are cracks filled with weathering products. (j) BSE image mosaic showing the edge of Miles-10 and the infilling of opx grain interstices by metal, the separation of cpx from metal by opx (left), and the location of a microprobe traverse (Fig. EA-2a).
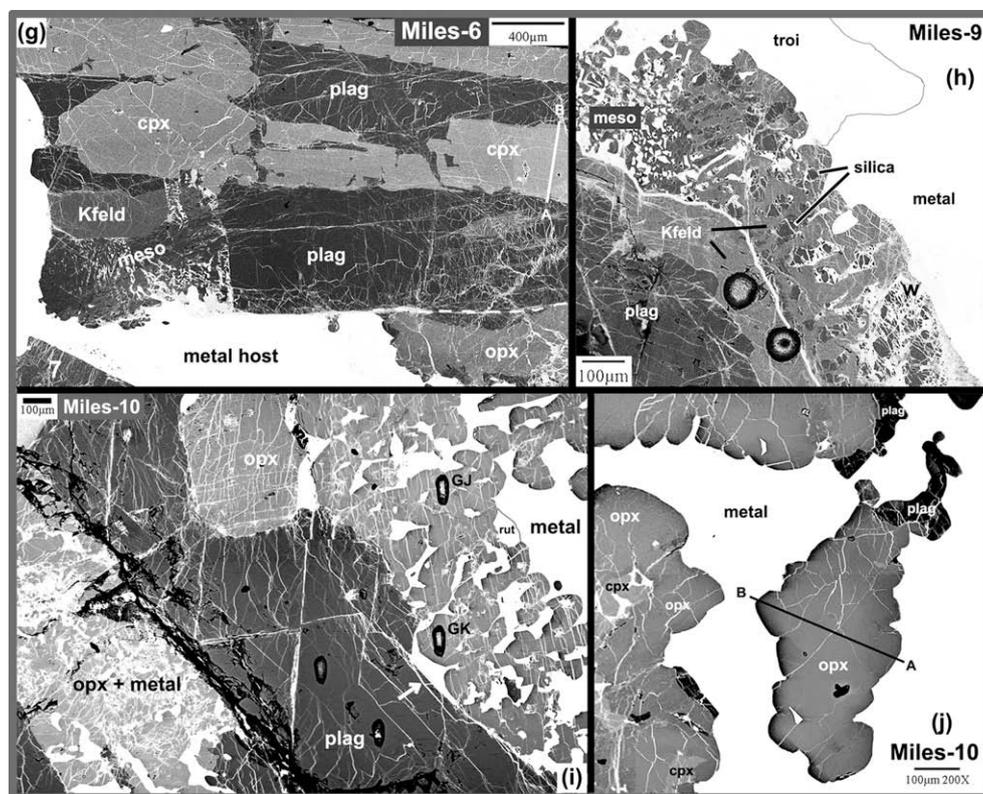
Fig. 3 (*continued*)

(located within ~100 μm of cpx–plag interfaces) in Miles-10 have relatively uniform compositions, with intermediate abundances of Ti, Y, Zr and the REE (Fig. 5c). A cpx grain in Miles-6 that shows core-rim zoning for minor elements (Fig. 3g and EA-2b) also shows evidence for zoning in trace elements (Fig. 5d). The core of this grain is least enriched, and the rim most enriched, in incompatible elements including the REE, Y and Hf (Fig. 5d). Strontium shows the opposite pattern, being most enriched in the grain core (Fig. 5d).

3.2.3. Olivine

Analyses of ol were obtained in inclusions Udei-1A-1 and Udei-3B and Miles-10. Olivine grains in Udei are poor in iron ($Fa_{5.9–8.4}$) compared to those in Miles ($Fa_{13–28}$). Besides iron, Miles olivine is enriched compared to Udei olivine in many minor and trace elements, including Cr, Mn, Sc, Ti, Co, Ga, Rb, Y, Zr, Nb, Ba, Er, Yb, and Lu (Tables 3, 4 and Fig. 6a). REE abundance patterns in ol are relatively flat for both meteorites (Fig. 6a).

3.2.4. Chromite

EMPA and LA-ICP-MS data were obtained for the largest chromite grain in Miles-10 (Fig. 1c). This chromite has variable Cr and Fe contents and is strongly enriched in Cr, V, Ti, Zn, Ga, and Nb compared to other analyzed phases (Tables 3, 5 and Fig. 6b). Given this composition and the ~2.4 wt% chromite present in Miles-10, chromite contains a significant inventory of these elements in the inclusion (i.e., ~70–80% of the Cr and Zn, ~30–40% of

the V and Nb, and ~15–20% of the Ti and Ga). The chromite grain has a relatively flat REE abundance pattern (Fig. 6b).

3.2.5. Plagioclase

Plagioclase in Udei is more anorthitic ($Ab_{78–82}Or_{3.1–3.8}$ $An_{14–19}$) than in Miles (mainly $Ab_{82–97}Or_{2.3–10}An_{1–11}$) (Table 3). In Udei, there is no obvious difference in major-element composition for plag in any of the measured inclusions despite large differences in texture (Fig. 2). In contrast, some Miles inclusions have plag that is more sodic (e.g., $Ab_{96–98}$ in Miles-3) than others (e.g., Ab_{82} in Miles-5). Plagioclase grains in individual Miles inclusions have variable Ab content, with a tendency for plag in different "pockets" separated by pyroxene to have different compositions. The largest measured variations occur in Miles-8A and Miles-8B (range $Ab_{86–97}$) and Miles-10 (range $Ab_{82–94}$).

Trace-element compositions of plag differ significantly between Udei and Miles. Most prominently, average REE abundances are higher in Udei (Fig. 7a). In addition, plag in Udei has lower Co contents, and on average somewhat lower Ga, V, Cr, and Mn abundances and somewhat higher Sr and Ba abundances than plag in Miles (Fig. 7a). The average trace-element composition of plag is related to Ab and An values, with higher REE, Ba, and Sr contents associated with more calcic plag (e.g., as in Miles-10 and in Udei overall), and lower REE contents corresponding to more sodic plag (as in Miles-6 and Miles-3).

Table 2b
Modal composition of inclusions in Miles.[a]

	Miles-1	Miles-2	Miles-2A	Miles-3	Miles-4	Miles-5	Miles-6	Miles-7	Miles-8A	Miles -8B	Miles-9	Miles-10	Miles 1–9 composite
vol%													
Olivine	0.0	0.0	0.0	0.0	0.0	0.0	0.0	0.0	0.0	0.0	0.0	1.2	0.0
Orthopyroxene	38.1	95.9	94.2	29.7	0.0	28.0	38.1	0.0	0.0	6.6	0.0	33.0	24.9
Clinopyroxene	43.7	0.0	0.0	52.8	79.8[b]	46.8	13.7	53.0	45.2	53.7	0.0	25.7	36.9
Plagioclase	13.6	0.1	4.4	14.3	19.7	0.5	30.9	47.0	54.1	36.2	31.0	33.6	28.8
K-feldspar	0.0	0.0	0.0	0.6	0.0	0.0	1.9	0.0	0.2	0.0	37.2	0.1	1.4
Oxide	<0.1	0.0	0.0	0.0	0.0	0.0	0.0	0.0	0.0	0.0	0.0	1.4	<0.1
Phosphate	0.0	1.1	0.0	0.6	0.3	22.8	0.0	0.0	0.0	2.0[c]	0.0	2.1	0.8
Mesostasis	3.1	2.2	0.0	1.3	0.0	0.4	14.9	0.0	<0.1	<0.1	4.8[d]	0.3	6.3
Si-mineral	0.9	0.3	0.0	0.6	<0.1	0.4	<0.01	0.0	0.0	<0.1	27.1[e]	<0.1	0.4
Metal	0.5	0.3	1.4	0.2	0.2	1.1	0.4	0.0	0.5	1.3	0.0	2.6	0.6
	100	100	100	100	100	100	100	100	100	100	100.1	100	100.1
Original % voids	0	1.2	0	2.7	5.3	3.6	0	0.6	1.8	9.0	4.6	5.0	—
S (µm)	52	29.1	17.5	42.1	69.6	25	82.5	45.1	76.0	60.5	21.3	205.5	—
N	1482	1481	1350	1207	1170	1059	2528	636	615	2010	1561	6360	15,099
A (mm²)	4.01	1.25	0.41	2.14	5.67	0.66	17.21	1.29	3.55	7.36	0.71	268.6	44.3

[a] S = grid spacing; N = number of points in principal count; A = area mapped, estimated from $A = N \cdot S^2$; "oxide" includes (mainly) chromite, also ilmenite and rutile; "phosphate" includes chlorapatite (Miles-2, Miles-5, Miles-8B, and Miles-10), merrillite (Miles-8B), and a possibly hydrous phosphate (Miles-3); "mesostasis" includes alkali feldspar + silica, with the latter partly replaced by weathering product.
[b] Mixed ortho-clinopyroxene consisting chiefly of clinopyroxene.
[c] Includes 0.83 vol% chlorapatite + 1.17% merrillite.
[d] Includes alkali feldspar.
[e] Consists of 16.7% unaltered silica + 10.4% of weathering product replacing silica phase.

Table 3
Average composition of phases in Udei Station and Miles, determined by electron probe microanalysis.[a]

	Udei Ol	Miles Ol	Udei Opx	Miles Opx	Udei Cpx	Miles Cpx	Udei Plag	Miles Plag	Miles Kfeld	Miles Alkfeld	Miles Chr	Miles Apat	Miles Merr	Miles Phos	Miles Meso
wt%															
SiO_2	42.6 (0.2)	37.5 (0.82)	58.6 (0.3)	54.4 (0.7)	55.0 (0.1)	53.1 (0.67)	64.8 (0.3)	66.3 (1.6)	63.9 (1.0)	64.7 (2.7)	0.89 (0.66)	n.a.	n.a.	n.a.	78.4 (2.2)
TiO_2	0.01 (0.01)	0.02 (0.01)	0.25 (0.03)	0.32 (0.10)	0.68 (0.05)	0.69 (0.27)	0.06 (0.01)	0.02 (0.03)	0.08 (0.00)	0.03 (0.03)	2.44 (0.16)	n.a.	n.a.	n.a.	0.23 (0.04)
Al_2O_3	0.01 (0.01)	0.01 (0.02)	0.29 (0.02)	0.27 (0.18)	0.86 (0.02)	0.78 (0.16)	22.6 (0.2)	19.7 (0.9)	18.1 (0.0)	18.1 (0.5)	5.44 (0.11)	n.a.	n.a.	n.a.	9.91 (1.68)
Cr_2O_3	0.01 (0.02)	0.25 (0.05)	0.38 (0.03)	0.40 (0.10)	1.24 (0.06)	1.52 (0.18)	<0.01	0.01 (0.05)	0.07 (0.13)	0.01 (0.02)	52.9 (5.8)	n.a.	n.a.	n.a.	0.01 (0.02)
FeO	6.52 (0.60)	19.2 (4.8)	5.49 (0.23)	14.0 (0.5)	2.00 (0.08)	6.34 (0.50)	0.09 (0.08)	1.68 (1.32)	0.96 (0.47)	4.47 (2.88)	29.3 (4.5)	1.84 (1.09)	0.83 (0.37)	4.16 (1.17)	3.39 (1.37)
MnO	0.41 (0.03)	0.61 (0.17)	0.46 (0.03)	0.61 (0.05)	0.28 (0.03)	0.34 (0.04)	<0.01	<0.01	<0.01	<0.01	0.69 (0.06)	n.a.	n.a.	n.a.	0.01 (0.01)
MgO	51.0 (0.6)	41.7 (3.9)	34.2 (0.3)	28.2 (0.6)	17.9 (0.4)	16.6 (0.48)	0.01 (0.01)	0.17 (0.28)	0.02 (0.02)	0.11 (0.10)	6.76 (0.91)	0.13 (0.05)	3.69 (0.04)	5.23 (0.12)	0.03 (0.02)
CaO	0.02 (0.01)	<0.01	1.08 (0.18)	1.43 (0.17)	21.3 (0.4)	19.0 (0.3)	3.35 (0.21)	1.05 (0.73)	0.02 (0.02)	0.32 (0.18)	0.03 (0.05)	48.8 (1.2)	43.2 (0.4)	39.3 (1.6)	0.18 (0.03)
Na_2O	<0.01	<0.01	0.04 (0.01)	0.13 (0.06)	0.70 (0.03)	0.88 (0.18)	8.79 (0.11)	10.2 (0.8)	1.12 (0.20)	7.12 (1.24)	0.06 (0.03)	0.24 (0.02)	2.60 (0.10)	2.30 (0.10)	4.31 (0.81)
K_2O	<0.01	0.01 (0.01)	<0.01	0.01 (0.01)	<0.01	0.01 (0.00)	0.57 (0.05)	0.63 (0.35)	14.8 (0.5)	4.68 (1.85)	0.03 (0.00)	n.a.	n.a.	n.a.	2.20 (0.41)
P_2O_5	n.a.	n.a.	n.a.	n.a.	n.a.	n.a.	n.a.	n.a.	n.a.	n.a.	0.04 (0.05)	40.5 (0.6)	46.7 (0.2)	39.9 (0.7)	0.02 (0.01)
Cl	n.a.	n.a.	n.a.	n.a.	n.a.	n.a.	n.a.	n.a.	n.a.	n.a.	0.01 (0.02)	5.20 (0.41)	<0.01	0.04 (0.00)	<0.01
F	n.a.	n.a.	n.a.	n.a.	n.a.	n.a.	n.a.	n.a.	n.a.	n.a.		<0.01	<0.01	<0.01	n.a.
	100.6	99.3	100.8	99.8	100.0	99.1	100.3	99.8	99.1	99.5	98.6	96.7	97.0	90.9	98.69
mol%															
Fa	6.70 (0.65)	20.6 (5.6)													
Wo			2.03 (0.34)	2.78 (0.32)	44.6 (0.9)	40.1 (0.9)									
En			89.9 (0.4)	76.1 (0.9)	52.1 (0.8)	49.1 (0.8)									
Fs			8.10 (0.33)	21.1 (0.9)	3.27 (0.13)	10.4 (0.8)									
Ab							80.0 (0.9)	91.0 (4.7)	10.3 (1.9)	68.6 (11.5)					73.5 (2.9)
Or							3.43 (0.32)	3.74 (2.23)	89.5 (2.0)	29.6 (12.0)					24.8 (3.0)
An							16.8 (1.0)	5.22 (3.70)	0.11 (0.12)	1.75 (1.08)					1.70 (0.30)
N	14	15	44	328	5	351	41	167	30	13	2	7	3	2	9

[a] Ol, olivine; Opx, orthopyroxene; Cpx, clinopyroxene; Plag, plagioclase; Kfeld, K-feldspar; Alkfeld, alkali feldspar; Chr, chromite; Apat, chlorapatite (average in Miles-2, -5, and -8B); Merr, merrillite in Miles-8B; Phos, phosphate in Miles-3; Meso, alkali feldspar + Si-polymorph mesostasis in Miles-6 (average of defocused beam analyses [20-μm diameter spots] in Fe-poor, less weathered areas). n.a. = not analyzed, N = number of analyses. Standard deviation of mean given in parentheses; when no number is shown, only one datum was used for the mean.

Table 4
Average composition of olivine, pyroxene, and plagioclase in Udei Station and Miles, determined by LA-ICP-MS analysis.[a]

	Udei Ol	Miles Ol	Udei Opx	Miles Opx all	Miles Opx A	Miles Opx B	Udei Cpx	Miles Cpx all	Miles Cpx 1–9	Miles Cpx 10	Udei Plag	Miles Plag all	Miles Plag 1–9	Miles Plag 10
Al (wt%)	0.0070 (0.0064)	n.a.	0.163 (0.010)	n.a.	n.a.	n.a.	0.507 (0.019)	n.a.	n.a.	n.a.	12.1 (0.3)	n.a.	n.a.	n.a.
Si (wt%)	19.90[b] (0)	n.a.	27.39[b] (0)	n.a.	n.a.	n.a.	25.70[b] (0)	n.a.	n.a.	n.a.	30.27[b] (0)	n.a.	n.a.	n.a.
Ca (wt%)	0.0154 (0.0071)	0.0277 (0.0083)	0.834 (0.108)	0.967[b] (0.279)	1.08[b] (0.18)	0.634[b] (0.217)	14.9 (0.6)	13.4[b] (0.5)	13.4[b] (0.4)	13.2[b] (0.6)	2.51 (0.19)	0.824[b] (0.594)	0.415[b] (0.356)	1.31[b] (0.43)
Sc (µg/g)	3.04 (0.52)	6.88 (1.91)	12.1 (1.0)	13.0 (4.9)	12.4 (4.1)	16.7 (6.9)	71.5 (5.7)	57.4 (8.8)	61.2 (7.4)	50.6 (6.9)	1.06 (0.40)	1.24 (0.72)	1.03 (0.83)	1.48 (0.45)
Ti (mg/g)	0.0276 (0.0038)	0.115 (0.033)	1.30 (0.07)	1.53 (0.56)	1.58 (0.57)	1.19 (0.46)	3.60 (0.27)	3.05 (1.44)	3.61 (1.49)	2.04 (0.51)	0.335 (0.018)	0.333 (0.112)	0.293 (0.127)	0.380 (0.068)
V (µg/g)	10.1 (1.2)	10.6 (2.0)	61.8 (5.5)	54.4 (18.9)	57.3 (15.8)	48.5 (28.0)	347 (51)	279 (34)	287 (34)	264 (30)	0.558 (0.335)	1.44 (1.79)	1.85 (2.29)	0.887 (0.348)
Cr (mg/g)	0.0841 (0.0210)	0.173 (0.051)	2.44 (0.11)	2.93 (1.02)	3.29 (0.79)	1.76 (0.87)	7.67 (0.32)	10.5 (1.5)	10.8 (1.3)	10.1 (1.7)	0.0058 (0.0101)	0.0467 (0.0674)	0.0705 (0.0922)	0.0252 (0.0135)
Mn (mg/g)	2.94 (0.10)	4.82 (1.33)	3.37 (0.05)	3.22 (1.01)	3.29 (1.05)	2.98 (0.99)	2.06 (0.12)	2.24 (0.46)	2.11 (0.52)	2.45 (0.22)	0.0088 (0.0091)	0.0301 (0.0396)	0.0347 (0.0423)	0.0252 (0.0344)
Co (µg/g)	2.55 (0.72)	61.1 (44.1)	3.26 (0.37)	88.9 (104.1)	95.4 (113.2)	44.6 (25.3)	1.44 (0.60)	83.9 (79.6)	96.1 (91.8)	63.1 (48.2)	1.57 (1.27)	111 (78)	127 (82)	83.1 (62.2)
Zn (µg/g)	n.a.	143 (21)	n.a.	119 (35)	121 (35)	108 (40)	n.a.	38.9 (7.7)	41.3 (7.1)	34.5 (6.9)	n.a.	2.12 (2.14)	2.54 (2.68)	1.62 (1.13)
Ga (µg/g)	0.119 (0.018)	0.571 (0.217)	0.783 (0.087)	1.38 (0.47)	1.42 (0.44)	1.19 (0.68)	1.91 (0.45)	2.14 (0.53)	2.26 (0.51)	1.93 (0.51)	10.5 (0.7)	18.3 (8.7)	18.5 (11.0)	17.9 (4.8)
Rb (ng/g)	32.6 (14.8)	833 (375)	119 (87)	620 (456)	613 (422)	702 (665)	192 (263)	779 (669)	713 (474)	886 (905)	8748 (866)	15,450 (25,230)	17,170 (33,840)	13,390 (6320)
Sr (µg/g)	0.0536 (0.0391)	0.104 (0.073)	0.0653 (0.0337)	0.534 (0.641)	0.537 (0.652)	0.631 (0.749)	6.61 (0.28)	9.57 (2.33)	9.03 (1.40)	10.5 (3.2)	112 (4)	68.3 (40.9)	39.0 (20.7)	103 (30)
Y (ng/g)	16.2 (11.7)	169 (132)	796 (114)	1835 (1093)	2234 (873)	490 (342)	24,650 (1230)	18,750 (6340)	21,030 (6420)	14,640 (3540)	64.2 (49.1)	44.2 (36.9)	37.6 (26.8)	51.5 (45.1)
Zr (µg/g)	0.0535 (0.0355)	0.507 (0.318)	2.58 (0.62)	2.28 (1.33)	2.60 (1.28)	1.22 (0.64)	29.4 (14.2)	10.5 (7.0)	11.8 (7.3)	8.25 (6.14)	0.242 (0.120)	0.172 (0.190)	0.141 (0.226)	0.212 (0.124)
Nb (ng/g)	7.7 (4.0)	29.3 (25.7)	17.0 (8.1)	41.3 (38.4)	44.4 (41.9)	23.9 (12.7)	133 (45)	138 (133)	147 (120)	126 (152)	27.9 (20.5)	28.6 (36.4)	31.1 (47.3)	25.6 (16.5)
Cs (ng/g)	n.a.	46.8 (19.4)	n.a.	78.0 (44.4)	84.4 (44.9)	69.5 (42.1)	n.a.	169 (177)	222 (199)	73.8 (48.4)	n.a.	522 (741)	737 (914)	236 (201)
Ba (ng/g)	27.6 (21.5)	145 (77)	22.5 (20.2)	266 (209)	229 (178)	434 (292)	79.0 (67.5)	364 (356)	416 (409)	264 (192)	33,920 (1702)	28,840 (14,720)	17,610 (7850)	42,320 (8160)
La (ng/g)	6.0	23.7 (8.3)	13.8 (8.5)	21.0 (15.7)	19.6 (13.1)	22.0 (16.2)	1959 (278)	1211 (746)	1480 (748)	723 (440)	1026 (335)	163 (110)	79.9 (43.7)	264 (75)
Ce (ng/g)	4.1	36.4 (33.0)	12.6 (8.7)	65.8 (57.3)	65.2 (56.7)	58.2 (45.8)	7695 (555)	5293 (3084)	6323 (3071)	3428 (2114)	1189 (400)	251 (158)	132 (86)	394 (90)
Pr (ng/g)	2.5 (0.3)	8.0 (4.4)	6.5 (4.9)	13.4 (8.2)	14.3 (8.7)	10.2 (6.1)	1446 (106)	1031 (569)	1222 (565)	684 (388)	82.9 (39.6)	21.3 (14.2)	13.3 (9.8)	30.0 (13.2)

Table 4 (*continued*)

	Udei Ol	Miles Ol	Udei Opx	Miles Opx all	Miles Opx A	Miles Opx B	Udei Cpx	Miles Cpx all	Miles Cpx 1–9	Miles Cpx 10	Udei Plag	Miles Plag all	Miles Plag 1–9	Miles Plag 10
Nd (ng/g)	34.7	53.8	30.2	80.9	88.0	55.0	8589	6171	7226	4262	289	90.9	60.3	121
	(15.4)	(26.2)	(23.6)	(54.7)	(56.8)	(38.5)	(604)	(3129)	(3127)	(2087)	(116)	(68.1)	(67.2)	(55)
Sm (ng/g)	40.5	47.1	48.6	58.3	64.3	29.0	3121	2331	2649	1757	107	47.9	37.3	58.5
	(10.8)	(17.7)	(28.5)	(29.8)	(28.6)	(11.4)	(429)	(984)	(997)	(655)	(52)	(32.2)	(20.2)	(39.1)
Eu (ng/g)	5.1	8.7	9.9	6.5	5.9	9.0	97.1	125	119	136	863	497	289	745
	(2.9)	(7.4)	(3.6)	(3.8)	(3.1)	(7.8)	(25.9)	(30)	(21)	(40)	(131)	(292)	(159)	(209)
Gd (ng/g)	27.9.	23.3	58.9	124	140	54.7	3829	3177	3592	2428	133	52.6	37.0	72.8
	(20.5)	(10.1)	(25.9)	(64)	(58)	(35.5)	(137)	(1196)	(1213)	(715)	(74)	(45.6)	(27.0)	(57.5)
Tb (ng/g)	2.2	4.9	10.9	27.8	32.7	8.8	695	551	622	424	7.81	3.0	2.6	4.6
	(0.2)	(1.9)	(5.6)	(14.9)	(11.9)	(6.1)	(65)	(200)	(203)	(115)	(2.82)	(1.6)	(1.3)	(1.8)
Dy (ng/g)	20.5	22.6	103	251	303	75.9	4554	3828	4297	2979	51.0	14.9	15.2	14.6
	(12.6)	(9.7)	(34)	(137)	(101)	(54.0)	(430)	(1333)	(1359)	(748)	(23.6)	(5.9)	(7.6)	(3.8)
Ho (ng/g)	5.3	5.7	34.8	67.5	81.3	21.2	917	786	885	605	10.2	2.9	2.3	4.1
	(4.6)	(3.1)	(10.6)	(39.0)	(31.4)	(19.0)	(86)	(279)	(285)	(147)	(5.4)	(1.5)	(1.5)	(0.6)
Er (ng/g)	8.0	39.1	116	250	301	86.7	2306	2128	2380	1672	27.0	10.3	5.4	18.0
	(2.3)	(15.0)	(22)	(140)	(112)	(61.1)	(258)	(720)	(741)	(386)	(13.9)	(7.7)	(2.3)	(6.9)
Tm (ng/g)	2.3	11.4	28.2	46.8	56.2	16.7	317	299	335	233	9.1	3.9	2.6	5.7
	(0.2)	(4.3)	(9.4)	(25.0)	(18.9)	(11.2)	(38)	(101)	(104)	(52)	(3.6)	(2.5)	(1.8)	(2.3)
Yb (ng/g)	20.1	88.5	228	369	449	106	1992	1899	2117	1504	39.5	12.8	9.6	17.5
	(11.3)	(79.7)	(54)	(205)	(153)	(46)	(196)	(619)	(632)	(346)	(18.8)	(5.8)	(4.6)	(3.8)
Lu (ng/g)	6.7	20.6	39.0	66.9	78.0	24.1	296	269	298	215	12.5	3.5	3.3	3.7
	(3.9)	(13.4)	(12.9)	(31.8)	(24.1)	(16.9)	(51)	(88)	(91)	(47)	(7.3)	(2.2)	(2.0)	(2.8)
Hf (ng/g)	n.a.	22.5	n.a.	69.4	70.7	75.5	n.a.	423	529	258	n.a.	10.5	8.4	14.3
		(19.0)		(70.8)	(78.8)	(31.1)		(287)	(313)	(122)		(5.3)	(4.1)	(5.4)
Th (ng/g)	n.a.	—	n.a.	10.8	12.4	6.6	n.a.	31.7	31.3	32.5	n.a.	30.4	30.4	—
				(11.6)	(13.9)	(4.3)		(34.8)	(2.6)	(50.1)		(40.3)	(40.3)	
U (ng/g)	n.a.	8.0	n.a.	8.9	5.9	26.9	n.a.	6.8	4.6	11.6	n.a.	2.6	2.6	—
		(2.8)		(10.0)	(6.6)			(7.9)	(2.8)	(12.3)		(0.9)	(0.9)	
N	9	11	20	41	32	7	5	59	38	21	25	55	30	25

[a] Abbreviations same as in Table 4. Miles Cpx 1–9 and Miles Plag 1–9 refer to averages for Miles inclusions 1, 2, 2A, 3, 4, 5, 6, 7, 8A, 8B, and 9, whereas Miles Cpx 10 and Miles Plag 10 refer to averages for Miles-10.

[b] Concentration normalized to that obtained by EMPA.

Table 5
Average composition of K-feldspar, mesostasis, chromite, and phosphate in various inclusions from Miles, determined by LA-ICP-MS analysis.[a]

	Miles Kfeld Incl 6,9	Miles Meso Incl 6	Miles Chr Incl 10	Miles Apat Incl 2	Miles Phos Incl 3	Miles Apat Incl 5	Miles Apat Incl 8B	Miles Merr Incl 8B	Miles Apat Incl 10
Ca (wt%)	0.141 (0.045)	0.130[b] (0)	0.00215	35.7[b] (0)	28.1[b] (0)	34.9[b] (0)	34.1[b] (0)	30.9[b] (0)	39.3[b] (1.2)
Sc (µg/g)	2.27 (1.02)	2.61 (0.52)	7.27 (0.52)	0.266 (0.077)	26.7 (0.3)	0.615 (0.215)	0.156 (0.198)	13.5 (0.5)	0.0767 (0.0329)
Ti (µg/g)	510[b] (11)	893 (80)	13,970 (570)	63.9 (6.8)	109 (1)	93.0 (17.9)	67.8 (6.7)	110 (0)	24.3 (3.7)
V (µg/g)	1.17 (0.31)	0.533 (0.065)	2477 (8)	0.174 (0.034)	4.24 (0.35)	0.476 (0.312)	0.222 (0.025)	4.54 (0.25)	0.482 (0.270)
Cr (µg/g)	5.54 (4.68)	4.84 (1.06)	541,040 (6700)	5.54 (0.90)	41.2 (0.8)	3.88 (1.86)	6.80 (2.19)	41.0 (6.4)	20.4 (7.9)
Mn (µg/g)	6.79 (4.57)	7.53 (10.67)	5365[b] (0)	150 (15)	175 (1)	199 (25)	204 (8)	198 (31)	488 (87)
Co (µg/g)	96.4 (66.9)	289 (430)	47.9 (51.5)	105 (19)	202 (86)	131 (166)	66.0 (49.1)	43.6	64.3 (40.1)
Zn (µg/g)	1.71 (0.44)	1.41 (1.29)	6784 (858)	0.819 (0.442)	2.05 (0.24)	0.570 (0.403)	0.405 (0.131)	2.55 (0.17)	0.546 (0.150)
Ga (µg/g)	56.5 (19.3)	14.6 (1.8)	81.8 (54.5)	0.229 (0.037)	1.78 (0.47)	0.676 (0.449)	0.403 (0.254)	1.22 (0.95)	0.336 (0.225)
Rb (µg/g)	762 (248)	71.7 (12.0)	0.267 (0.138)	0.249 (0.071)	1.45 (0.05)	0.327 (0.354)	0.277 (0.231)	0.937 (0.094)	0.171 (0.187)
Sr (µg/g)	51.4 (24.4)	13.2 (1.1)	0.117 (0.040)	151 (9)	52.3 (0.4)	180 (8)	191 (5)	65.2 (7.4)	187 (13)
Y (ng/g)	21.9 (7.2)	30.7 (10.7)	273 (238)	35,110 (1177)	176,340 (1640)	157,880 (3840)	42,260 (5680)	346,510 (24,460)	73,820 (9980)
Zr (µg/g)	0.968 (1.822)	6.60 (1.83)	6.82 (1.12)	3.06 (0.08)	0.335 (0.011)	8.61 (2.32)	6.64 (0.10)	0.280 (0.121)	4.67 (1.11)
Nb (ng/g)	32.6 (25.0)	41.1 (1.3)	1099 (76)	67.9 (25.5)	42.7 (2.2)	122 (40)	102 (14)	74.9 (2.8)	9.40 (3.18)
Cs (µg/g)	1.78 (1.10)	0.610 (0.311)	0.161 (0.050)	0.0667 (0.0224)	0.0919 (0.0111)	0.0706 (0.0556)	0.0718 (0.0554)	0.173 (0.130)	0.0275 (0.0173)
Ba (µg/g)	25.5 (13.0)	6.37 (0.79)	0.276	1.11 (0.81)	1.01 (0.22)	2.04 (1.67)	0.815 (0.324)	0.413 (0.192)	1.54 (0.86)
La (ng/g)	60.1 (25.5)	10.7 (1.2)	52.4 (24.2)	8854 (395)	65,060 (1650)	81,640 (3170)	33,630 (5500)	153,580 (9940)	39,010 (8960)
Ce (ng/g)	75.1 (29.1)	15.2 (8.6)	192 (134)	16,920 (590)	154,660 (3880)	195,640 (8940)	70,220 (12,710)	378,940 (26,270)	93,430 (21,820)
Pr (ng/g)	30.2 (34.6)	10.9 (7.2)	34.6 (19.9)	1774 (46)	17,840 (550)	25,600 (1010)	8501 (1434)	50,350 (4200)	11,830 (2810)
Nd (ng/g)	25.5 (3.0)	15.3 (1.8)	132 (11)	6414 (279)	61,600 (1920)	112,020 (4190)	36,290 (6260)	212,260 (19,570)	49,010 (12,020)
Sm (ng/g)	39.7 (9.0)	28.8 (6.0)	114	1419 (93)	16,070 (160)	27,140 (1070)	7865 (1098)	51,840 (4290)	12,400 (2602)
Eu (ng/g)	389 (201)	81.4 (9.9)	19.9 (11.7)	1444 (87)	3156 (131)	1566 (72)	1667 (147)	3081 (0)	1747 (222)
Gd (ng/g)	34.3 (18.2)	31.2 (15.3)	94.0 (45.2)	2667 (135)	18,730 (1220)	32,960 (1100)	11,230 (1320)	62,430 (5230)	13,300 (2320)
Tb (ng/g)	6.1	1.5	13.1 (9.8)	447 (15)	3468 (194)	4899 (179)	1405 (122)	9750 (858)	2226 (365)
Dy (ng/g)	9.3 (1.9)	4.8 (0.5)	115 (119)	3460 (83)	26,300 (1050)	30,480 (1150)	8891 (599)	63,130 (4800)	14,760 (2310)
Ho (ng/g)	2.8 (0.4)	4.5	28.4	885 (31)	5936 (376)	6036 (232)	1714 (114)	12,450 (1260)	3003 (424)
Er (ng/g)	7.9 (5.9)	—	47.6	2977 (109)	18,980 (1350)	15,590 (700)	4090 (323)	32,850 (3070)	8213 (1157)
Tm (ng/g)	3.5 (1.2)	2.7	7.0 (3.3)	494 (19)	3124 (200)	1928 (74)	436 (30)	4118 (434)	1132 (154)
Yb (ng/g)	12.0 (1.6)	6.6	75.0 (2.7)	2536 (48)	26,810 (2060)	9869 (366)	1714 (90)	21,740 (2430)	6935 (798)
Lu (ng/g)	3.1 (1.6)	3.8 (0.7)	12.6 (6.3)	642 (29)	3630 (205)	1290 (68)	262 (10)	2731 (315)	972 (125)
Hf (ng/g)	61.1 (77.5)	224 (59)	135 (68)	18.4 (18.0)	11.4	50.8 (40.7)	17.5 (9.0)	27.8 (5.4)	29.1 (13.0)
Th (ng/g)	17.2 (12.2)	84.1 (23.5)	—	5177 (477)	1659 (490)	7977 (2126)	11,350 (1330)	7410 (1200)	2335 (594)
U (ng/g)	5.1 (2.2)	4.0 (0.5)	28.3	2765 (179)	211 (20)	1980 (98)	1897 (222)	162 (11)	1036 (178)
N	8	6	3	3	2	7	4	2	11

[a] Abbreviations same as in Table 4. Incl, inclusion.
[b] Concentration normalized to that obtained by EMPA.

Table 6
Apparent two-pyroxene equilibration temperatures (in °C).[a]

	Udei Station[b]	Miles[c]
Orthopyroxene		
Mean ± s.d.	958 ± 46	967 ± 95
Range	$900 - 1105$	$800 - 1090$
Clinopyroxene		
Mean ± s.d.	1142 ± 36	1168 ± 31
Range	$1110 - 1190$	$1100 - 1213$

[a] Based on Lindsley (1983) and Lindsley and Andersen (1983). Temperature estimates are probably precise to ±10 °C. s.d., standard deviation of mean.
[b] Based on 5 clinopyroxene and 28 orthopyroxene EMP analyses.
[c] Based on averaged EMPA data for separate inclusions (353 clinopyroxene and 328 orthopyroxene analyses).

3.2.6. K-feldspar and mesostasis

Potassic feldspars and mesostasis were analyzed in Miles. K-feldspar has a relatively well-defined major-element composition with an average composition of $\sim Ab_{10}Or_{90}$ and only ~ 0.02 wt% CaO (Table 3). A different alkali feldspar mineral ("antiperthite"; Ikeda et al., 1997) is found together with a silica phase in inclusion mesostasis and has a composition of $\sim Ab_{65-80}Or_{20-35}An_2$ (Table 3).

Although the antiperthite was too fine-grained to analyze with LA-ICP-MS, trace-element data were obtained for both K-feldspar and bulk mesostasis (Table 5). These data reveal similar abundance patterns with low concentrations for most trace elements, although some elements (Ga, Sr, Cs, Ba, Eu, and especially Rb) are concentrated in K-feldspar (Table 5 and Fig. 7b). Mesostasis is less enriched in these elements, and only the nominally quadrivalent Ti, Zr, Hf, and Th are significantly enriched in mesostasis compared to K-feldspar (Fig. 7b). Most likely the silica phase is enriched in Ti, Zr, Hf, and Th.

3.2.7. Phosphate

Chlorapatite is a relatively common accessory mineral in Miles, although one grain identified as merrillite was found in Miles-8B, and another grain that is neither apatite nor merrillite and that gives a low total (~ 91 wt%) with microprobe analysis was found in Miles-3 (Table 3). The latter phase may be hydrated and was possibly affected by terrestrial weathering, although other phosphate grains are cut by weathering veins and are not significantly hydrated.

All of the analyzed phosphates are enriched in the REE, but they have various REE patterns (Fig. 7c). This includes LREE-enriched patterns with a negative Eu anomaly that deepens as overall REE content increases (Miles-8B merrillite and apatite, Miles-5 and Miles-10 apatite); a "W-shaped" pattern with a positive Eu anomaly at lower overall abundances (Miles-2 apatite); and a "V-shaped" pattern with low Eu and middle REE (MREE) abundances (Miles-3 phosphate). Apatites in Miles-2 and possibly Miles-8B show an apparent negative Yb anomaly whereas a possible positive Yb anomaly occurs in Miles-3 phosphate (Fig. 7c). Despite large chemical differences between phosphate in different inclusions, individual phosphate grains have well-defined compositions, and different apatite grains in Miles-10 have similar compositions to one another (Fig. 7c). Phosphate grains in Miles evidently record different formation conditions local to the inclusions in which they reside.

3.3. Bulk inclusion compositions

Bulk compositions of inclusions in Udei Station and Miles are given in Tables EA-2a and EA-2b, respectively, and CI-normalized abundances are shown in Fig. 8a and c. These compositions correspond to areas for which modes were determined (Tables 2a and b) and are presented on a metal- and sulfide-free basis. All inclusions have low Co contents that undoubtedly reflect significant partitioning of this element into co-existing metal. All inclusions in which the elements were measured also have relatively low abundances of Nb, Hf, and Zr, which could indicate that these elements are concentrated in Ti-oxide (such as ilmenite or rutile) or silica phase excluded in the modal reconstructions.

3.3.1. Udei Station

Udei Station inclusions vary dramatically in composition, as one might expect based on the large variations in modes. For example, the granular areas in Udei-3B have strong depletions in the LREE, and low abundances of Al, Ca, Ga, Rb, Sr, and Ba (Fig. 8a), reflecting their plag- and cpx-poor character. In contrast, the poikilitic areas in Udei-3B (poik #1 and poik #2) and inclusion Udei-1A-3 have abundance patterns that resemble one another and which reflect abundant feldspar, including a large positive Eu anomaly, LREE-enrichments, and high abundances of Sr and Ba (Fig. 8a).

Inclusion Udei-1A-1 (Fig. 2a) has a relatively unfractionated abundance pattern, with most elements present at abundances of $\sim 1.5-2 \times$ CI-chondrites (Fig. 8a). The only exceptions to this are Co, Ga, V, Cr, and Rb. Cobalt and Ga are partly partitioned into metal, so depletions of these elements in the silicate-portion of Udei-1A-1 are not surprising. Moreover, V and Cr are both concentrated in chromite (Fig. 6b), and Rb is strongly concentrated in K-feldspar (Fig. 7b), so an undercount of these phases in the inclusion (only a portion of which was mapped) can explain the apparent depletion of these elements as well. Thus, Udei-1A-1 can be considered to be roughly chondritic in composition, although it has a small positive Eu anomaly and a small enrichment in Ba and Sr (Fig. 8a). This probably reflects a small excess of feldspar in the mapped area for the inclusion.

Inclusion Udei-1B (Fig. 2j) is enriched in most incompatible elements compared to other Udei inclusions (Fig. 8a). The REE pattern is relatively flat at $\sim 5-9 \times$ CI-chondrites and has no Eu anomaly, although it is noticeably enriched for the MREE (Fig. 8a). Other elements such as Al, Ca, Sr, Y, and Ba are similarly enriched. The overall composition and mineralogy of Udei-1B is similar to that of FeO-poor and Na-rich gabbro in Caddo County (Takeda et al., 2000), making Udei the second known IAB that contains such material.
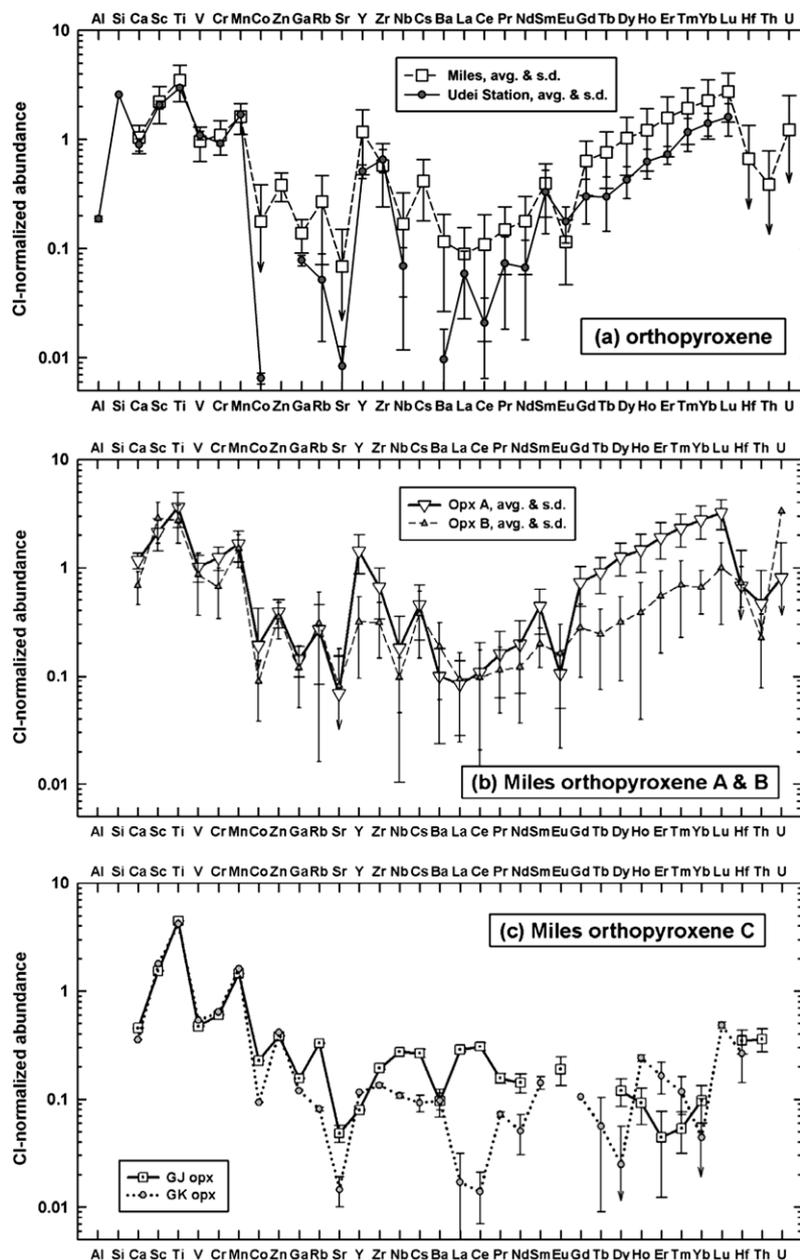
Fig. 4. CI-normalized abundances for orthopyroxene measured by LA-ICP-MS. (a) Average orthopyroxene in Miles and Udei Station. (b) Average Group A and B orthopyroxene in Miles. (c) Group C orthopyroxene in Miles. avg, average; s.d., standard deviation of the mean (shown by bars in parts (a) and (b)). Error bars in part (c) refer to 1σ uncertainties based on counting statistics.

3.3.2. Miles

Fig. 8b and c show compositions for selected small inclusions in Miles, the large inclusion Miles-10, and a composite of all of the smaller inclusions (Miles 1–9). The compositions of the small inclusions differ dramatically from one another, but that of the composite and large inclusion are similar (Fig. 8b and c).

In Miles-10 (Fig. 1c), bulk abundances for most incompatible elements are uniformly enriched. For instance, REE abundances are fairly uniform at $\sim$4–5$\times$ CI-chondrites, with a slight LREE-enrichment and no Eu anomaly (Fig. 8b). Many other elements have similar abundances ($\sim$3–6$\times$ CI-chondrites), including Ca, Sc, Ti,

V, Cr, Sr, Y, Ba, U, and (to within the extent of uncertainty) Rb and Th.

More fractionated compositions are shown by smaller inclusions, such as Miles-2A, Miles-5, and Miles-9 (Fig. 8c). Especially noteworthy is the composition of the latter, a rhyolitic inclusion that is rich in plag, K-feldspar, and silica (Fig. 3h and Table 2b). Although rich in Si, Rb, Cs, and Ba, the rhyolitic inclusion is poor in most incompatible elements (Fig. 8c; Table EA-2b), corresponding to the low abundances of these elements in the feldspars and silica phase in the inclusion.

The bulk-chemical data for Miles imply increasingly fractionated compositions for progressively smaller inclu-
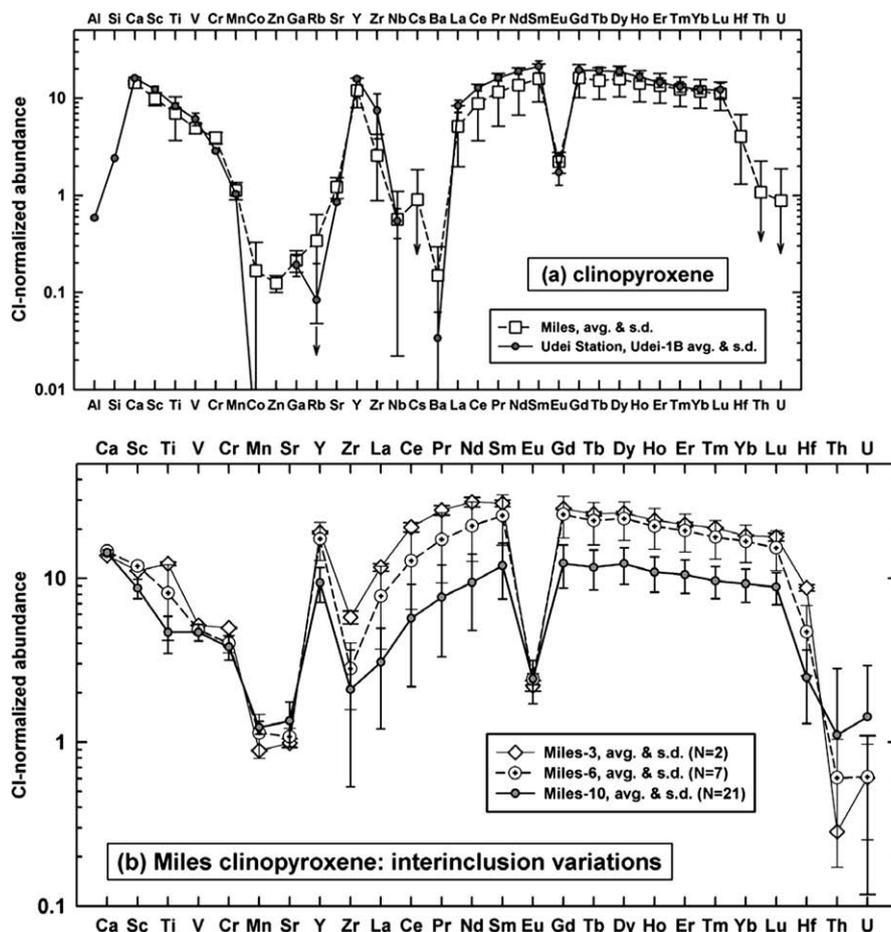
Fig. 5. CI-normalized abundances for clinopyroxene measured by LA-ICP-MS. (a) Average clinopyroxene in Miles and Udei Station. (b) Average clinopyroxene compositions in Miles-3, -6, and -10 for selected elements illustrating interinclusion variability. N = number of analyses averaged. (c) Data for Miles-10 clinopyroxene illustrating intrainclusion variability. Data for grain rims refer to an average of seven analyses obtained within $\sim$100 μm of plagioclase. (d) Clinopyroxene grain compositions at different locations for a single zoned grain in Miles-6. This grain is the same one analyzed with an EMPA traverse in Fig. EA-2b and located in Fig. 3g. In parts (a)–(c), error bars show standard deviations of means. In parts (c) and (d), x = approximate distance of analysis at central point from grain rim.

sions. Miles-10 has the largest area and also has the least fractionation between incompatible elements. The Miles 1–9 composite is $\sim$6× smaller and only slightly more fractionated. Miles-2A, Miles-9, and Miles-5 each have only $\sim$0.15–0.25% the area of Miles-10 and are the most chemically fractionated inclusions analyzed in Miles. This trend is probably caused in large part by unrepresentative sampling, which can occur when the sizes of inclusions become similar to the sizes of the grains within them. We suggest the composition of the largest inclusion (Miles-10) is the most representative of the overall bulk silicate in Miles.

4. DISCUSSION

4.1. Partial melting, melt migration, and crystallization

Textures, mineralogy, and two-pyroxene geothermometry (Section 3) suggest that igneous processes including partial melting were important in the formation of silicates inclusions in Udei Station and Miles. In Udei Station, the inclusions appear to consist both of lithologies that repre-

sent solids remaining after the removal of a partial melt, as well as lithologies that crystallized from either a portion or all of the extracted partial melt. In contrast, all inclusions in Miles probably crystallized from a partial melt.

4.1.1. Udei Station

Most inclusions in Udei were probably at least partly melted. In the poikilitic areas of Udei (Fig. 2b, d, and e), textures imply that plag crystallized after opx, and that opx may have nucleated on olivine. There is good evidence in Udei for local silicate melt migration. Granular zones in Udei which have a harzburgitic mineralogy (Fig. 2c–f) probably represent melt residues that were produced by the extraction of a partial melt. Batch melting models suggest that the overall composition of the harzburgitic areas in Udei-3B can be explained if they are the residues after removal of a 3–10% partial melt of a chondritic protolith (Fig. 9a). Based on comparisons with experiments on peridotite melting summarized by Taylor et al. (1993), this degree of partial melting corresponds to a maximum temperature of <1180 °C for Udei.
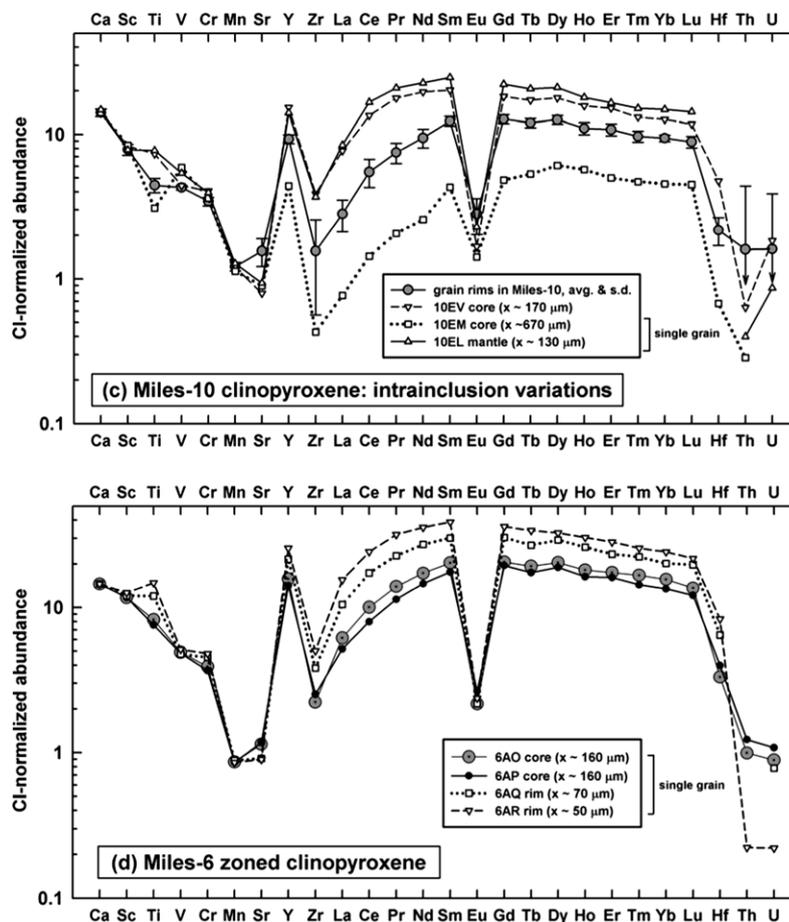
Fig. 5 (*continued*)

The data for Udei-3B strongly suggest that silicate melt was effectively separated from silicate residue at a low degree of melting. This occurred despite the inability of silicate to fully separate from metal. Density contrast was evidently not the sole, controlling variable for solid–melt separation in Udei, as this would have resulted in more effective separation of silicate from metal than of silicate melt from silicate solid. Instead, surface tension effects between liquids and solids were probably a more controlling variable (Takeda et al., 2000, 2003), with metallic melt less able to migrate than silicate melt, in agreement with one would expect from experimental data (e.g., Rushmer et al., 2000; McCoy et al., 2006).

Melt migration also may have been aided by the flow of a pressurized gas (Keil and Wilson, 1993; Ruzicka et al., 2006; McCoy et al., 2006). The presence of such a gas in Udei is implied by the variable amounts of graphite in Udei-3B (Fig. 2e–h). In IAB irons, graphite may have co-existed with a CO gas (Kracher, 1985). We suggest that such a gas helped push interstitial silicate melts through the largely solid Udei-3B granular zone and into an adjacent melt-rich zone which subsequently crystallized as the poikilitic border zone (Fig. 2d and e). The gas would have readily escaped in a melt-rich zone, but in the mostly solid areas of Udei-3B, it was trapped long enough to form locally abundant graphite.

Grain growth accompanied the extraction of silicate melt in Udei-3B, as evidenced by the coarser grain sizes in progressively feldspar-poor areas. Typical grain sizes of ol and opx range from ~100 μm in Udei-1A-1 which has a near-chondritic proportion of feldspar (Fig. 2a), to ~100–500 μm in Udei-3B granular #1 (harzburgite with ~2% feldspar) (Fig. 2e), to ~100–1500 μm in Udei-3B granular #2 (harzburgite with only trace feldspar) (Fig. 2f).

Udei-1B, which has a basaltic mineralogy (Fig. 2j), has the approximate chemical composition expected for a melt produced by ~10–20% partial melting (Fig. 9b). This is greater than the 3–10% partial melting needed to produce the harzburgitic areas, however, so the basalt did not form simply by equilibrium crystallization of "batch" melt that was separated from harzburgitic areas. Moreover, the bowed REE pattern of Udei-1B is in detail different than the slightly LREE-enriched pattern that would be expected for a partial melt (Fig. 9b). Finally, the irregular outlines of the inclusion and the variation in grain size from one side to the other (Fig. 2j) is suggestive of a cumulate process. Additionally, as will be shown in Section 4.4, it is clear that the plag and cpx crystals did not form in equilibrium with one another, requiring a more complex petrogenesis for the basalt.

Poikilitic areas in Udei are not simple melt residues or melts, as their compositions are unlike what one would ex-
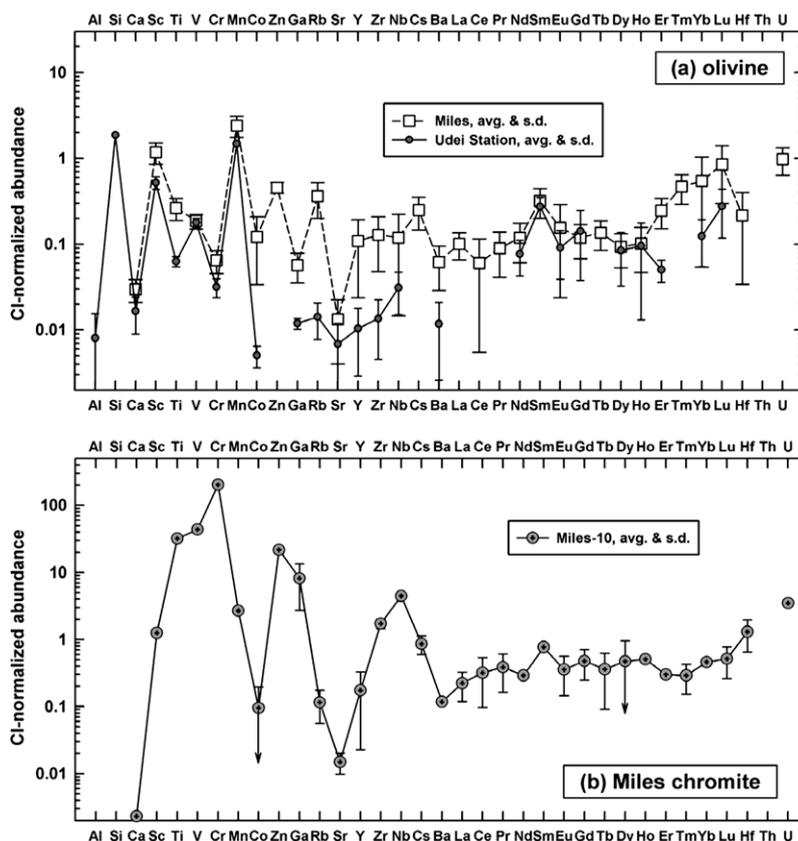
Fig. 6. CI-normalized abundances measured by LA-ICP-MS for (a) average olivine in Miles and Udei Station and (b) chromite in Miles-10. Error bars show standard deviations.

pect of either these (Fig. 9a and b). Instead, they have relatively high abundances of Al, Sr, Ba, and Eu and an overall low concentration of incompatibles (Fig. 9b). These characteristics suggest an excess of plag and the removal of a low-temperature melt component. We suggest that the poikilitic areas in Udei formed as a cumulate or partial cumulate, involving the crystallization of feldspar from melt that surrounded opx crystals. The opx itself could be an early-crystallizing cumulus mineral. The poikilitic areas are poor in cpx, which evidently was removed from these areas either in the form of a low-temperature melt component or as cpx crystals that had migrated elsewhere.

The lithologic contact in Udei-3B between the granular and poikilitic areas, although sharp, is clearly not a breccia contact as it follows the detailed outlines of euhedral–subhedral opx grains (Fig. 2e). Moreover, the similar grain sizes and composition of opx on both sides of the contact imply that it is a primary igneous demarcation. This contact probably separated restite from an adjacent molten area, now represented by the granular and poikilitic areas, respectively.

4.1.2. Miles

In contrast to Udei, silicate inclusions in Miles represent material crystallized from a partial melt (Ikeda and Prinz, 1996; Ikeda et al., 1997). Textures leave no doubt that plag largely crystallized after opx, cpx, ol, and chromite (Fig. 3a and c). That opx crystallized largely before plag in Miles is

also consistent with observed silicate–metal contacts: metal fills interstices between opx grains and so probably crystallized after some opx, but plag–metal contacts are smooth (Fig. 3a), as if metal solidified around an immiscible feldspathic silicate liquid that had not yet crystallized plag.

The composition of the large inclusion Miles-10, which is probably most representative of the overall silicate in Miles, is similar to that expected for a batch melt of a chondritic precursor produced by ~30% partial melting (with a best estimate based on the REE of 28% melting) (Fig. 9c). This corresponds to a maximum temperature of ~1250 °C (Taylor et al., 1993). The parent melt must have extensively separated from silicate residue as there is no evidence for a residue lithology in Miles. As with Udei, however, silicate melt and solids in Miles were able to separate without the complete separation of silicate from metal.

The estimate of ~30% partial melting to form Miles inclusions is relatively robust. It is insensitive to the precise residue mineralogy that is assumed, so long as the residue is rich in ol and opx. Moreover, the melting model for Miles-10 provides a good match for many elements. Some elements are discrepant but this is probably not significant, as it mostly includes elements that could be significantly partitioned into phases not included in the models. The melting model fails to account adequately for the abundance of Cs, but D-values are poorly known for this element. More significantly, Cr content in Miles-10 is much higher than predicted by the melting model (Fig. 9c). This
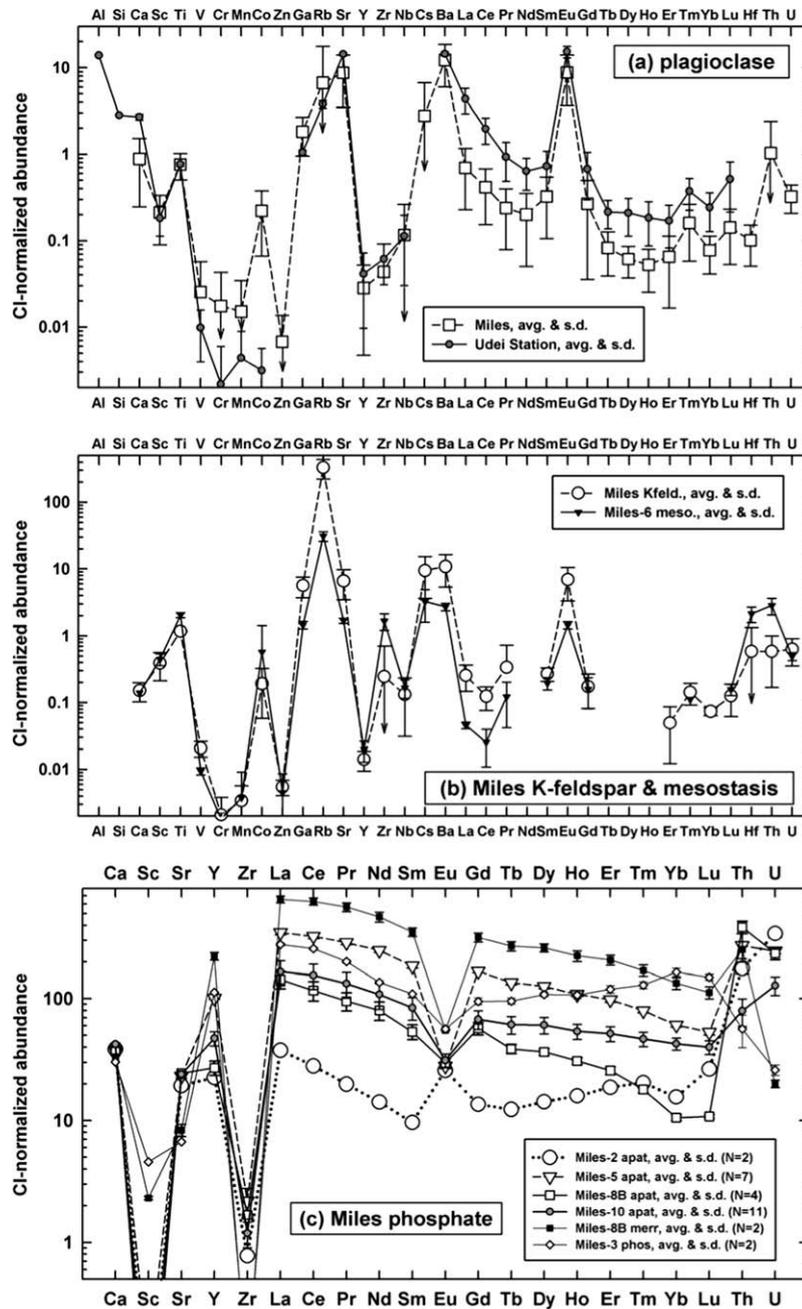
Fig. 7. CI-normalized abundances measured by LA-ICP-MS for (a) average plagioclase in Miles and Udei Station, (b) average K-feldspar and mesostasis in Miles, and (c) average phosphate (all single grains) in different inclusions from Miles (N = number of grains averaged). Error bars in all cases represent standard deviations.

could indicate that much of the chromite in Miles-10 formed by a cumulate process.

In any case, our best estimate of ∼28% partial melting to form Miles inclusions agrees remarkably well with the ∼25% partial melting proposed by Ikeda and Prinz (1996) based on an estimate of the average major-element composition of inclusions. In contrast, our results disagree with the 10% partial melting estimated by Hsu (2003). As discussed in Section 3.3.2, the bulk-chemical data of Miles inclusions are increasingly fractionated for smaller inclusion sizes. Thus the results of Hsu (2003), which were based

on small inclusions, could be easily biased by inadequate sampling.

To account for the variations in bulk composition seen in smaller Miles inclusions, as well as the similar trace-element composition of opx in different inclusions and more divergent compositions of other minerals, we suggest that silicate melt pockets and grains became isolated from one another as silicate and metal crystallized. Pyroxene grains became isolated to form orthopyroxene-rich inclusions such as Miles-2A, and melt pockets became isolated to form rhyolitic inclusions such as Miles-9.
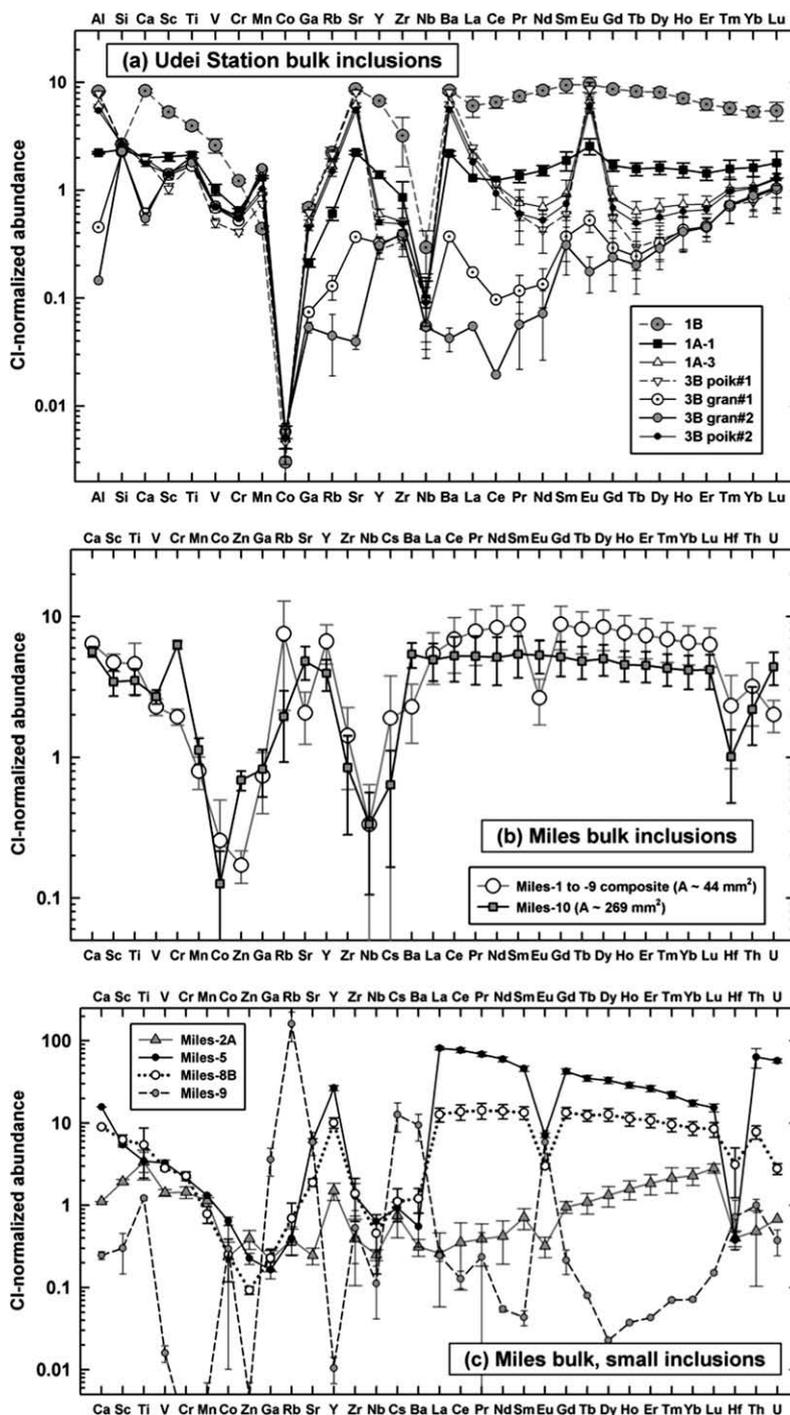
Fig. 8. Reconstructed CI-normalized bulk abundances for (a) Udei Station inclusions (poik, poikilitic; gran, granular); (b) large inclusion Miles-10 and a composite (area-weighted) composition for Miles-1 through -9 (A = mapped area); and (c) selected small Miles inclusions. In all cases, error bars reflect 1σ uncertainties based on uncertainties in phase compositions.

4.2. Metal–silicate separation

The presence of metal-rich veins in silicate inclusions from Udei but not Miles (Fig. 1; see also Fig. 2c and f) and the occasionally high contents of metal inside inclusions from Udei (Tables 2a and b) is suggestive of a more advanced stage of metal–silicate separation in Miles. In Udei, a substantial amount of solid silicate was present at

the highest temperatures that were reached, and this allowed more metal to become trapped within inclusions. Some of this metal probably coalesced to form liquid veins that moved through the partly solid silicate assemblage. Evidence for late transport of metal through solid silicate is provided by the presence of coarse metal-rich veins in Udei-3B that cross-cut the different lithologic zones (Fig. 2c). Minor transport of metallic melt through silicate

also appears to have occurred in narrow veins that now connect separate metal grains (Fig. 2f).

We suggest that the fundamental reason that silicate and metal did not fully separate in either meteorite is that maximum temperatures were not sufficiently high for a sufficiently long period of time prior to solidification. If the proportion of solid metal substantially exceeds that of liquid metal at a given temperature, silicate inclusions consisting of immiscible melt and crystals will be unable to freely pass through the metallic host and will be constrained to flow in passageways between metal grains. As temperature decreases these melt passageways will freeze, preventing further migration of silicate material. Evidence that this occurred for Miles is provided by the presence of inclusions along metal grain boundaries.

Fe–S equilibria provide the main control on metallic solid and melt proportions in a chondrite (Hansen and Anderko, 1958; Doan and Goldstein, 1970; Usselman, 1975). Using the Fe–S phase diagram (Hansen and Anderko, 1958) and assuming an H-chondrite precursor, we infer that at peak temperatures in Udei the amount of solid metal ($\sim$63% at 1150 °C) exceeded that of liquid metal, but that the opposite would be true for Miles ($\sim$42% at 1250 °C). However, Miles has a significantly lower S content than an H-chondrite (Ikeda and Prinz, 1996), so the proportion of metal that was solid at $\sim$1250 °C should have exceeded 50%. Once the silicates in Miles and Udei had crystallized and most metal was also solid, complete silicate–metal separation would be inhibited.

Potentially some separation of metallic melt from solid metal could have occurred in both meteorites. Although gravity would tend to make solid metal sink relative to liquid metal, the latter would be more mobile, and most researchers have suggested that metallic melt would tend to sink relative to a suspended mixture of solid metal and silicate (e.g., Kelly and Larimer, 1977; Kracher, 1985; Wasson and Kallemeyn, 2002). Although the composition of metal in Miles has been interpreted as that of a metallic melt separated from solid metal (Ebihara et al., 1997), the overall composition of metal in IIEs and IABs is not readily interpreted as that of either a melt or solid metal component. For example, average concentrations of Ir, Au, As, and Co in metal from H-chondrites (Kong and Ebihara, 1997) are similar to those in normal IIE (Wasson and Wang, 1986) and main group (relatively Ni-poor) IAB irons (Wasson and Kallemeyn, 2002), despite these elements having different metal solid/liquid partition coefficients (e.g., Ir is compatible, Au and As are incompatible, and Co is relatively indifferent; Wasson and Kallemeyn, 2002). Thus, if metallic melt–solid separation occurred, it did not occur in such a way as to significantly perturb the average composition of metal in IIEs and Ni-poor IABs from presumed chondritic initial compositions.

4.3. Redox equilibria and reaction to form phosphate

Both Udei and Miles show textural evidence for the formation of phosphate by reaction between silicate and metal phases, although the reaction was only incipient in Udei. These reactions appear to have been important in control-

ling phase compositions during a late stage of crystallization. The inferred reactions are similar to those described previously for various types of meteorites (Murrell and Burnett, 1983; Harlow et al., 1982; Ikeda et al., 1997; Ruzicka et al., 1999, 2005):

$$\underset{\text{diopside}}{3CaMgSi_2O_6} + \underset{\text{metal}}{2P} + \underset{\text{metal}}{3Fe} + \underset{\text{gas}}{4O_2}$$
$$\rightarrow \underset{\text{enstatite}}{3MgSiO_3} + \underset{\text{ferrosilite}}{3FeSiO_3} + \underset{\text{merrillite}}{Ca_3(PO_4)_2} \qquad (1)$$

and

$$\underset{\text{clinopyroxene}}{3Ca(Mg,Fe)Si_2O_6} + \underset{\text{metal}}{2P} + \underset{\text{gas}}{5/2O_2}$$
$$\rightarrow \underset{\text{orthopyroxene}}{3(Mg,Fe)SiO_3} + \underset{\text{merrillite}}{Ca_3(PO_4)_2} + \underset{\text{silica}}{3SiO_2} \qquad (2)$$

Evidence for these reactions in Udei is provided by the thin selvages of opx that separate cpx from metal (Fig. 2b). Evidence in Miles includes the almost invariable presence of opx between cpx and metal (Fig. 3d, e, and j), and the typical occurrence of phosphate (Fig. 3c and d) and a silica phase (Fig. 3b and e) adjacent to metal. The wider opx zones and more abundant phosphate in Miles imply that the reactions proceeded to greater extent in Miles than in Udei. The presence of Ca-poor opx adjacent to metal in Miles (e.g., Fig EA-2a) is also consistent with these reactions as it implies depletion of a cpx component adjacent to metal. Finally, the common presence of schreibersite in Miles suggests that reduced P was abundant in this meteorite.

Although phosphate could have formed either above or below the solidus, we suggest that most phosphate in Miles crystallized from a residual melt, as advocated by Ikeda et al. (1997). Orthopyroxene overgrowths on cpx (Fig. 3e) thus could be explained by crystallization of opx from melts that were becoming increasingly depleted in a cpx component as a result of phosphate crystallization.

Group B opx in Miles, which is found adjacent to metal and as overgrowths on cpx, probably crystallized during phosphate-forming redox reactions. The low HREE content in Group B opx compared to Group A opx (Fig. 4b) can be explained as a result of HREE uptake by phosphate in the melt out of which Group B opx crystallized. The LREE have about the same concentration in Group A and Group B opx, however (Fig. 4b). Perhaps a kinetic barrier prevented the diffusion of LREE from cpx to phosphate Although diffusion rates of the LREE and HREE are similar in enstatite (Cherniak and Liang, 2007) and would be expected to be similar in melt, the LREE diffuse much more slowly than the HREE in diopside (Van Orman et al., 2001). If Group B opx grew in place of cpx or grew from melt adjacent to cpx that was undergoing diffusive exchange with cpx, this might explain the unexpectedly high LREE abundances in the opx.

Group C opx, which also has low contents of the HREE and Ca (Fig. 4c) and which forms fine-grained mixtures with metal (Fig. 3i), may have formed by an unrelated process. The intimate mixture of opx and metal is unusual for Miles and suggests that the two phases were not able to unmix owing to quenching. We suggest Group C opx crystallized rap-

idly at the highest temperatures, and that this resulted in irregular and presumably disequilibrium REE patterns.

4.4. Mineral equilibration and exchange modeling

4.4.1. Mineral equilibration

The compositions of minerals in Udei and Miles can be used to evaluate whether they were in equilibrium. Figs. 10

and 11 compare equilibrium partition coefficient (*D*-value) ratios to measured concentration ratios for various mineral pairs. Agreement between the two sets of ratios is indicated by a 1:1 (45°) correlation line and is taken to be evidence for equilibrium, whereas departure from the 1:1 line is taken to be evidence for disequilibrium. The *D*-values that were assumed refer to mineral/melt partition coefficients, so the models strictly test whether equilibrium was maintained be-

tween mineral pairs and a co-existing melt. Available evidence suggests that under subsolidus conditions, *D*-values will increase for all REE (especially the LREE) and for most transition elements in cpx relative to opx and olivine (Seitz et al., 1999; Green et al., 2000; Witt-Eickschen and O'Neill, 2005), and that LREE will preferentially partition into plag and out of opx, and HREE out of plag and into opx, during exchange between the two minerals (Floss et al., 1998).
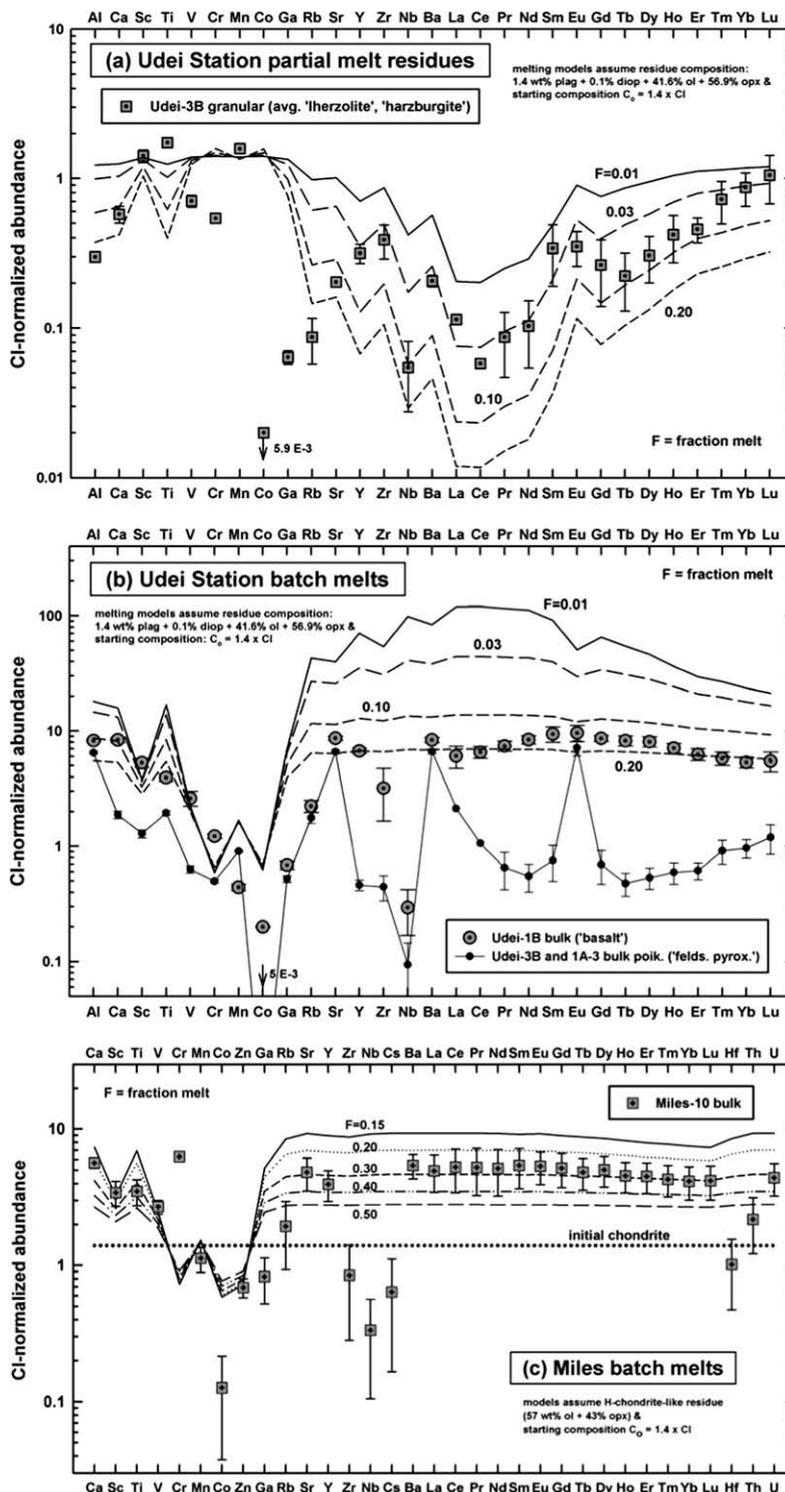
Plagioclase is the only mineral that was analyzed in all of the Udei inclusions, so this mineral is chosen as the reference mineral to which opx and cpx are compared in Fig. 10. Orthopyroxene and plag in Udei appear to be largely in equilibrium with one another, with only a few elements present in significant excess in either opx or plag (Fig. 10a). This implies an approach to equilibrium under magmatic conditions for opx and plag in Udei. In contrast, cpx (analyzed only in Udei-1B) and plag are largely in disequilibrium with one another in Udei (Fig. 10b). Most trace elements are present in excess in cpx compared to plag. This mainly includes highly incompatible elements such as the REE, Nb, and Y. Evidently cpx does not reflect the same equilibrium conditions as plag in Udei. The discrepancy for cpx could be explained by the re-equilibration of cpx under subsolidus conditions, but this is unlikely as REE diffusion rates in cpx are relatively slow compared to that in plag (Van Orman et al., 2001; Cherniak, 2003; Cherniak and Liang, 2007), not fast as would be required. More likely, cpx in Udei-1B crystallized from a more evolved melt composition than plag.

For Miles, the reference mineral that is chosen is cpx, as it is both widely distributed throughout inclusions in this meteorite and has well-determined concentrations of many trace elements. Fig. 11a shows that cpx and opx in Miles have compositions consistent with magmatic equilibrium for virtually every element analyzed. In contrast, Fig. 11b and c show that virtually every element is out of equilibrium between cpx and plag, and between cpx and apatite. Most elements, including most incompatible elements, are present in similar excess in cpx compared to both plag and apatite (Fig. 11b and c). Considering that plag and phosphate mostly crystallized after opx and cpx in Miles (Sections 4.1.2 and 4.3), the data thus imply that there were two sets of equilibrium conditions in Miles: an early stage ("Stage 1") represented by opx and cpx in a magmatic system that was enriched in incompatible elements, and a later stage ("Stage 2") under different conditions represented by plag and phosphate.
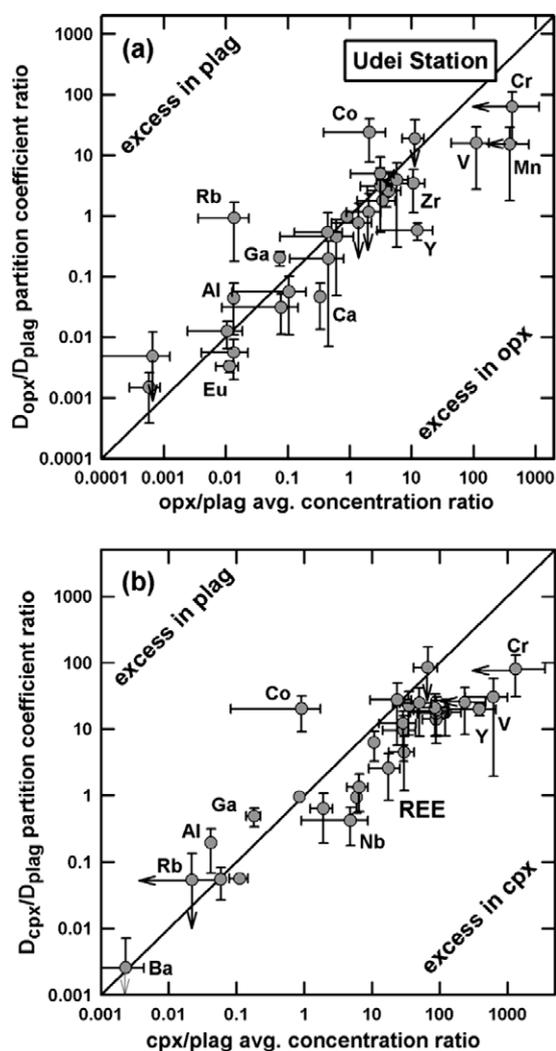
Fig. 10. Comparison between mineral/melt partition coefficient (*D*-value) ratios and measured mineral concentration ratios for mineral pairs in Udei Station. Error bars represent 1σ uncertainties based on standard deviations of average values for phase compositions and partition coefficients. (a) Orthopyroxene (opx)–plagioclase (plag) and (b) clinopyroxene (cpx)–plagioclase (plag).

4.4.2. Exchange models

To help evaluate the conditions under which minerals equilibrated, we constructed "exchange models" that assume local buffering between minerals in a system of specified bulk composition. In these models, mineral–min-

Fig. 9. CI-normalized diagrams that illustrate the results of models which assume equilibrium partial melting (lines) are compared to various lithologies. A representative chondrite protolith with initial elemental abundances of 1.4× CI-chondrites is assumed. (a) Partial melt residues produced at different degrees of melt fraction (F) compared to the composition of Udei-3B granular areas (harzburgite, with bars indicating standard deviation of the average). The assumed residue mineralogy corresponds to that observed for the Udei-3B granular areas. (b) Partial melts produced at different degrees of melt fraction (F) compared to the composition of Udei-1B and the average of Udei-1A-3 and Udei-3B poikilitic areas. The assumed residue mineralogy corresponds to that observed for the Udei-3B granular areas. Error bars for Udei-1B correspond to the 1σ uncertainties based on uncertainties in phase compositions, and for Udei-1A-3 and -3B to the standard deviation of the mean composition for poikilitic areas. (c) Partial melts produced at different degrees of melt fraction (F) compared to the composition of Miles-10, assuming an H-chondrite-like olivine:orthopyroxene residue mineralogy. Error bars for Miles-10 reflect 1σ uncertainties based on uncertainties in phase compositions.
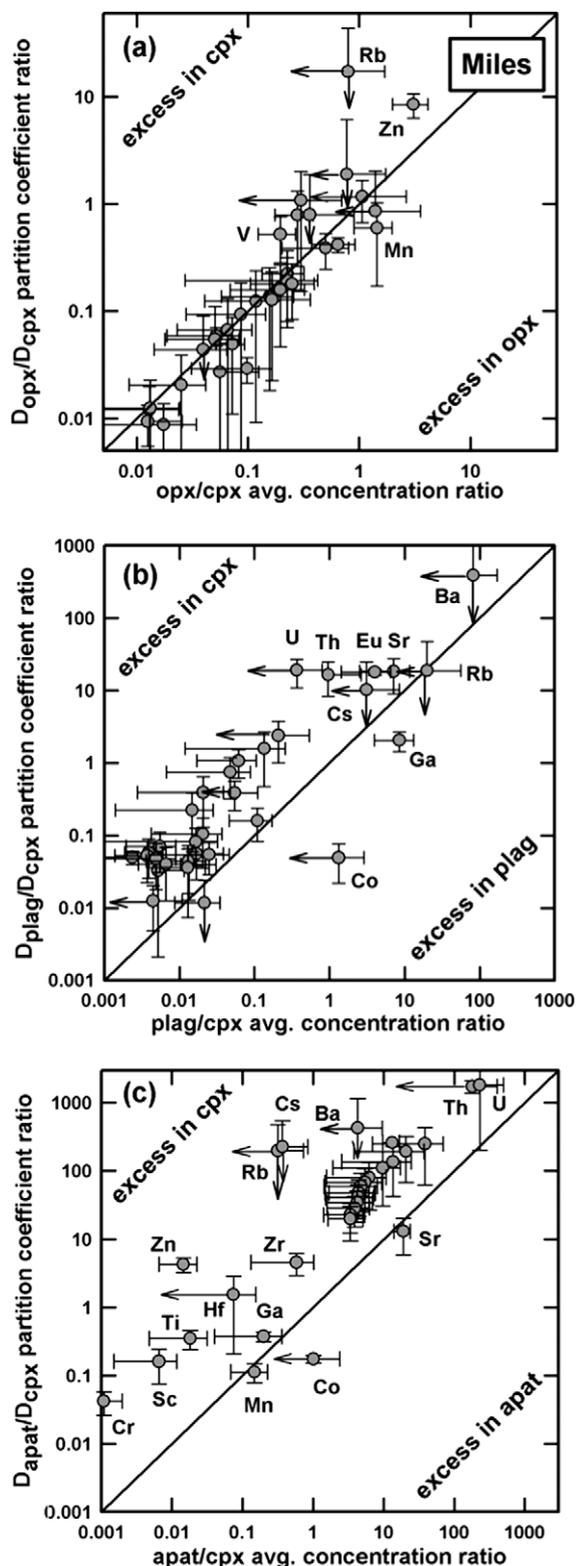
Fig. 11. Comparison between mineral/melt partition coefficient (D-value) ratios and measured mineral concentration ratios for mineral pairs in Miles. Error bars represent 1σ uncertainties based on standard deviations of average values for phase compositions and partition coefficients. (a) Orthopyroxene (opx)–clinopyroxene (cpx), (b) plagioclase (plag)–clinopyroxene (cpx), and (c) apatite (apat)–clinopyroxene (cpx).

eral equilibrium partitioning occurs according to D-value ratios. Similar models for eucrites and ordinary chondrites have tested the possibility of an equilibrium "metamorphic" exchange between minerals under subsolidus conditions assuming that metamorphic and magmatic D-value ratios are the same (Curtis and Schmitt, 1979; Treiman, 1996; Ruzicka et al., 2005). As shown in Section 5 of Electronic Annex, this type of modeling can be extended to include the presence of a melt, to test the possibility of equilibrium between crystals and melt following the crystallization of multiple minerals. Provided that the bulk composition and proportions of minerals are specified, the amount and composition of melt can be readily determined. In the discussion that follows, we focus on the REE as the partition coefficients for these elements are relatively well known.

4.5. Petrogenesis of silicates in Udei Station

Udei Station has four lithologies, representing different bulk-chemical systems. These include (a) subchondritic (1A-1), (b) basaltic (1B), (c) granular restite (3B granular #1 and #2), and (d) poikilitic (1A-3, 3B poikilitic #1 and #2) lithologies (Section 3.1.2). For Udei Station we investigated whether measured compositions for opx, plag, cpx, and ol are consistent with equilibration in these different systems, either under subsolidus conditions or in the presence of melt that co-existed with the minerals in different regions.

Measured compositions for opx and plag resemble model equilibrium compositions in bulk-chemical systems similar to the poikilitic areas for both minerals and in the granular restite areas for opx (Fig. 12a and b). They are most inconsistent for models involving either an overall chondritic or basaltic composition (Fig. 12a and b), both of which contain more cpx.

The composition of cpx in Udei resembles the model equilibrium composition for a chemical system similar to the Udei-1B basalt inclusion in which it is found, although the model underestimates the measured LREE abundances in cpx (Fig. 12c). Other modeled chemical systems clearly are inconsistent with the observed composition of cpx (Fig. 12c).

Altogether, these results imply that opx and plag could have equilibrated in a system in which cpx was not an important buffering phase, and that cpx equilibrated in a different system. The REE content of cpx in Udei-1B is similar to that expected for equilibrium with a very low-degree (~1%) partial melt (Figs. 12c and 9b). We infer that cpx crystallized from the last residual melt that remained after the equilibration of plag and opx.

All models suggest that olivine should have a LREE-depleted pattern, unlike the relatively flat REE pattern that is observed (Fig. 12d). The measured concentrations for most other elements also cannot be reproduced by the models (Fig. 12d). Most olivine in Udei would not have significantly melted for the low degree of partial melting (~3–10%) inferred for the meteorite (Section 4.1.1). We therefore suggest that although olivine grain rims may have equilibrated with surrounding melt, sluggish diffu-

Comparative petrology of silicate-bearing irons
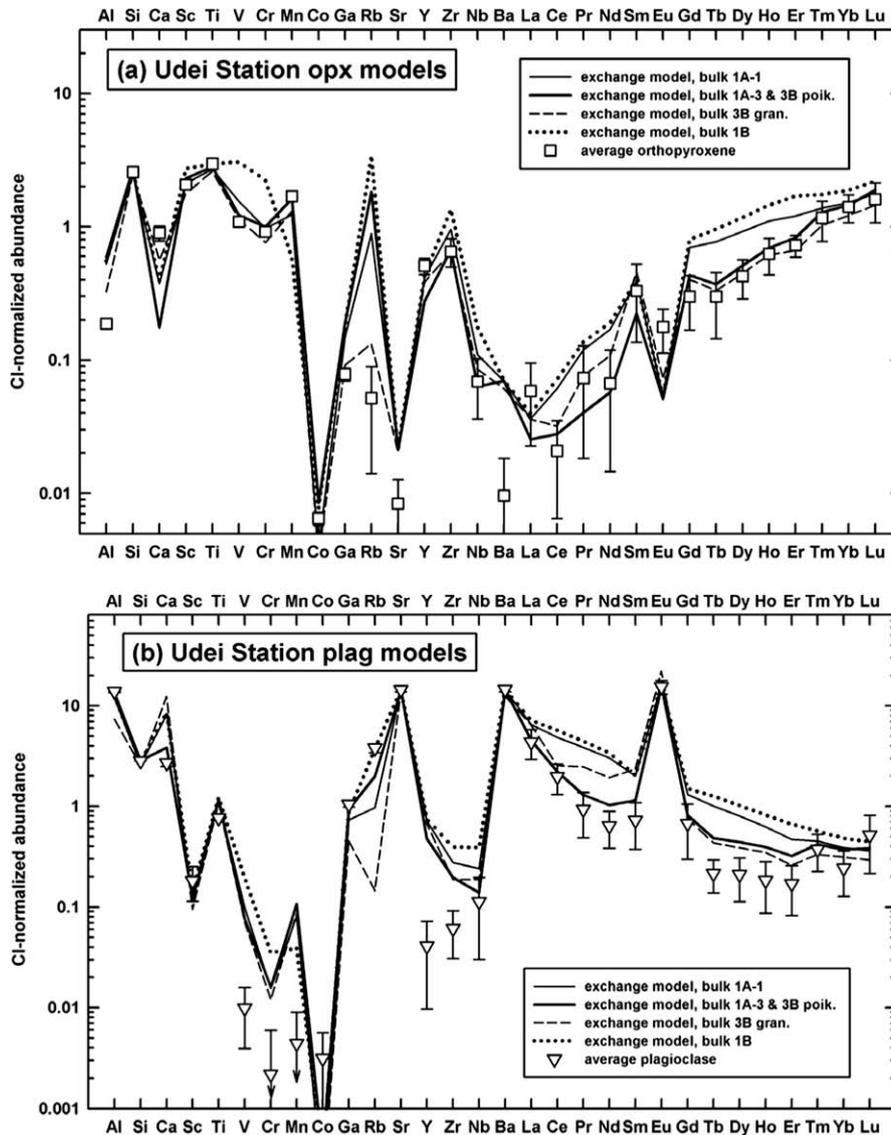
Fig. 12. CI-normalized abundance diagrams comparing average mineral compositions for Udei Station to predicted equilibrium compositions based on exchange models (see text). Various bulk-chemical systems are assumed for the exchange models, corresponding to chondritic (Udei-1A-1), average poikilitic lithology (Udei-1A-3 and Udei-3B), average restite lithology (Udei-3B granular), and basaltic (Udei-1B). Error bars in all cases refer to the standard deviations of mean phase compositions. (a) Orthopyroxene, (b) plagioclase, (c) clinopyroxene, and (d) olivine.

sion kinetics could have prevented the interiors of olivine grains from equilibrating with their surroundings. This is equally true for olivine in areas that experienced significant melt–solid separation (Udei-3B) as for areas that did not undergo significant melt–solid separation (Udei-1A-1) (Fig. 12d).

4.6. Petrogenesis of silicates in Miles

The complex crystallization history experienced by inclusions in Miles (Section 4.4.1) can be successfully modeled using two approaches. Stage 1 crystallization can be modeled by equilibration between cumulus minerals (Group A opx, cpx, olivine, and chromite) and intercumulus melt, whereas Stage 2 can be modeled by fractional crys-

tallization of plag and phosphate from an evolved melt composition.

For Stage 1, we use exchange models that equate the bulk composition of the system to the composition of the large inclusion Miles-10, with cpx, opx, plag, ol, chromite, apatite and intercumulus melt as possible phases. Our model assumes that all plag crystallized after cpx, opx, ol, and chromite, and that all apatite crystallized last. In reality, some opx and cpx probably crystallized together with plag and apatite (Ikeda and Prinz, 1996) and multiple phases may have crystallized at the solidus, but the model provides a useful approximation to the likely crystallization sequence, with results that are easily interpretable.

The composition of intercumulus melt for different melt proportions is shown in Fig. 13a. Particularly noteworthy
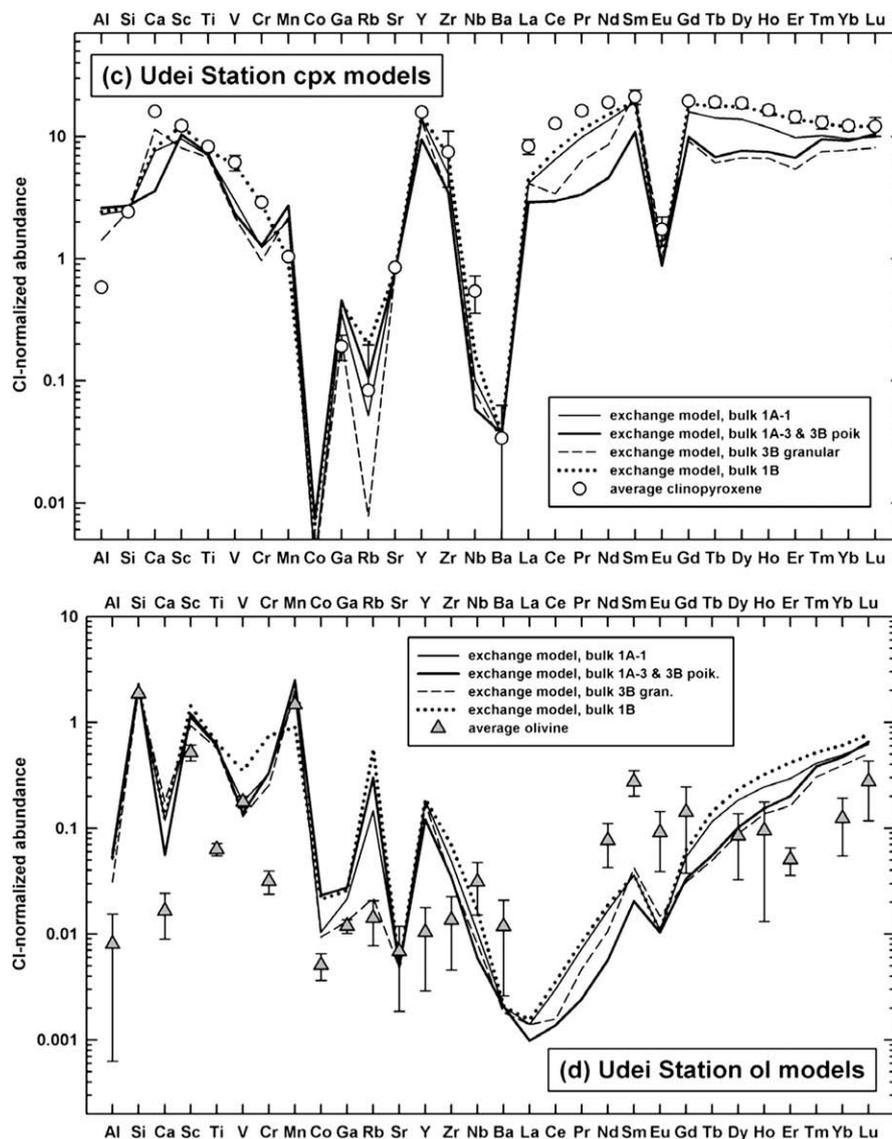
Fig. 12 (*continued*)

in Fig. 13a is the large increase in melt REE contents during crystallization until the moment when apatite crystallizes (from 32% to 2% melt in the model), at which point the REE content in the melt decreases dramatically.

Fig. 13b shows that the composition of the model 2% intercumulus melt closely resembles that of a melt in equilibrium with average cpx, opx, and chromite ("equilibrium melt") in Miles for most elements. Even the composition of

Fig. 13. CI-normalized abundance diagrams illustrating exchange model results for Miles, assuming a bulk-chemical system with the same composition as Miles-10 (see text). (a) Composition of model intercumulus melts for different melt fractions. The 32% melt case refers to one in which all phases except plag and apatite have crystallized, whereas the 17% melt case refers to one in which half the plag has crystallized, 2% melt refers to a case to one in which all phases except apatite have crystallized, 1% melt refers to a case in which half the apatite has crystallized, and the 0% melt case refers to the last liquid present. (b) Comparison between the composition of 2% intercumulus melt and the inferred equilibrium melt compositions corresponding to the average composition of orthopyroxene, clinopyroxene, chromite, and olivine in Miles. (c) Comparison between the predicted equilibrium composition of clinopyroxene for three models and the measured range of clinopyroxene in Miles. The average composition of clinopyroxene rims (analyzed within ~100 μm of plagioclase) in Miles-10 is also shown. (d) Comparison between the predicted equilibrium composition of orthopyroxene for three models and the measured range of Group A orthopyroxene in Miles. (e) Comparison between the predicted equilibrium composition of plagioclase for three models and the measured range of plagioclase in Miles. (f) Comparison between the predicted equilibrium composition of apatite for two models and the measured range of Cl-apatite in Miles.

the average equilibrium melt for ol agrees with the 2% inter-cumulus melt composition for many transition elements and the HREE, although the LREE are clearly far more abundant in ol than can be explained by the exchange model (Fig. 13b). This implies that cpx, opx, chromite, and ol could have partly equilibrated with an intercumulus melt after approximately 98% crystallization. This melt could not have been affected by significant crystallization of apa-tite as this would have resulted in REE contents much low-er than measured for the other minerals.

Fig. 13c and d compare model predictions for the com-position of cpx and opx and the measured ranges for these minerals in Miles. The model composition for cpx and opx in a system with 2% intercumulus melt agrees well with the data for many elements, especially the REE. A particularly close match is observed between the observed composition

(a) Miles model intercumulus melts

32% melt case
17% melt case
2% melt case
1% melt case
~0% melt case

(b) Miles intercumulus & equilibrium melts

exchange model, 2% melt
equil. melt for orthopyroxene
equil. melt for clinopyroxene
equil. melt for chromite
equil. melt for olivine

(c) Miles cpx models

measured range
exchange model, 32% melt
exchange model, 2% melt
exchange model, 0% melt
avg. cpx rim

Fig. 13 (*continued*)

of cpx rims in Miles-10 and model cpx in a system with 2% melt (Fig. 13c). This suggests that the composition of the rims was established by equilibration between the rims and melt, just prior to phosphate crystallization. Higher REE concentrations in cpx from some smaller inclusions presumably reflect bulk-chemical systems more enriched

in the REE than Miles-10, whereas the lowest measured REE abundances in cpx resemble those for a system with a high melt proportion (32%) (Fig. 13c and d). To account for the observation that some cpx grains in Miles-10 are complexly zoned, with low-REE cores, enriched-REE mantles, and rims with intermediate REE abundances (Fig. 5c),

we suggest that cpx crystallized over a significant solidification interval, and that intracrystalline REE exchange in cpx was limited. This has important implications for the thermal history of Miles (see Section 4.7).

Measured abundances of Sr inversely correlate with those of the REE in cpx (Fig. 5b and d). This can be explained by the co-crystallization of plag, which would decrease Sr abundances in the remaining melt and decrease the amount of Sr that could partition into cpx (Fig. 13a and c). Co-crystallization of plag and cpx can result in a decrease in Al content of cpx (Ikeda and Prinz, 1996), which can explain the data for the zoned cpx grain in Miles-6 (Fig. EA-2b). This inference requires that the assumed crystallization model assumed for Miles (all plag crystallizes after all cpx) is indeed oversimplified, as some plag and cpx appear to have co-crystallized.

Although the measured REE abundances in Group A opx closely resemble those predicted for equilibration with a relatively evolved melt prior to apatite crystallization, the lower HREE abundances of Group B opx more closely resemble the predicted composition of opx for a system with ∼0% melt after apatite crystallization, or alternatively a much less solidified system with ∼32% melt (cf. Figs. 13d and 4b). As Group B opx probably crystallized after Group A opx (Section 4.3), the lower HREE abundances of Group B opx most likely records equilibration under essentially solidified (and possibly subsolidus) conditions.

Fig. 13e and f compare measured ranges in the composition of plag and apatite with the predictions of exchange models. In contrast to pyroxene, the models clearly fail to explain the measured compositions of these minerals, with model REE abundances for both minerals too high by about an order of magnitude compared to the measured abundances. Moreover, the LREE-enriched pattern of apatite in Miles is unlike the relatively flat LREE pattern predicted for a system with either trace or no melt (0% melt case, Fig. 13f). Thus plag and apatite in Miles did not equilibrate in systems that were either solidified or that contained enriched intercumulus melt.

Rather, we suggest that fractional crystallization of an evolved, intercumulus melt can explain the mineral chemistry of apatite and plag, and also the bulk compositions of Miles inclusion mesostasis and the Miles-9 felsic inclusion. We focus attention on those elements that concentrate in phosphate (the lanthanides, actinides, and Y). For these elements, phosphate crystallization will be the main control on concentrations.

Fig. 14a compares the composition of various phosphate minerals in Miles spanning the observed range of REE contents, to a model in which apatite fractionally crystallizes from the Miles 2% intercumulus melt (Fig. 13a). The models are admittedly oversimplified, as the same D-values are assumed for apatite, merrillite, and the unidentified phosphate mineral in Miles-3; as only phosphate is assumed to be crystallizing; and as the same starting composition is assumed for all inclusions. Nonetheless, the models replicate two key features of the observed phosphate compositions: (1) the Eu anomaly changes from increasingly negative to increasingly positive as the overall REE content decreases

and (2) a variety of REE patterns are produced depending on the amount of phosphate crystallized. This includes with decreasing overall REE abundance (a) LREE-enriched patterns (Miles-8B merrillite, Miles-10 apatite), (b) "V-shaped" patterns (Miles-3), and (c) "W-shaped" patterns (Miles-2) (Fig. 14a). It appears that ∼5–20% fractional crystallization of an enriched intercumulus melt can explain the observed REE and Y abundances of the various phosphate minerals in Miles (Fig. 14a). The models, however, fail to account for the variable abundances of Th and U that are observed in the phosphate minerals (Fig. 14a). This probably indicates that the actual D-values for these elements in phosphate are not similar to unity, as was assumed in the models.

If plag and apatite were in equilibrium, plag should have crystallized from the same melts that crystallized phosphate. Fig. 14b shows that plag crystallizing from the intercumulus liquid that produced phosphate can account for the average REE abundances of plag in Miles-10 (∼5–10% phosphate crystallization) and in other Miles inclusions (∼15–20% crystallization). This amount of phosphate crystallization is roughly the same as needed to explain the compositional range of phosphate minerals, consistent with co-crystallization of the two minerals. The model also explains the somewhat higher An contents for plag in Miles-10 ($An_{9.3\pm2.7}$, average ± standard deviation) compared to other inclusions ($An_{4.8\pm3.6}$) as the result of less phosphate fractionation. This model can be extended to Udei Station, which has plag with the highest REE and An contents ($An_{16.8\pm1.0}$), implying still less fractionation (Fig. 14b).

Fig. 14c compares the composition of residual melt produced by phosphate fractionation to the measured bulk compositions of inclusion mesostasis and Miles-9. The REE abundances of mesostasis and Miles-9 are very low (∼0.01–0.1× CI-chondrites), in contrast to Rb abundance and to what one might a priori expect for a sialic, evolved melt composition (Ebihara et al., 1997). Most likely these low-REE abundances are the result of phosphate crystallization. Our models suggest that ∼20–40% fractional crystallization of phosphate from an evolved intercumulus melt can explain the REE and Y abundances of mesostasis and Miles-9 (Fig. 14c). Considering that the starting intercumulus liquid corresponds to ∼98% crystallization, mesostasis and Miles-9 would thus have formed from the last ∼1% of melt to crystallize in Miles. In a petrogenetic sense these materials are indeed evolved and rhyolitic (Section 3.3.2), but unlike other evolved melts, they are REE-poor owing to removal of the REE into phosphate. Presumably, REE that were concentrated in the residual melts were able to diffuse through these melts and become incorporated into phosphate that was crystallizing elsewhere, leaving a late stage, REE-poor rhyolitic melt.

4.7. Residence time at high temperature

REE data can be used to devise simple models for the high-temperature thermal history of inclusions. Key observations include the following: (1) Clinopyroxene grains in Miles are often zoned in REE on a scale of ∼100–200 μm
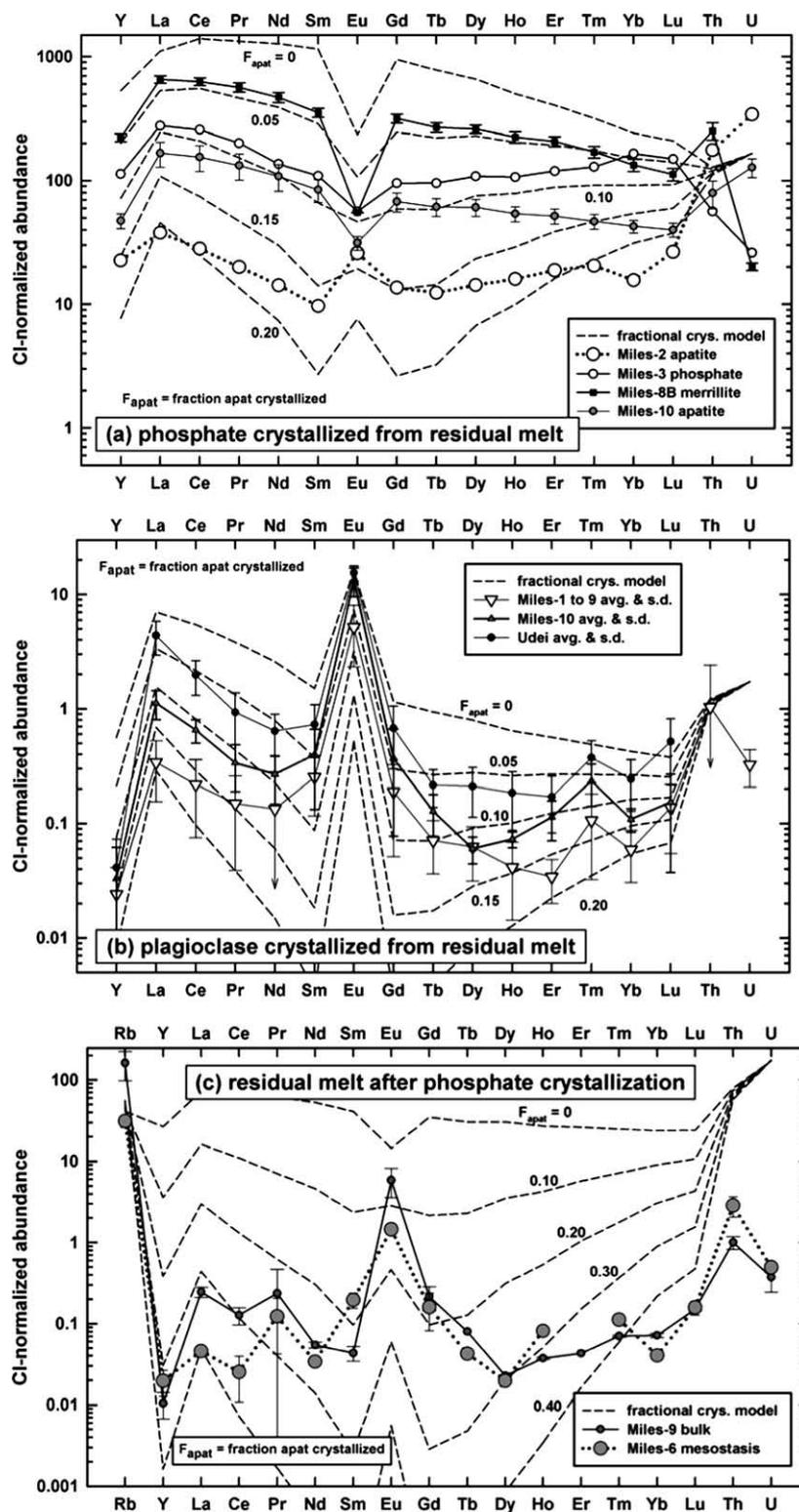
Fig. 14. CI-normalized abundance diagrams comparing the results of fractional crystallization models to observed mineral and bulk compositions in Miles. Models assume that liquid compositions were controlled by the fractional crystallization of apatite from an evolved (2% intercumulus) melt composition (Fig. 13a). F_{apat} = fraction of apatite crystallized from the melt. Errors bars in all cases are derived from 1σ standard deviations of mean phase compositions. (a) Models compared to average phosphate compositions in different Miles inclusions. (b) Models compared to average plagioclase in Miles small inclusions (1–9), Miles-10, and Udei Station. (c) Models compared to bulk Miles-9 and bulk Miles-6 mesostasis. Rb is included as an example of an incompatible element not strongly affected by apatite crystallization.

(Fig. 5c and d). (2) Clinopyroxene grain rims located within ~100 μm of cpx–plag contacts appear to have equilibrated with their surroundings at a time when intercumulus melt was present (Section 4.6). (3) Group B opx grains located within ~100 μm of metal grains in Miles-10 have different HREE contents than Group A opx (Section 3.2.1), probably as a result of redox reactions (Section 4.3) occurring at near-solidus temperatures (Section 4.6). (4) Plagioclase grains in Miles have variable REE abundances that were probably established by fractional crystallization not much above the solidus (Section 4.6). Plagioclase compositions differ significantly between different inclusions and between different pockets in Miles-10 (Section 3.2.5). The pockets range from ~200 μm to >3–10 mm across, implying that significant variations in REE content occur roughly over ~1 mm in plag, but the spatial extent of zoning in plag and any relationship to grain boundaries is poorly defined.

These observations are combined with REE diffusion data for diopside (Van Orman et al., 2001), enstatite (Cherniak and Liang, 2007), and An$_{23}$ plagioclase (Cherniak, 2003) obtained under dry conditions at 1 atm pressure to model diffusion timescales. We calculated residence times at different temperatures to result in a characteristic diffusion distance (x) of 0.1 mm in diopside, 0.1–0.2 mm in enstatite, and 1–3 mm in plagioclase, assuming a simple model with $t = x^2/2D$, where D = diffusion coefficient and t = time. The models assume Nd diffusion in plag and diopside and Gd diffusion in enstatite; other REE have similar diffusion coefficients in the case of plag (Cherniak, 2003) and enstatite (Cherniak and Liang, 2007), but the HREE diffuse an order of magnitude faster than the LREE in diopside (Van Orman et al., 2001).

At a temperature of 1150 °C, corresponding to the average equilibration temperature of cpx (Table 6), ~213 ka is needed for 0.1 mm diffusion in diopside (Fig. 15). For this same temperature and timescale, Fig. 15 shows that the REE would have diffused ~0.2 mm in enstatite and ~3 mm in plag. This is somewhat larger than the scale over which significant REE abundance variations occur in Miles opx and plag, which could be explained if the latter minerals had lower closure temperatures. At ~1100 °C, for instance, REE will diffuse ~0.1 mm in enstatite and ~1 mm in plag in ~100 ka (Fig. 15). Thus, the observed scale of spatial variation in REE for all three minerals is consistent with residence times of ~100–200 ka at temperatures of ~1100–1150 °C.
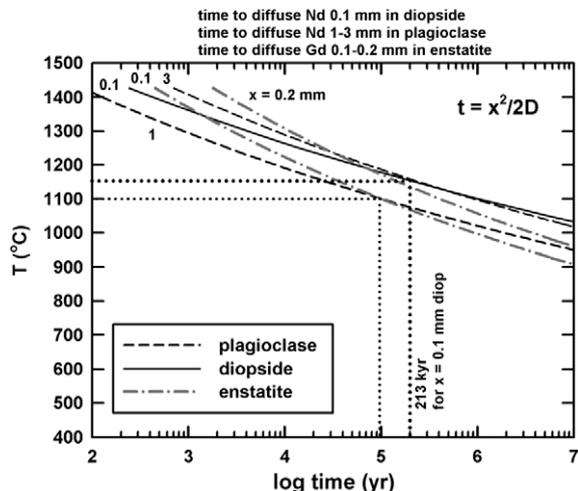
It seems likely that the actual residence time is less than these calculations imply. Diffusion coefficients increase for more sodic plag (Cherniak, 2003) as is present in Miles, so this could make the calculated timescales for plag high. The calculated timescales for diopside are also probably high, as diffusion coefficients in more iron-rich clinopyroxenes are an order of magnitude higher than for Fe-poor endmembers (Van Orman et al., 2001). Moreover, the assumed diffusion distances for all minerals could be overestimates, as an implicit assumption is that no compositional zoning occurred during crystallization and that all zoning was established following crystallization. However, some if not all zoning in plagioclase was probably established during fractional crystallization (Section 4.6), and Group B opx probably formed by reaction from a melt (Sections 4.3 and 4.6), making it unlikely that simple post-crystallization diffusion models are valid in these cases. On the other hand, this model could be largely valid for cpx rims.

Given that actual cpx diffusion rates could have been an order of magnitude higher than assumed, our best estimate for the residence time of Miles inclusions is ~20 ka at a temperature of ~1150 °C. This residence time corresponds to a condition in which cumulus pyroxene co-existed with intercumulus melt prior to the crystallization of phosphate close to the end of Stage 1 crystallization (Sections 4.4.1 and 4.6). During Stage 2 crystallization of phosphate, plag, and Group B opx, residence times at high temperatures could have been substantially shorter.

4.8. Crystallization setting and emplacement of metal and silicate lithologies

Our data have implications for the crystallization setting and emplacement of metal and silicate for Udei and Miles. We infer the same general petrogenesis for both.

The large differences in inclusion mineralogies and textures in Udei can be explained by a mixing process whereby different lithologies from separate regions of the parent body are brought together in close proximity. The best evidence for this is the juxtaposition of (a) those inclusions that have subchondritic mineralogy and bulk composition (Udei-1A-1 and -3A), with (b) those that are fractionated (Udei-1A-2, -1A-3, -1B, and -3B) (Fig. 1a and b). Most likely the fractionated inclusions were derived from a warmer portion of the parent body, where the degree of silicate partial melting reached a critical threshold to allow silicate melt–solid separation to occur, whereas the subchondritic inclusions were derived from a cooler portion of the parent body that experienced a lower degree of partial melting.

Fig. 15. Residence times at different temperatures needed to account for the diffusion of two representative REE (Nd and Gd) over different length scales (×) in diopside, plagioclase, and enstatite. Diffusion coefficients (D) are based on data from Van Orman et al. (2001), Cherniak and Liang (2007), and Cherniak (2003).

The apparent need to mix materials across different zones of the parent body implies substantial transport of material, most likely by an impact-induced process.

The silicate mixing process in Udei must have occurred no later than the time of metal emplacement, as the inclusions are embedded in metal, and thus silicate mixing also involved metal–silicate mixing. The subangular shapes of the subchondritic inclusions (e.g., Fig. 1a and b) imply a brecciation process during metal–silicate mixing in which the silicates were largely solid. On the other hand, inclusion edges are irregular in detail, with non-broken silicate minerals projecting into the metal host. Similarly, there are many euhedral and unbroken minerals embedded within the metal host. This implies that metal was fluid and that silicates were able to either grow into the metal fluid or aggregate within it. Metal–silicate mixing thus probably occurred while metal was in a fluidized state.

The petrogenesis of Udei can be thus represented by a two-stage process involving (1) variable degrees of silicate partial melting and melt migration in different areas and (2) impact-induced mixing of silicate and metallic materials while the metal was in a fluidized and probably partly molten state, with or without additional silicate melt migration. This petrogenesis is consistent with the model proposed by Benedix et al. (2000) in which a partly molten parent body experienced an impact-mixing and brecciation process.

Miles also shows evidence for early melt migration and later metal–silicate mixing. A relatively high degree of partial melting probably caused separation of silicate and metallic melt from unmelted residue and immiscible separation of silicate melt from metallic melt (Sections 4.1.2 and 4.2). Density differences would have tended to place metallic melt below silicate melt. The silicate liquids then experienced a two-stage crystallization petrogenesis, with fluidized metal enveloping and reacting with the crystal mush during Stage 2, at which time plag and phosphate fractionally crystallized out of equilibrium with previously formed minerals (Sections 4.3, 4.4, and 4.6). Thus, metal–silicate mixing occurred during Stage 2 and was probably associated with rapid cooling.

Some plag, as well as some pyroxene, could have been re-melted before plag fractionally crystallized in Stage 2. Evidence for this includes the trace-element composition of felsic glass in some inclusions of Miles (Hsu, 2003) and in other fractionated IIE irons such as Weekeroo Station (Ruzicka et al., 1999). Indirect evidence for this process is provided by the apparent contradiction between zoning data for cpx that implies that plag co-crystallized with cpx during slow Stage 1 cooling, and the composition of plag that implies crystallization of the mineral under different conditions (Sections 4.4.1 and 4.6). Re-melting was likely shock-induced (Ruzicka et al., 1999; Bogard et al., 2000; Hsu, 2003), and rapid cooling of the melt led to both glass and the spherulitic textures observed in various fractionated IIE irons (Osadchii et al., 1981; Ruzicka et al., 1999; Bogard et al., 2000; Takeda et al., 2003). Differences in plag, phosphate, and cpx compositions between inclusions imply that these inclusions began to form closed systems during the crystallization of these minerals. Most likely this was caused by the pinching of silicate melt–crystal pockets as metal crystallized around them (Sections 4.1.2 and 4.2).

Thus, for Miles it seems likely that during slow cooling in Stage 1, silicate crystal mush separated from metal somewhat, only to be re-mixed with metal by an impact process during rapid cooling in Stage 2. This model is consistent with the scenario for Colomera proposed by Takeda et al. (2003).

The overall petrology we infer for Miles and Udei is essentially the same but differs in some ways. One difference is that peak temperatures were higher for Miles than for Udei, resulting in more silicate melt for the former. Another difference is that there is more evidence for rapid cooling following metal–silicate mixing in Miles and other fractionated IIEs than in Udei and other IABs. The meteorites also differ in the amount of S they contain. The depletion of sulfide in IIE meteorites such as Miles implies that S could have been lost from the source region, possibly by impact-induced vaporization during metal–silicate mixing (Ikeda and Prinz, 1996; Ikeda et al., 1997). In contrast, sulfide minerals are abundant in Udei and other IAB/IIICD irons, possibly reflecting a S-rich parent body that did not experience much outgassing (Wasson and Wang, 1986; Choi et al., 1995; Wasson and Kallemeyn, 2002).

4.9. Models for forming IAB and IIE irons

We suggest that endogenic heating coupled with impact processes can best explain the data for IABs and IIEs. Other models involving impact-melting alone (Wasson and Wang, 1986; Choi et al., 1995; Wasson and Kallemeyn, 2002) or endogenic heating alone (Kracher, 1985; McCoy et al., 1993; Bogard et al., 2000) fail to account for all properties of the rocks.

4.9.1. Arguments against endogenic-heating-only models

(1) One problem associated with endogenic heating and the partial differentiation model for IAB/IIICD irons (Kracher, 1985) is the requirement that metallic liquids would have to significantly separate from metallic and silicate solids during relatively minor amounts of partial melting (McCoy et al., 1993). Experiments suggest that metallic melts do not easily separate from silicates unless melting is extensive or unless shear forces are present (e.g., Rushmer et al., 2000; McCoy et al., 2006). High degrees of partial melting for the IABs are clearly inconsistent with the prevalence of chondritic silicates in these meteorites and with our data for Udei, which imply <10% partial melting of silicates (Section 4.1.1).

(2) Another problem with the partial differentiation model for IABs is the absence of complementary metal- and S-poor silicate materials among meteorites, if the protoliths were chondritic. Although winonaites may correspond to a metal-poor facies of the parent body (Kracher, 1985; Benedix et al., 2000), these meteorites do not appear to be significantly depleted in metal (or their weathering products) compared to chondrites (Benedix et al., 1998). To account for the lack of "metal-poor IAB achondrites", one must postulate their complete destruction by impact comminution or conversion to a different, unrecognizable

form. Although silicate meteoroids are clearly more fragile than metal-rich ones and would be expected to more readily fragment, given the large number of IABs (Chabot and Haack, 2006) one might still expect a reasonable fraction of the IAB complementary materials to have survived and been sampled as meteorites. The same argument applies less strongly to the less numerous IIE irons.

(3) Endogenic heating models for the fractionated IIEs (Wasserburg et al., 1968; Bogard et al., 2000) leave unclear why metal and silicate would not separate if substantial melting was caused by an internal heat source that presumably operated over a finite duration. The only way to avoid metal–silicate separation in this case would be to invoke inefficient metal–silicate separation. However, based on data for Miles it appears that metal + sulfide could have been ~60% molten and silicates ~30% molten at peak heating, which probably should have enabled some metal–silicate separation (Sections 4.1.2 and 4.2). Metal would become trapped with silicates if cooling rates were high (Section 4.2), but there is no reason to suspect that this would be the case in the interior of an endogenically heated parent body.

(4) For endogenic heating, cooling rates might be expected to be slow throughout crystallization. This is inconsistent with the inferred thermal histories of fractionated IIEs (Section 4.8; Ikeda et al., 1997; Ruzicka et al., 1999; Takeda et al., 2003), which involve rapid cooling following a long period of diffusional exchange at high temperature.

4.9.2. Arguments against impact-melting-only models

(1) The impact-melting model has difficulty in explaining the characteristics of the silicates. To create the silicates in the fractionated IIEs and the mineralogically similar Guin and Sombrerete irons by impact-melting alone would require preferential formation and separation of feldspathic liquids by collision, possibly in a manner analogous to that which produced feldspathic shock-melt pockets in ordinary chondrites (Rubin et al., 1986). However, the silicate inclusions in IIEs do not closely resemble the compositions of the melt pockets (Ruzicka et al., 1999). Moreover, Keil et al. (1997) argued that impact processes do not create significant amounts of fractionated melt, and the inclusions have much larger volumes than the pockets (by 3–8 orders of magnitude). In the case of IABs, the large number of inclusions with unfractionated character is problematic for a model invoking repeated impact-melting of metal, as it implies just the right amount of heating to melt and fluidize metal but not silicate.

(2) Impact heating alone has difficulty explaining the inferred thermal histories of fractionated IIEs which involve crystallization of coarse pyroxene under quasi-equilibrium conditions followed by a second stage of more rapid cooling. Rubin et al. (1986) recognized the apparent need for a two-step process to create silicate inclusions in Guin and suggested two separate impact-melting events, one to create a melt that crystallized coarse pyroxene and another to create finer-grained feldspar. This is possible, but there is no obvious reason why the same process would produce first slowly solidified melt, and then rapidly solidified melt. Moreover, it is unlikely that this would have occurred by

chance for each silicate-bearing IIE iron if each had formed in a separate melt pool.

(3) The absence of metal-poor achondrite rocks complementary to the IAB and IIE irons cannot be explained by impact-melting alone without invoking some other mechanical fractionation process. This problem was discussed above for models involving only endogenic heating.

4.9.3. Scenario for IAB/IIICD/winonaite meteorites

For the IAB/IIICD/winonaite parent body, we hypothesize that a major collision occurred while the body was being internally heated. We suggest that prior to collision, the interior was partly molten but only slightly above the silicate solidus. Under these conditions, metallic melt had difficulty separating, but limited silicate melt–solid separation could have occurred, and some metallic melt could have drained to form an incipient core prior to impact (Fig. 16a). We infer that a major collision then unroofed the uppermost, cooler, and more brittle part of the parent body (Fig. 16a). Either the surviving body was disrupted and (quickly) reassembled (Benedix et al., 2000), or it was left largely intact but significantly scrambled. Impact stress waves mobilized metal and caused metal–silicate mixing, and metallic melt + solid was forcefully injected into silicate to form Copiapo-type breccias such as Udei Station. The removal of the uppermost portion of the parent body depressurized the interior, allowing CO gas to partly escape, which could have enabled further movement of metallic and silicate melt (Section 4.1.1). Removal of the upper portion of the parent body would have destroyed those silicate-rich materials that are not sampled as meteorites. This process also exposed warm material from the interior to cold space and caused more rapid cooling at high temperature. If the parent body was not totally disrupted, gas loss would be limited to the upper portions.

We suggest that the parent body remaining after collisional unroofing was mineralogically zoned, as a result of processes occurring after and to some extent before collision. We infer not only that winonaites were derived from outer portions of the parent body (Kracher, 1985), but also that Ni-poor IAB/IIICD irons were derived from a central, deep portion, and that Ni-rich IAB/IIICD irons were derived from an intermediate zone (Fig. 16a). This structure is consistent with correlations between metal bulk Ni content and various parameters, including (a) higher cooling rates for metal in Ni-rich irons (Herpfer et al., 1994) that were closer to the surface of the parent body, (b) older I–Xe ages and ^{39}Ar–^{40}Ar ages for bulk silicates in Ni-rich irons (Niemeyer, 1979a,b) and winonaites (Benedix et al., 1998) that reached closure temperature sooner as a result of more rapid cooling closer to the surface of the parent body, (c) C and S contents that are higher for Ni-poor irons (Bunch et al., 1970; see also Choi and Wasson, 1994; Benedix et al., 1995), possibly as a result of less degassing in more deeply buried material, and (d) a higher proportion of brecciated Copiapo-type inclusions in Ni-rich irons (Bunch et al., 1970), possibly as a result of mixing a higher proportion of cooler silicate from upper portions of the pre-impact body. If higher Ni contents in metal correspond to a higher metallic melt component (Kracher, 1985; Wasson
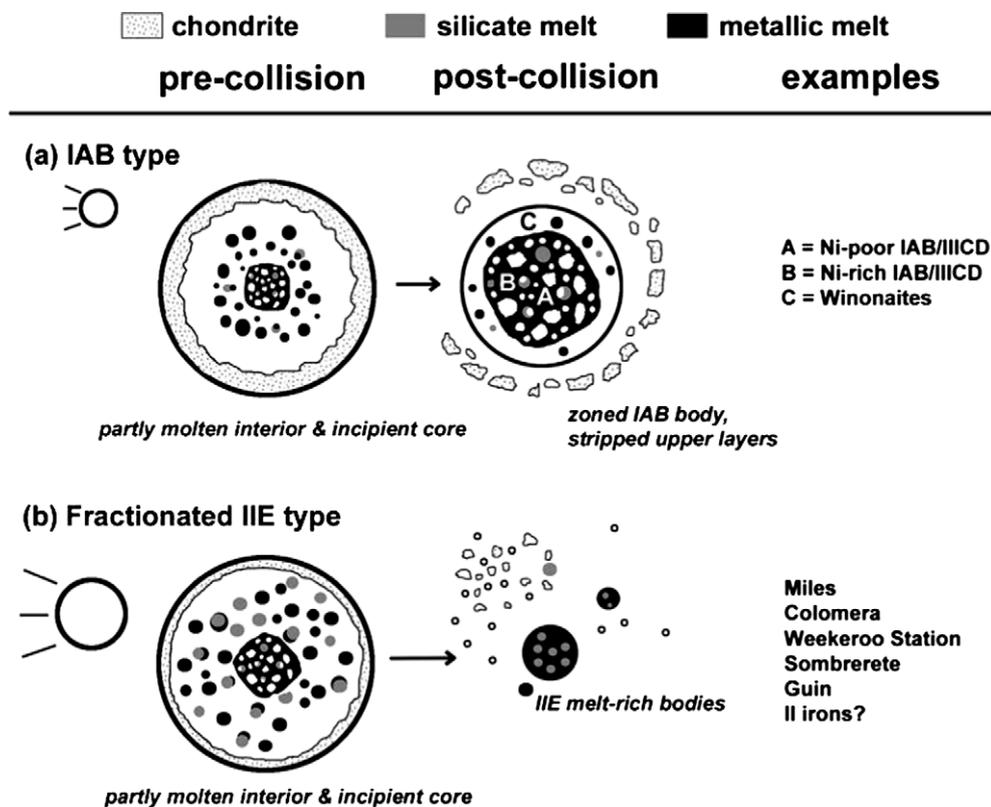
Fig. 16. Cartoon showing the proposed evolution of (a) IAB type and (b) fractionated IIE type silicate-bearing irons, involving major disruptive collisions of partly molten planetesimals being heated endogenically (see text). White areas in pre- and post-collision bodies represent solid material (chiefly olivine).

and Kallemeyn, 2002), then metallic melt in the metal-rich interior of the remnant body was concentrated *upward* relative to metallic solid. This is as one would expect based on density differences, but opposite to previous models (Kracher, 1985; Choi et al., 1995; Wasson and Kallemeyn, 2002).

4.9.4. Scenario for fractionated IIE meteorites

For the fractionated IIE parent body, we hypothesize that a major collision occurred while the body was being internally heated to temperatures significantly above the silicate solidus. Prior to collision, the parent body consisted of a crystal mush composed of both molten silicate and metal and solid metal and silicate, with roughly equal parts metallic melt and silicate melt and a larger portion of solid silicate (mainly olivine) and a smaller portion of solid metal. We suggest that the metallic and silicate melts separated from the residue to some extent owing to a relatively high proportion of melting (e.g., 30% partial melting of silicate and 60% partial melting of metal–sulfide in the Miles source area – Sections 4.1.2 and 4.2). Metallic melt would have a tendency to sink downwards and may have formed an incipient core, but melt pod "plums" consisting of silicate melt overlying metallic melt may have been present throughout the largely solid interior (Fig. 16b). Magmatic temperatures were high for a long time period and silicate grains crystallized and grew in a quasi-equilibrium condition. We infer that a major collision then catastrophically

disrupted the original parent body. Some feldspathic materials were re-melted, and significant degassing and loss of S occurred as hot material was depressurized and exposed to cold space. A smaller secondary melt-rich body, which may have been derived largely from the incipient core of the primary body or from one or more of the hypothesized "plums", quickly re-accreted from the debris, and consisted largely of metallic melt with some entrained silicate crystal mush (Fig. 16b). This secondary body was the immediate precursor to the fractionated IIEs. Solid olivine was largely lost during the break-up process, possibly because it was accelerated differently than liquids during impact (Ruzicka and Hutson, 2006) or because it was dispersed as dust.

4.9.5. Collision during endogenic heating

Collision during endogenic heating provides the mechanisms and conditions needed to enable some differentiation but to arrest complete differentiation. This model for IABs and fractionated IIEs avoids all of the problems identified for impact-only and endogenic-heating-only models. Additional advantages include the following: (1) There is little doubt that the main heat source, ^{26}Al decay, could have provided the necessary heat to enable differentiation if accretion occurred sufficiently early. The reason that many IABs were heated to the same extent just above the silicate solidus, and that fractionated IIEs were heated to a greater extent, is that they formed in the deep interiors of nearly isothermal parent bodies that were being heated

endogenically. Differences in maximum temperatures can be explained by the timing of accretion (hotter for faster accretion). (2) A major impact provides the mechanism to mobilize partly molten metal and to result in metal–silicate mixing. For the IABs, this impact scrambled materials from different depths in the parent body, and removed weakly heated or silicate-rich materials from the upper portion of the original parent body. For the IIEs, it allowed separation of liquid-rich silicate and metallic materials from solid olivine. (3) The inferred two-stage magmatic cooling history for IIEs, first slow cooling and then more rapid cooling, is best accommodated by a change in crystallization setting, from the deep interior of a well-insulated body, to cooling in small dispersed fragments or in a smaller or less well-insulated body. This implies a parent body break-up process. (4) The rapid cooling that is initiated during collisional disruption provides a mechanism to prevent metal–silicate separation immediately after metal is mobilized. Metal liquids will cool and crystallize sufficiently fast to effectively trap enclosed silicates. (5) The same basic model can explain other silicate-bearing irons by including variations in maximum heating temperature during collision, the extent of parent body disruption, and the size of the secondary body that is produced. For example, the Steinbach IVA stony iron and the IVA irons can be produced by crystallization in a relatively large secondary melt body after a collision at high temperature (Ruzicka and Hutson, 2006), and the Sombrerete ungrouped iron can be produced by crystallization in a small, more rapidly cooled secondary melt body after a collision at lower temperature (Ruzicka et al., 2006).

5. CONCLUSIONS

The results of chemical and petrographic studies of silicate inclusions in the Udei Station (IAB) and Miles (fractionated IIE) silicate-bearing irons suggest that the meteorites experienced broadly similar but not identical petrogeneses. Chondritic protoliths for both meteorites were partly melted, but inclusions in Miles were formed from a single parental melt of mafic composition that was generated by ∼30% partial melting at a peak temperature of ∼1250 °C, whereas inclusions in Udei Station include both lithologies that are residues (harzburgite) as well as those that crystallized from partial melts (feldspathic orthopyroxenite, basalt/gabbro). Portions of Udei Station experienced ∼3–10% equilibrium partial melting of a chondritic protolith at a peak temperature <1180 °C. Silicates in both meteorites were mixed with metal while the latter was in a fluidized state, and redox reactions occurred between the silicate and metal, but these reactions proceeded to a greater extent in Miles. During these reactions, clinopyroxene and P-bearing metal were partly consumed, and phosphate, silica, and a second generation of orthopyroxene minerals were produced. Mineral compositions in Udei Station and Miles reflect partial equilibration under magmatic conditions, but these conditions were different in the two meteorites. In Udei Station, plagioclase and orthopyroxene approached equilibrium with one another, but were out of equilibrium with olivine and clinopyroxene. In Miles, slowly crystallizing minerals (orthopyroxene, clinopyroxene, chromite, and olivine) partly equilibrated with an enriched intercumulus melt, whereas plagioclase and phosphate formed out of equilibrium with other minerals by fractional crystallization during more rapid cooling of an evolved melt composition. We suggest that a model involving collisions of endogenically heated planetesimals can best explain the data for Udei Station, Miles, and other silicate-bearing irons. We infer that major, disruptive collisions of the original IAB and IIE planetesimals occurred while they were partly molten, resulting in smaller secondary parent bodies from which the meteorites were derived.

APPENDIX A. SUPPLEMENTARY DATA

Supplementary data associated with this article can be found, in the online version, at doi:10.1016/j.gca.2009.09.019.

REFERENCES

Anders E. and Grevesse N. (1989) Abundances of the elements: meteoritic and solar. *Geochim. Cosmochim. Acta* **53**, 197–214.

Benedix G. K., McCoy T. J. and Keil K. (1995) Silicate inclusions in IAB irons: correlations between metal composition and inclusion properties, and inferences for their origin. *Meteoritics* **30**, 485 (abstr.).

Benedix G. K., McCoy T. J., Keil K., Bogard D. D. and Garrison D. H. (1998) A petrologic and isotopic study of winonaites: evidence for early partial melting, brecciation, and metamorphism. *Geochim. Cosmochim. Acta* **62**, 2535–2553.

Benedix G. K., McCoy T. J., Keil K. and Love S. G. (2000) A petrologic study of the IAB iron meteorites: constraints on the formation of the IAB–winonaite parent body. *Meteorit. Planet. Sci.* **35**, 1127–1141.

Benedix G. K., Lauretta D. S. and McCoy T. J. (2005) Thermodynamic constraints on the formation conditions of winonaites and silicate-bearing IAB irons. *Geochim. Cosmochim. Acta* **69**, 5123–5131.

Bild R. W. (1977) Silicate inclusions in group IAB irons and a relation to the anomalous stones Winona and Mt. Morris (Wis). *Geochim. Cosmochim. Acta* **41**, 1439–1456.

Bogard D. D., Garrison D. H. and McCoy T. J. (2000) Chronology and petrology of silicates from IIE iron meteorites: evidence of a complex parent body evolution. *Geochim. Cosmochim. Acta* **64**, 2133–2154.

Bunch T. E., Keil K. and Olsen E. (1970) Mineralogy and petrology of silicate inclusions in iron meteorites. *Contrib. Mineral. Petrol.* **25**, 297–340.

Casanova I., Graf T. and Marti K. (1995) Discovery of an unmelted H-chondrite inclusion in an iron meteorite. *Science* **268**, 540–542.

Chabot N. L. and Haack H. (2006) Evolution of asteroidal cores. In *Meteorites and the Early Solar System II* (eds. D. S. Lauretta and H. Y. McSween Jr.). University of Arizona Press, Tucson, pp. 747–771.

Cherniak D. J. (2003) REE diffusion in feldspar. *Chem. Geol.* **193**, 25–41.

Cherniak D. J. and Liang Y. (2007) Rare earth element diffusion in natural enstatite. *Geochim. Cosmochim. Acta* **71**, 1324–1340.

Choi B.-G. and Wasson J. T. (1994) Role of C during the formation of IAB-IIICD iron meteorites. *Meteoritics* **29**, 456–457 (abstr.).

Choi B.-G., Ouyang X. and Wasson J. T. (1995) Classification and origin of IAB and IIICD iron meteorites. *Geochim. Cosmochim. Acta* **59**, 593–612.

Clayton R. N. and Mayeda T. K. (1996) Oxygen isotope studies of achondrites. *Geochim. Cosmochim. Acta* **60**, 1999–2017.

Curtis D. B. and Schmitt R. A. (1979) The petrogenesis of L-6 chondrites: insights from the chemistry of minerals. *Geochim. Cosmochim. Acta* **43**, 1091–1103.

Doan A. S. and Goldstein J. I. (1970) The ternary phase diagram, Fe–Ni–P. *Metall. Trans.* **1**, 1759–1767.

Ebihara M., Ikeda Y. and Prinz M. (1997) Petrology and chemistry of the Miles IIE iron: II. Chemical characteristics of the Miles silicate inclusions. *Antarct. Meteorite Res.* **10**, 373–388.

Fish R. A., Goles G. G. and Anders E. (1960) The record in the meteorites: III. On the development of meteorites in asteroidal bodies. *Astrophys. J.* **132**, 243–258.

Floss C., James O. B., McGee J. J. and Crozaz G. (1998) Lunar ferroan anorthosite petrogenesis: clues from trace element distributions in FAN subgroups. *Geochim. Cosmochim. Acta* **62**, 1255–1283.

Green T. H., Blundy J. D., Adam J. and Yaxley G. M. (2000) SIMS determination of trace element partition coefficients between garnet, clinopyroxene and hydrous basaltic liquids at 2–7.5 GPa and 1080–1200 °C. *Lithos* **53**, 165–187.

Haack H. and McCoy T. J. (2005) Iron and stony-iron meteorites. In *Treatise on Geochemistry, vol. 1: Meteorites, Comets, Planets* (ed. A. M. Davis). Elsevier, Oxford, pp. 325–345.

Hansen M. and Anderko K. (1958) *Constitution of Binary Alloys.* McGraw-Hill, New York.

Harlow G. E., Delaney J. S., Nehru C. E. and Prinz M. (1982) Metamorphic reactions in mesosiderites: origin of abundant phosphate and silica. *Geochim. Cosmochim. Acta* **46**, 339–348.

Herpfer M. A., Larimer J. W. and Goldstein J. I. (1994) A comparison of metallographic cooling rate methods used in meteorites. *Geochim. Cosmochim. Acta* **58**, 1353–1365.

Hsu W. (2003) Rare earth element geochemistry and petrogenesis of Miles (IIE) silicate inclusions. *Geochim. Cosmochim. Acta* **67**, 4807–4821.

Ikeda Y. and Prinz M. (1996) Petrology of silicate inclusions in the Miles IIE iron. *Proc. NIPR Symp. Antarct. Meteorites* **9**, 143–173.

Ikeda Y., Ebihara M. and Prinz M. (1997) Petrology and chemistry of the Miles IIE iron: I. Description and petrology of twenty new silicate inclusions. *Antarct. Meteorite Res.* **10**, 355–372.

Keil K. and Wilson L. (1993) Explosive volcanism and the compositions of cores of differentiated asteroids. *Earth Planet. Sci. Lett.* **117**, 111–124.

Kelly W. R. and Larimer J. W. (1977) Chemical fractionation in meteorites: VIII. Iron meteorites and the cosmochemical history of the metal phase. *Geochim. Cosmochim. Acta* **41**, 93–111.

Keil K., Stöffler D., Love S. G. and Scott E. R. D. (1997) Constraints on the role of impact heating and melting in asteroids. *Meteorit. Planet. Sci.* **32**, 349–363.

Kong P. and Ebihara M. (1997) The origin and nebular history of the metal phase of ordinary chondrites. *Geochim. Cosmochim. Acta* **61**, 2317–2329.

Kracher A. (1985) The evolution of partially differentiated planetesimals: evidence from iron meteorite groups IAB and IIICD.

In *Proceedings of the 15th Lunar and Planetary Science Conference.* pp. 689–698.

Le Maitre R. W. (1976) The chemical variability of some common igneous rocks. *J. Petrol.* **17**, 589–637.

Lindsley D. H. (1983) Pyroxene thermometry. *Am. Mineral.* **68**, 477–493.

Lindsley D. H. and Andersen D. J. (1983) A two-pyroxene thermometer. In *Proceedings of the 13th Lunar and Planetary Science Conference.* pp. 887–906.

McCoy T. J., Keil K., Scott E. R. D. and Haack H. (1993) Genesis of the IIICD iron meteorites: evidence from silicate-bearing inclusions. *Meteoritics* **28**, 552–560.

McCoy T. J., Mittlefehldt D. W. and Wilson L. (2006) Asteroid differentiation. In *Meteorites and the Early Solar System II* (eds. D. S. Lauretta and H. Y. McSween Jr.). University of Arizona Press, Tucson, pp. 733–745.

Mittlefehldt D. W., McCoy T. J., Goodrich C. A. and Kracher A. (1998) Non-chondritic meteorites from asteroidal bodies. In *Planetary Materials*, vol. 36 (ed. J.J. Papike). Reviews in Mineralogy, Mineralogical Society of America. pp. 4-1–4-195.

Murrell M. T. and Burnett D. S. (1983) The behavior of actinides, phosphorus, and rare earth elements during chondrite metamorphism. *Geochim. Cosmochim. Acta* **47**, 1999–2014.

Niemeyer S. (1979a) I–Xe dating of silicate and troilite from IAB iron meteorites. *Geochim. Cosmochim. Acta* **43**, 843–860.

Niemeyer S. (1979b) ^{40}Ar–^{39}Ar dating of inclusions from IAB iron meteorites. *Geochim. Cosmochim. Acta* **43**, 1829–1840.

Olsen E., Davis A., Clarke, Jr., R. J., Schultz L., Weber H. W., Clayton R., Mayeda T., Jarosewich E., Sylvester P., Grossman L., Wang M.-S., Lipschutz M. E., Steele I. M. and Schwade J. (1994) Watson: a new link in the IIE iron chain. *Meteoritics* **29**, 200–213.

Osadchii Eu. G., Baryshnikova G. V. and Novikov G. V. (1981) The Elga meteorite: silicate inclusions and shock metamorphism. *Proc. Lunar Planet. Sci.* **12B**, 1049–1068.

Rubin A. E., Jerde E. A., Zong P., Wasson J. T., Westcott J. W., Mayeda T. and Clayton R. N. (1986) Properties of the Guin ungrouped iron meteorite: the origin of Guin and of group-IIE irons. *Earth Planet. Sci. Lett.* **76**, 209–226.

Rushmer T., Minarik W. G. and Taylor G. J. (2000) Physical processes of core formation. In *Origin of the Earth and Moon* (eds. R. M. Canup and K. Righter). University of Arizona Press, Tucson, pp. 227–243.

Ruzicka A. and Hutson M. (2006) Differentiation and evolution of the IVA meteorite parent body: clues from pyroxene geochemistry in the Steinbach stony-iron meteorite. *Meteorit. Planet. Sci.* **41**, 1959–1987.

Ruzicka A., Fowler G. W., Snyder G. A., Prinz M., Papike J. J. and Taylor L. A. (1999) Petrogenesis of silicate inclusions in the Weekeroo Station IIE iron meteorite: differentiation, remelting and dynamic mixing. *Geochim. Cosmochim. Acta* **63**, 2123–2143.

Ruzicka A., Kilgore M., Mittlefehldt D. W. and Fries M. D. (2005) Portales Valley: petrology of a metallic-melt meteorite breccia. *Meteorit. Planet. Sci.* **40**, 261–295.

Ruzicka A., Hutson M. and Floss C. (2006) Petrology of silicate inclusions in the Sombrerete ungrouped iron meteorite: implications for the origins of IIE-type silicate-bearing irons. *Meteorit. Planet. Sci.* **41**, 1797–1831.

Seitz H.-M., Altherr R. and Ludwig T. (1999) Partitioning of transition elements between orthopyroxen and clinopyroxene in peridotitic and webseritic xenoliths: new empirical geothermometers. *Geochim. Cosmochim. Acta* **63**, 3967–3985.

Takeda H., Bogard D. D., Mittlefehldt D. W. and Garrison D. H. (2000) Mineralogy, petrology, chemistry, and ^{39}Ar–^{40}Ar and exposure ages of the Caddo County IAB iron: evidence for

early partial melt segregation of a gabbro area rich in plagioclase-diopside. *Geochim. Cosmochim. Acta* **64**, 1311–1327.

Takeda H., Hsu W. and Huss G. R. (2003) Mineralogy of silicate inclusions of the Colomera IIE iron and crystallization of Cr-diopside and alkali feldspar from a partial melt. *Geochim. Cosmochim. Acta* **67**, 2269–2288.

Taylor G. J., Keil K., McCoy T., Haack H. and Scott E. R. D. (1993) Asteroid differentiation: pyroclastic volcanism to magma oceans. *Meteoritics* **28**, 34–52.

Treiman A. H. (1996) The perils of partition: difficulties in retrieving magma compositions from chemically equilibrated basaltic meteorites. *Geochim. Cosmochim. Acta* **60**, 147–155.

Usselman T. M. (1975) Experimental approach to the state of the core: Part I. The liquidus relations of the Fe-rich portion of the Fe–Ni–S system from 30 to 100 kb. *Am. J. Sci.* **275**, 278–290.

Van Orman J. A., Grove T. L. and Shimizu N. (2001) Rare earth element diffusion in diopside: influence of temperature, pressure, and ionic radius, and an elastic model for diffusion in silicates. *Contrib. Mineral. Petrol.* **141**, 687–703.

Vogel N. and Renne P. R. (2008) ^{40}Ar–^{39}Ar dating of plagioclase grain size separates from silicate inclusions in IAB iron meteorites and implications for the thermochronological evolution of the IAB parent body. *Geochim. Cosmochim. Acta* **72**, 1231–1255.

Wasserburg G. J., Sanz H. G. and Bence A. E. (1968) Potassium-feldspar phenocrysts in the surface of Colomera, and iron meteorite. *Science* **161**, 684–686.

Wasson J. T. and Kallemeyn G. W. (2002) The IAB iron–meteorite complex: a group, five subgroups, numerous grouplets, closely related, mainly formed by crystal segregation in rapidly cooling melts. *Geochim. Cosmochim. Acta* **66**, 2445–2473.

Wasson J. T. and Wang J. (1986) A nonmagmatic origin of group-IIE iron meteorites. *Geochim. Cosmochim. Acta* **50**, 725–732.

Wasson J. T., Willis J., Wai C. M. and Kracher A. (1980) Origin of iron meteorite groups IAB and IIICD. *Z. Naturforsch.* **35**, 781–795.

Witt-Eickschen G. and O'Neill H. St. C. (2005) The effect of temperature on the equilibrium distribution of trace elements between clinopyroxene, orthopyroxene, olivine and spinel in upper mantle peridotite. *Chem. Geol.* **221**, 65–101.

Associate editor: Alexander N. Krot

ELECTRONIC ANNEX for "Comparative petrology of silicates in the Udei Station (IAB) and Miles (IIE) iron meteorites: Implications for the origin of silicate-bearing irons", by Alex Ruzicka and Melinda Hutson

Contents:

Section 1. Details on the experimental methods and data reduction.

Section 2. Database of mineral/melt partition coefficients.

Section 3. Major and minor-element mineral chemistry.

Section 4. Determination of equilibrium mineral compositions in polymineralic systems, using an exchange model.

Electronic Annex, Section 1: Details on the experimental methods and data reduction.

Modal analysis, bulk compositions, and electron microprobe analysis

Point counts of silicate and phosphate minerals were primarily obtained using BSE image mosaics; counts of metal, sulfide, and oxide minerals were obtained using reflected light image mosaics. These were combined to give an overall mode. For inclusion Udei-1B, plagioclase and clinopyroxene proportions were determined by using a thin section scanner image which showed the distribution of the two phases in transmitted light (clinopyroxene appeared green, plagioclase white). Area fractions derived by point counting were assumed to be equivalent to volume fractions.

Electron microprobe data were reduced with the nominal Cameca PAP procedure (Pouchou and Pichoir, 1985, 1991). For Udei Station, EMP analyses of olivine, pyroxene, and plagioclase were obtained in ~1-µm-diameter spots using a 30 nA beam current as measured in a Faraday cup. For Miles, EMP analyses of olivine, pyroxene, and chromite were obtained in ~1-µm-diameter spots using a 50 nA current, and analyses of feldspar and phosphate were obtained in ~4-10-µm-diameter spots using a 10-30 nA current. Analysis of bulk inclusion mesostasis in Miles was obtained by averaging EMPA data for 20-µm-diameter spots obtained in a grid pattern.

The modal data were combined with mineral densities and measured phase compositions to determine bulk compositions. The following mineral densities (ρ, in g/cm^3) were assumed based on data from Gaines et al. (1997) and measured phase compositions: ρ olivine = 3.30 (Udei) - 3.46 (Miles), ρ orthopyroxene = 3.26 (Udei) - 3.36 (Miles), ρ clinopyroxene = 3.28 (Udei, diopside) - 3.17 (Miles), ρ plagioclase = 2.64 (Udei) - 2.62 (Miles), ρ k-feldspar = 2.54, ρ SiO$_2$ phase = 2.3, ρ mesostasis = 2.4, ρ phosphate = 3.2, ρ chromite = 5.1.

Trace element analyses

LA-ICP-MS data for Miles were obtained in four shifts between July 2002 and July 2004, and data for Udei Station were obtained in a single shift in March, 2008. The laser was operated with a forward power of 1340 W and pulse times of 4 Hz for Miles and 3 Hz for Udei Station. Measured species included isotopes of elements with strong lithophile tendency (^{43}Ca, ^{45}Sc, ^{47}Ti, ^{51}V, ^{53}Cr, ^{55}Mn, ^{59}Co, ^{69}Ga, ^{88}Sr, ^{89}Y, ^{90}Zr, ^{93}Nb, ^{137}Ba, ^{139}La, ^{140}Ce, ^{141}Pr, ^{147}Sm, ^{153}Eu, ^{157}Gd, ^{159}Tb, ^{163}Dy, ^{165}Ho, ^{166}Er, ^{169}Tm, ^{172}Yb, and ^{175}Lu for both meteorites; ^{66}Zn, ^{85}Rb , ^{133}Cs, ^{178}Hf, ^{232}Th, and ^{238}U for Miles only; and ^{27}Al, ^{29}Si, ^{86}Sr, ^{138}Ba for Udei Station only). For Udei Station, data for ^{88}Sr and ^{138}Ba provided better counting statistics than ^{86}Sr and ^{137}Ba, and the former isotopes were used to determine concentrations. In addition, ^{60}Ni data were obtained for both meteorites as a monitor for potential metal inclusions within analysis volumes, and ^{82}Se data were obtained for Udei Station as a monitor for troilite inclusions, although in most analyses contamination by troilite or metal appears to have been minimal. Analyses of unknowns were interleaved in the same run with analyses of glass standards (NIST 612 for Miles, and NIST 610 for Udei Station). Element concentrations for the standards were taken from Pearce et al. (1997). Concentrations for unknowns derived by LA-ICP-MS were normalized to that obtained by prior microprobe analysis, using Si as a normalizing element for analyses of Udei Station, and by using a variety of normalizing elements for Miles depending on the phase being analyzed (Ca for analyses of pyroxene, plagioclase, phosphate, and mesostasis; Mn for olivine; Cr for chromite; and Ti for K-feldspar). Selection criteria were applied to remove from consideration those elements in a given analysis that were above background counts but that had large (>70%) theoretical counting errors, or that had large variations in net count rates during pulsed laser firing shots (>300% relative standard deviation between six even time "subset" intervals after normalization to another isotope used as an internal standard). Large temporal variations in count rates during ablation reflect either poor counting statistics or the presence of sporadic inclusions in the analysis volume. Finally, data for elements whose concentrations were

unusually high for the phase being analyzed were also excluded. This included the LREE, Th, and U for some analyses of orthopyroxene adjacent to a large apatite in inclusion Miles-5 cut by weathering veins, and more commonly Co in analyses of plagioclase in Miles cut by weathering veins.

References

Gaines R.V., Skinner H.C.W., Foord E.E., Mason B. and Rosenzweig A. (1997) *Dana's New Mineralogy, The System of Mineralogy of James Dwight Dana and Edward Salisbury Dana*, Eight Edition. John Wiley & Sons, New York.

Pearce J.G., Perkins W.T., Westgate J.A., Gorton M.P., Jackson S.E., Neal C.R. and Chenery S.P. (1997) A compilation of new and published major and trace element data for NIST SRM 610 and NIST SRM 612 glass reference materials. *Geostandards and Geoanalytical Res.* **21**, 115-144.

Pouchou J.L. and Pichoir F. (1985) "PAP" $\phi(\rho Z)$ procedure for improved quantitative microanalysis. In *Microbeam Analysis* (ed. J.T. Armstrong). San Francisco Press, Inc., San Francisco. pp. 104-106.

Pouchou, J.-L., and Pichoir, F. (1991) Quantitative analysis of homogeneous or stratified microvolumes applying the model "PAP". In *Electron Microprobe Quantitation* (eds. K.F.J. Heinrich. and D.E. Newbury). Plenum Press, New York. pp. 31-75.

Electronic Annex, Section 2: Database of mineral/melt partition coefficients.

Table EA-1: Mineral/melt partition coefficients assumed in this study. Large bolded values represent arithmetic averages of selected literature data, with standard deviations given in parentheses and reference numbers given in square brackets. Values for REE elements were interpolated in some cases. Phosphate data mainly for apatite. Clearly discrepant values were excluded before averaging, and preference was given to determinations made by laboratory experiments at low pressures and reducing conditions utilizing mafic or ultramafic bulk compositions.

	Olivine	orthopyroxene	clinopyroxene	plagioclase	phosphate	chromite
Al	**0.0071** *(0.0039)* [2,4,14,19,20,23,29,31]	**0.074** *(0.055)* [1,4,14,23,31]	**0.32** *(0.21)* [1,20,23,29,42]	**1.67** *(0.12)* [20,29,31,56]	--	--
Si	**0.81** *(0.06)* [1,2,4,14,22,23,29,31]	**0.96** *(0.11)* [1,14,23,31]	**0.96** *(0.03)* [1,20,23,29,42]	**1.0** *(0.10)* [20,29,31,56]	**0.012** *(0.011)* [64,66,68]	--
Ca	**0.025** *(0.006)* [1,2,4,7,14,15,18,19,22, 23,26,31]	**0.065** *(0.052)* [1,4,14,26,31]	**1.57** *(0.59)* [1,20,23,42]	**1.68** *(0.33)* [20,29,31,56,57,61]	--	--
Sc	**0.24** *(0.11)* [2,4,14,15,17,20,23,24, 28,29]	**0.46** *(0.21)* [4,14,28]	**2.1** *(0.9)* [20,23,24,28,29,42,44, 45,46,52]	**0.025** *(0.023)* [24,29,32,58,61]	**0.34** *(0.10)* [24,46,65,66]	**0.49** [69]
Ti	**0.024** *(0.019)* [1,3,6,7,14,15,27,28,29]	**0.11** *(0.02)* [1,14,23,28,31]	**0.29** *(0.09)* [1,3,6,7,23,27,28,42,44, 45,47,52]	**0.046** *(0.017)* [3,8,29,56,58,61]	**0.1** [66]	**3.6** [70]
V	**0.114** *(0.088)* [3,5,6,12,14,20,27,28]	**1.00** *(0.10)* [8,14,28]	**1.92** *(0.86)* [3,5,6,27,28,44,45]	**0.063** *(0.052)* [3,8]	--	**38** [71]
Cr	**1.13** *(0.66)* [2,3,5,12,14,15,17,21, 22,26,29,31]	**3.36** *(1.87)* [1,8,14,21,26,31,33,35]	**4.27** *(1.59)* [20,26,27,29,44,45,46]	**0.053** *(0.026)* [3,8,29,56,61]	**0.18** [46]	**77** [71]
Mn	**1.05** *(0.31)* [1,2,3,4,7,10,12,14,15, 16,17,20,23,30]	**0.69** *(0.44)* [1,4,14]	**1.15** *(0.35)* [3,6,7,20,23,24,42]	**0.045** *(0.027)* [3,24,58]	**0.13** [24]	**24** [70]
Co	**3.60** *(1.59)* [2,3,5,6,9,12,14,15,17, 20,24,29]	**1.32** *(0.54)* [14,35]	**1.13** *(0.14)* [3,5,6,20,24,29,46]	**0.056** *(0.030)* [3,24,29,32,58,61]	**0.2** [66]	**6.4** [69]
Zn	**1.00** *(0.39)* [3,5,10,15,16,20,24]	**3.55** *(0.22)* [32,34]	**0.42** *(0.10* [3,5,20,24]	**0.16** *(0.06)* [3,24,34]	**1.8** [65]	**4** [69]
Ga	**0.03** *(0.01)* [15,58]	**0.28** [34]	**0.67** *(0.11)* [34,44]	**1.36** *(0.36)* [24,34,59]	**0.25** [24]	**3.2** [69]

Rb	0.0058 (0.0040) [8,13,25]	0.035 (0.020) [25,34]	0.0020 (0.0029) [13]	0.038 (0.021) [8,13,21,25,34,56,60]	0.4 [66]	--
Sr	5.9E-4 (9.4E-4) [1,2,13,14,27]	0.0026 (0.0018) [1,8,14,36]	0.095 (0.044) [1,5,13,20,25,27,29,36, 39,43,44,45,46,47,51, 52,53]	1.73 (0.36) [5,8,13,25,31,34,53,56, 57,60,61]	1.24 (0.38) [48,68]	--
Y	0.0054 (0.0026) [2,14,23,27]	0.012 (0.003) [14,28]	0.42 (0.04) [27,42,44,47]	0.021 (0.004) [8,56,57]	20 [66]	0.01 ‡
Zr	0.0014 (0.0006) [14,27]	0.027 (0.014) [8,11,14,28,36]	0.14 (0.05) [11,27,34,36,39,40,41, 43,44,45,47,48,54]	0.0078 (0.0033) [11,48,56]	0.64 [47]	0.054 [49,69]
Nb	6.2E-4 (8.2E-4) [14,27]	0.0066 (0.0051) [14,36]	0.0061 (0.0023) [27,36,41,43,44,45,47]	0.015 (0.007) [8,48]	--	0.085 [69]
Cs	0.00043 [13]	--	0.0031 (0.0044) [13,55]	0.032 (0.010) [8,13,29]	0.7 [66]	--
Ba	5.9E-5 (6.3E-5) [1,2,13,14]	0.0020 (0.0028) [1,14]	0.0011 (0.0018) [1,13,39,44,45]	0.41 (0.21) [8,13,20,21,24,25,29, 32,34,56,57,60,61]	0.45 [66]	--
La	2.1E-5 (1.2E-5) [2,14]	5.4E-4 (1.9E-4) [14,38]	0.062 (0.028) [5,11,27,42,45,46,47,49]	0.097 (0.052) [5,8,11,20,24,31,56,57, 60,61,62]	15.3 (9.2) [24,47,65,66,68]	0.01 [72]
Ce	4.6E-5 (2.2E-5) [2,14]	9.3E-4 (1.8E-4) [14,38]	0.099 (0.036) [5,11,27,42,45,46,47, 49]	0.074 (0.033) [5,8,11,20,24,31,56,57, 60,61,62]	19.1 (10.2) [24,47,65,66,68]	0.01 [72]
Pr	1.2E-4 (8.4E-5) [2,14]	0.0019 (0.0008) [14,38]	0.16 (0.07) [5,11,27,42,45,46,47, 49]	0.062 (0.029) [5,8,11,20,24,31,56,57, 60,61,62]	21.6 (10.9) [24,47,65,66,68]	0.01 [72]
Nd	2.7E-4 (1.6E-4) [2,14,22]	0.0027 (0.0016) [14,38]	0.22 (0.11) [5,11,27,42,45,46,47, 49]	0.049 (0.025) [5,8,11,20,24,31,56,57, 60,61,62]	24.1 (11.8) [24,47,65,66,68]	0.01 [72]
Sm	6.6E-4 (1.8E-4) [2,14,22]	0.0072 (0.0058) [14,38]	0.35 (0.13) [5,11,27,42,45,46,47, 49]	0.037 (0.020) [5,8,11,20,24,31,56,57, 60,61,62]	28.1 (15.2) [24,47,65,66,68]	0.01 [72]
Eu	7.5E-4 (3.9E-4) [14,22]	0.0037 (0.0007) [14,38]	0.06 [50]	1.1 (0.1) [31,60]	16.4 §	0.01 [72]
Gd	0.0014 (0.0039) [2,14,22]	0.018 (0.018) [14,38]	0.41 (0.12) [5,11,27,42,45,46,47, 49]	0.033 (0.015) [5,8,11,20,24,31,56,57, 60,61,62]	27.4 (14.2) [24,47,65,66,68]	0.01 [72]

Tb	**0.0035** (0.0018) [2,14,22]	**0.023** (0.023) [14,38]	**0.43** (0.12) [5,11,27,42,45,46,47,49]	**0.031** (0.015) [5,8,11,20,24,31,56,57,60,61,62]	**25.6** (12.8) [24,47,65,66,68]	**0.01** [72]
Dy	**0.0060** (0.0033) [2,14,22]	**0.030** (0.027) [14,38]	**0.45** (0.11) [5,11,27,42,45,46,47,49]	**0.026** (0.013) [5,8,11,20,24,31,56,57,60,61,62]	**21.5** (10.3) [24,47,65,66,68]	**0.01** [72]
Ho	**0.0094** (0.0037) [2,14,22]	**0.042** (0.039) [14,38]	**0.45** (0.12) [5,11,27,42,45,46,47,49]	**0.024** (0.012) [5,8,11,20,24,31,56,57,60,61,62]	**18.6** (8.2) [24,47,65,66,68]	**0.01** [72]
Er	**0.014** (0.004) [2,14,22]	**0.055** (0.049) [14,38]	**0.45** (0.12) [5,11,27,42,45,46,47,49]	**0.021** (0.012) [5,8,11,20,24,31,56,57,60,61,62]	**15.5** (6.2) [24,47,65,66,68]	**0.01** [72]
Tm	**0.018** (0.003) [2,14,22]	**0.061** (0.050) [14,38]	**0.45** (0.11) [5,11,27,42,45,46,47,49]	**0.020** (0.012) [5,8,11,20,24,31,56,57,60,61,62]	**12.8** (5.0) [24,47,65,66,68]	**0.01** [72]
Yb	**0.023** (0.003) [2,14,22]	**0.070** (0.046) [14,38]	**0.44** (0.11) [5,11,27,42,45,46,47,49]	**0.018** (0.012) [5,8,11,20,24,31,56,57,60,61,62]	**10.2** (3.9) [24,47,65,66,68]	**0.01** [72]
Lu	**0.027** (0.004) [2,14,22]	**0.078** (0.037) [14,38]	**0.43** (0.11) [5,11,27,42,45,46,47,49]	**0.016** (0.012) [5,8,11,20,24,31,56,57,60,61,62]	**8.7** (4.0) [24,47,65,66,68]	**0.01** [72]
Hf	**0.0069** (0.0053) [11,14]	**0.033** (0.026) [11,14]	**0.26** (0.07) [5,7,11,27,28,44,45,46,47,55]	**0.014** (0.005) [5,11,61]	**0.40** (0.33) [47,65,66]	**0.065** [69]
Th	**5.7E-5** (6.7E-5) [1,14]	**7.4E-4** (1.0E-3) [1,14]	**9.4E-4** [1]	**0.015** (0.008) [5,61]	**1.62** (0.35) [63,64,65,66,67]	--
U	**1.5E-5** (6.4E-6) [1,14]	**4.5E-4** (5.8E-4) [1,14]	**5.3E-4** (2.3E-4) [1,55]	**0.01** [5]	**0.96** (0.75) [63,64,65]	--

[1] Beattie (1993). [2] Beattie (1994). [3] Bougault and Hekinian (1974). [4] Colson et al. (1988). [5] Dostal et al. (1983). [6] Duke (1976). [7] Dunn (1987). [8] Dunn and Sen (1994). [10] Ehlers et al. (1992). [11] Fujimaki et al. (1984). [12] Gaetani and Grove (1997). [13] Hart and Brooks (1974). [14] Kennedy et al. (1993). [15] Klock and Palme (1988). [16] Kohn and Schofield (1994). [17] Leeman and Scheidegger (1977). [18] Libourel (1999). [19] Lindstrom (1983). [20] Matsui et al. (1977). [21] McKay and Weill (1976). [22] McKay (1986). [23] Nielsen et al. (1992). [24] Paster et al. (1974). [25] Philpotts and Schnetzler (1970). [26] Schreiber (1979). [27] Skulski et al. (1994). [28] Ulmer (1989). [29] Villemant et al. (1981). [30] Watson (1977). [31] Weill and McKay (1975). [32] Bacon and Druitt (1988). [33] Barnes

(1986). [34] Ewart and Griffin (1994) [35] Irving and Frey (1984). [36] Keleman and Dunn (1992). [37] Mysen (1978). [38] Schwandt and McKay (1998). [39] Chazot et al. (1996). [40] Dunn and McCallum (1982). [41] Forsythe et al. (1994). [42] Gallahan and Nielsen (1992). [43] Green et al. (1989). [44} Hart and Dunn (1993). [45] Hauri et al. (1994). [46] Irving and Frey (1984). [47] Johnson (1994). [48] McCallum and Charette (1978). [49] McKay et al. (1986). [50] McCanta et al. (2004). Assumes $D_{Eu}/D_{Gd} = 0.156$ at IW-1 and average D_{Gd} value. [51] McKay et al. (1991). [52] Ray et al. (1983). [53] Sun et al. (1974). [54] Watson and Ryerson (1986). [55] Watson et al. (1987). [56] Bindeman et al. (1998). [57] Drake and Weill (1975). [58] Lindstrom (1976). [59] Malvin and Drake (1987). [60] McKay and Weill (1977). [61] Phinney and Morrison (1990). [62] Schnetzler and Philpotts (1970).[63] Benjamin et al. (1978). [64] Fujimaki (1986). [65] Luhr et al. (1984). [66] Mahood and Stimac (1990). [67] Seitz (1973). [68] Watson and Green (1981). [69] Horn et al. (1994). [70] Ruzicka et al. (2006). [71] Ringwood (1970). [72] Nagasawa et al. (1980).
§ Calculated based on Eu* = 0.59, (Paster et al., 1974; Fujimaki, 1986).
‡ Assumed same as REE.

REFERENCES FOR TABLE EA-1

Bacon, C.R. and Druitt, T.H. (1988) Compositional evolution of the zoned calcalkaline magma chamber of Mount Mazama, Crater Lake, Oregon. *Contrib. Mineral. Petrol.* **98**, 224-256.

Barnes, S.J. (1986) The distribution of chromium among orthopyroxene, spinel and silicate liquid at atmospheric pressure. *Geochim. Cosmochim. Acta* **50**, 1889-1909.

Beattie, P. (1993) The effect of partial melting of spinel peridotite on uranium series disequilibria: constraints from partitioning studies. *Earth Planet Sci. Lett.* **177**, 379-391.

Beattie P. (1994) Systematics and energetics of trace-element partitioning between olivine and silicate melts: implications for the nature of mineral/melt partitioning. *Chem. Geol.* **117**, 57-71.

Benjamin T., Heuser, W.R. and Burnett, D.S. (1978) Laboratory studies of actinide partitioning relevant to [244]Pu chronometry. *Proc. Lunar. Planet. Sci. Conf. 9th*, 1393-1406.

Bindeman, I.N., Davis, A.M. and Drake, M.J. (1998) Ion microprobe study of plagioclase-basalt partition experiments at natural concentration levels of trace elements. *Geochim. Cosmochim. Acta* **62**, 1175-1193.

Bougault, H. and Hekinian, R. (1974) Rift valley in the Atlantic Ocean near 36 degrees 50'N; petrology and geochemistry of basalt rocks. *Earth Planet. Sci. Lett.* **24**, 249-261.

Chazot, G., Menzies, M.A. and Harte, B. (1996) Determination of partition coefficients between apatite, clinopyroxene, amphibole, and melt in natural spinel lherzolites from Yemen: Implications for wet melting of the lithospheric mantle. *Geochim. Cosmochim. Acta* **60**, 423-437.

Colson R.O., McKay G.A. and Taylor L. A. (1988) Temperature and composition dependencies of trace element partitioning: olivine/melt and low-Ca pyroxene/melt. *Geochim. Cosmochim. Acta* **52**, 539-553.

Dostal, J., Dupuy, C., Carron, J.P., Dekerneizon, M.L. and Maury, R.C. (1983) Partition-coefficients of trace elements:Application to volcanic rocks of St.Vincent, West-Indies. *Geochim. Cosmochim. Acta* **47**, 525-533.

Drake, M.J. and Weill, D.F. (1975) Partition of Sr, Ba, Ca, Y, Eu^{2+}, Eu^{3+}, and other REE between plagioclase feldspar and magmatic liquid: An experimental study. *Geochim. Cosmochim. Acta* **39**, 689-712.

Duke, J.M. (1976) Distribution of the period four transition elements among olivine, calcic clinopyroxene and mafic silicate liquid; experimental results. *J. Petrol.* **17**, 499-521.

Dunn, T. (1987) Partitioning of Hf, Lu, Ti, and Mn between olivine, clinopyroxene and basaltic liquid. *Contrib. Mineral. Petrol.* **96**, 476-484.

Dunn, T. and Mccallum, I.S. (1982) The partitioning of Zr and Nb between diopside and melts in the system diopside-albite-anorthite. *Geochim. Cosmochim. Acta* **46**, 623-629.

Dunn T. and Sen C. (1994) Mineral/matrix partition coefficients for orthopyroxene, plagioclase, and olivine in basaltic to andesitic systems: A combined analytical and experimental study. *Geochim. Cosmochim. Acta* **58**, 717-733

Ehlers K., Grove T. L., Sisson T.W., Recca S. I. and Zervas D. A. (1992) The effect of oxygen fugacity on the partitioning of nickel and cobalt between olivine, silicate melt, and metal. *Geochim. Cosmochim. Acta* **56**, 3733-3743.

Ewart, A. and Griffin, W.L. (1994) Application of proton microprobe data to trace-element partitioning in volcanic rocks. *Chem. Geol.* **117**, 251-284.

Forsythe, L.M., Nielsen, R.L. and Fisk, M.R. (1994) High-field-strength element partitioning between pyroxene and basaltic to dacitic magmas. *Chem. Geol.* **117**, 107-125.

Fujimaki, H. (1986) Partition coefficients of Hf, Zr, and REE between zircon, apatite, and liquid. *Contrib. Mineral. Petrol.* **94**, 42-45.

Fujimaki, H., Tatsumoto, M. and Aoki, K.-i. (1984) Partition coefficients of Hf, Zr, and REE between phenocrysts and groundmasses. *J. Geophys. Res.* **89**, 662-672.

Gaetani G.A. and Grove T.L. (1997) Partitioning of moderately siderophile elements among olivine, silicate melt, and sulfide melt: Constraints on core formation in the earth and Mars. *Geochim. Cosmochim. Acta* **61**, 1829-1846.

Gallahan, W.E. and Nielsen, R.L. (1992) The partitioning of Sc, Y, and the rare-earth elements between high-Ca pyroxene and natural mafic to intermediate lavas at 1-atmosphere. *Geochim. Cosmochim. Acta* **56**, 2387-2404.

Green, T.H., Sie, S.H., Ryan, C.G. and Cousens, D.R. (1989) Proton microprobe-determined partitioning of Nb, Ta, Zr, Sr and Y between garnet, clinopyroxene and basaltic magma at high pressure and temperature. *Chem. Geol.* **74**, 201-216.

Hart, S.R. and Brooks, C. (1974) Clinopyroxene-matrix partitioning of K, Rb, Cs, Sr and Ba. *Geochim. Cosmochim. Acta* **38**, 1799-1806.

Hart, S.R. and Dunn, T. (1993) Experimental cpx/melt partitioning of 24 trace elements. *Contrib. Mineral. Petrol.* **113**, 1-8.

Hauri, E.H., Wagner, T.P. and Grove, T.L. (1994) Experimental and natural partitioning of Th, U, Pb and other trace elements between garnet, clinopyroxene and basaltic melts. *Chem. Geol* **117**, 149-166.

Horn, I., Foley, S.F., Jackson, S.E. and Jenner, G.A. (1994) Experimentally determined partitioning of high field strength- and selected transition elements between spinel and basaltic melt. *Chem. Geol.* **117**, 193-218.

Irving, A.J. and Frey, F.A. (1984) Trace-element abundances in megacrysts and their host basalts: Constraints on partition-coefficients and megacryst genesis. *Geochim. Cosmochim. Acta* **48**, 1201-1221.

Johnson, K.T.M. (1994) Experimental cpx/ and garnet/melt partitioning of REE and other trace elements at high pressures; petrogenetic implications. *Mineral. Mag.* **58**, 454-455

Keleman, P.B. and Dunn, J.T. (1992) Depletion of Nb relative to other highly incompatible elements by melt/rock reaction in the upper mantle. *EOS, Trans. Amer. Geophys. Union* **73**, 656-657.

Kennedy A.K., Lofgren G.E. and Wasserburg.,G.J. (1993) An experimental study of trace element partitioning between olivine, orthopyroxene and melt in chondrules: equilibrium values and kinetic effects. *Earth Planet. Sci. Lett.* **115**, 177-195.

Klöck, W. and Palme, H. (1988) Partitioning of siderophile and chalcophile elements between sulfide, olivine, and glass in a naturally reduced basalt from Disko Island, Greenland. *Proc. Lunar Planet. Sci. Conf. 18th*, 471-483.

Kohn, S.C. and Schofield, P.F. (1994) The Importance of Melt Composition in Controlling Trace-Element Behavior - an Experimental-Study of Mn and Zn Partitioning between Forsterite and Silicate Melts. *Chem. Geol.* **117**, 73-87.

Leeman W.P. and Scheidegger K.F. (1977) Olivine/liquid distribution coefficients and a test for crystal-liquid equilibrium. *Earth Planet. Sci. Lett.* **35**, 247-257.

Libourel G. (1999) Systematics of calcium partitioning between olivine and silicate melt: Implications for melt structure and calcium content of magmatic olivines. *Contrib. Mineral. Petrol.* **136**, 63-80.

Lindstrom, D.J. (1976) Experimental study of the partitioning of the transition metals between clinopyroxene and coexisting silicate liquids. *Dept. of Geochemistry, Grad. Sch. Univ. of Oregon, Eugene, OR, USA.*

Lindstrom, D.J. (1983) Kinetic effects on trace element partitioning. *Geochim. Cosmochim. Acta* **47**, 617-622.

Luhr, J.F., Carmichael, I.S.E. and Varekamp, J.C. (1984) The 1982 eruptions of El Chichon volcano, Chiapas, Mexico: mineralogy and petrology of the anhydrite-bearing pumices. *J. Volcan. Geothermal Res*. **23**, 69-108.

Malvin, D.J. and Drake, M.J. (1987) Experimental determination of crystal/melt partitioning of Ga and Ge in the system forsterite-anorthite-diopside. *Geochim. Cosmochim. Acta* **51**, 2117-2128.

Mahood, G.A. and Stimac, J.A. (1990) Trace-element partitioning in pantellerites and trachytes. *Geochim. Cosmochim. Acta* **54**, 2257-2276.

Matsui, Y., Onuma, N., Nagasawa, H., Higuchi, H. and Banno, S. (1977) Crystal structure control in trace element partition between crystal and magma. *Tectonics* **100**, 315-324.

McCallum, I.S. and Charette, M.P. (1978) Zr and Nb partition coefficients: implications for the genesis of mare basalts, KREEP, and sea floor basalts. *Geochim. Cosmochim. Acta* **42**, 859-869.

McCanta, M.C., Rtherford, M.J. and Jones, J.H. (2004) An experimental study of rare earth element partitioning between a shergottite melt and pigeonite: Implications for the oxygen fugacity of the martian interior. *Geochim. Cosmochim. Acta* **68**, 1943-1952.

McKay, G.A. (1986) Crystal/liquid partitioning of REE in basaltic systems: Extreme fractionation of REE in olivine. *Geochim. Cosmochim. Acta* **50**, 69-79.

McKay, G.A. and Weill, D.F. (1976) Petrogenesis of KREEP. *Proc. Lunar Sci. Conf. 7th*, 2427-2447.

McKay, G.A. and Weill, D.F. (1977) KREEP petrogenesis revisited. *Proc. Lunar Sci. Conf. 8th*, 2339-2355.

McKay G., Wagstaff, J. and Yang, S.-R. (1986) Clinopyroxene REE distribution coefficients for shergottites: The REE content of the Shergotty melt. *Geochim. Cosmochim. Acta* **50**, 927-937.

McKay, G., Le, L. and Wagstaff, J. (1991) Constraints on the origin of the mare basalt europium anomaly: REE partition coefficients for pigeonite. *Lunar Planet Sci. Conf. 12*[th], 883-884.

Mysen, B. (1978) Experimental determination of nickel partition coefficients between liquid, pargasite and garnet peridotite minerals and concentration limits of behavior according to Henry's Law at high pressure and temperature. *Am. J. Sci.* **278**, 217-243.

Nagasawa, H., Schreiber, H.D. and Morris, R.V. (1980) Experimental mineral/liquid partition coefficients of the rare Earth elements, Sc and Sr for perovskite, spinel and melilite. *Earth Planet. Sci. Lett.* **46**, 431-437.

Nielsen, R.L., Gallahan, W.E. and Newberger, F. (1992) Experimentally determined mineral-melt partition coefficients for Sc, Y and REE for olivine, orthopyroxene, pigeonite, magnetite and ilmenite. *Contrib. Mineral. Petrol.* **110**, 488-499.

Paster, T.P., Schauwecker, D.S. and Haskin, L.A. (1974) The behavior of some trace elements during solidification of the Skaergaard layered series. *Geochim. Cosmochim. Acta* **38**, 1,549-1,577.

Philpotts C.C. and Schnetzler J.A. (1970) Phenocryst-matrix partition coefficients for K, Rb, Sr and Ba, with applications to anorthosite and basalt genesis. *Geochim. Cosmochim. Acta* **34**, 307-322.

Phinney, W.C. andMorrison, D.A. (1990) Partition coefficients for calcic plagioclase: Implications for Archaen anorthosites. *Geochim. Cosmochim. Acta* **54**, 1639-1654.

Ray, G.L., Shimizu, N. and Hart, S.R. (1983) An Ion Microprobe Study of the Partitioning of Trace-Elements between Clinopyroxene and Liquid in the System Diopside-Albite-Anorthite. *Geochim. Cosmochim. Acta* **47**, 2131-2140.

Ringwood, A.E. (1970) Petrogenesis of Apollo 11 basalts and implications for lunar origin. *J. Geophys. Res.* **75**, 6,453-6,479.

Ruzicka A., Hutson M. and Floss C. (2006) Petrology of silicate inclusions in the Sombrerete ungrouped iron meteorite: Implications for the origins of IIE-type silicate-bearing irons. *Meteorit. Planet. Sci.* **41**, 1797-1831.

Schnetzler, C.C. and Philpotts, J.A. (1970) Partition coefficients of rare-earth elements between igneous matrix material and rock-forming mineral phenocrysts; II. *Geochim. Cosmochim. Acta* **34**, 331-340.

Schreiber, H.D. (1976) The experimental determination of redox states, properties, and distribution of chromium in synthetic silicate phases and application to basalt petrogenesis. *University of Wisconsin, Madison.*

Schwandt, C.S. and McKay, G.A. (1998) Rare earth element partition coefficients from enstatite/melt synthesis experiments. *Geochim. Cosmochim. Acta* **62**, 2845-2848.

Seitz, M.G. (1973) Uranium and thorium partitioning in diopside-melt and whitlockite-melt systems. *Yearbook of the Carnegie Institute of Washington 72: 581-586.*

Skulski, T., Minarik, W. and Watson, E.B. (1994) High pressure experimental trace-element partitioning between clinopyroxene and basaltic melts. *Chem. Geol.* **117**, 127-147.

Sun, C.-O., Williams, R.J. and Sun, S.-S. (1974) Distribution coefficients of Eu and Sr for plagioclase-liquid and clinopyroxene-liquid equilibria in oceanic ridge basalt; an experimental study. *Geochim. Cosmochim. Acta* **38**, 1415-1433.

Ulmer, P. (1989) Partitioning of high field strength elements among olivine, pyroxenes, garnet and calc alkaline picrobasalt: experimental results and an application. *Internat. J. Mass Spectrom. Ion Phys.* 42-47.

Villemant B., Jaffrezic H., Joron J.-L. and Treuil M. (1981) Distribution coefficients of major and trace elements; fractional crystallization in the alkali basalt series of Chaîne des Puys (Massif Central, France). *Geochim. Cosmochim. Acta* **45**, 1997-2016.

Watson, E.B. (1977) Partitioning of manganese between forsterite and silicate liquid. *Geochim. Cosmochim. Acta* **41**, 1363-1374.

Watson, E.B. and Green, T.H. (1981) Apatite/liquid partition coefficients for the rare earth elements and strontium. *Earth Planet. Sci. Lett.* **56**, 405-421.

Watson, E.B. and Ryerson, F.J. (1986) Partitioning of zirconium between clinopyroxene and magmatic liquids of intermediate composition. *Geochim. Cosmochim. Acta* **50**, 2523-2526.

Watson, E.B., Othman, D.B., Luck, J.M. and Hofmann, A.W. (1987) Partitioning of U, Pb, Cs, Yb, Hf, Re and Os between chromian diopsidic pyroxene and haplobasaltic liquid. *Chem. Geol.* **62**, 191-208.

Weill, D.F. and McKay, G.A. (1975) The partitioning of Mg, Fe, Sr, Ce, Sm, Eu, and Yb in lunar igneous systems and a possible origin of KREEP by equilibrium partial melting. *Proc. Lunar Sci. Conf. 6th,* 1143-1158.

Electronic Annex, Section 3: Major and minor-element mineral chemistry.

Major- and minor-element compositions for pyroxene, feldspar and olivine determined by EMPA are illustrated in Figs. EA-1 and EA-2. Fig. EA-1 presents ternary and quadrilateral diagrams for phases analyzed in Udei Station and Miles, whereas Fig. EA-2 presents traverse data for Miles. The traverse in Fig. EA-2a was obtained in an orthopyroxene grain cluster at the edge of Miles-10 (Fig. 3j), and shows Wo, Fs, Na, Al, Ti, Cr and possibly Mn contents all decreasing towards the metal host. The variations are not completely smooth but rather stepped or discontinuous, as is especially evident for Ti and Al, possibly reflecting different orthopyroxene grains in the cluster. Similar zoning was observed in opx close to the metal host elsewhere in Miles. The clinopyroxene grain shown in Fig. EA-2b was obtained in a clinopyroxene grain in Miles-6 (Fig. 3g) and is unusual in showing a systematic core-rim zoning pattern, with the core depleted in Cr, Na, and Ti, and enriched in Al. No similar core-rim zoning was identified in EMPA traverses of other clinopyroxene grains, which all represent pyroxene glomerocrysts consisting of various proportions of clinopyroxene and orthopyroxene. The lack of Fs and Wo zoning in this clinopyroxene grain is typical.
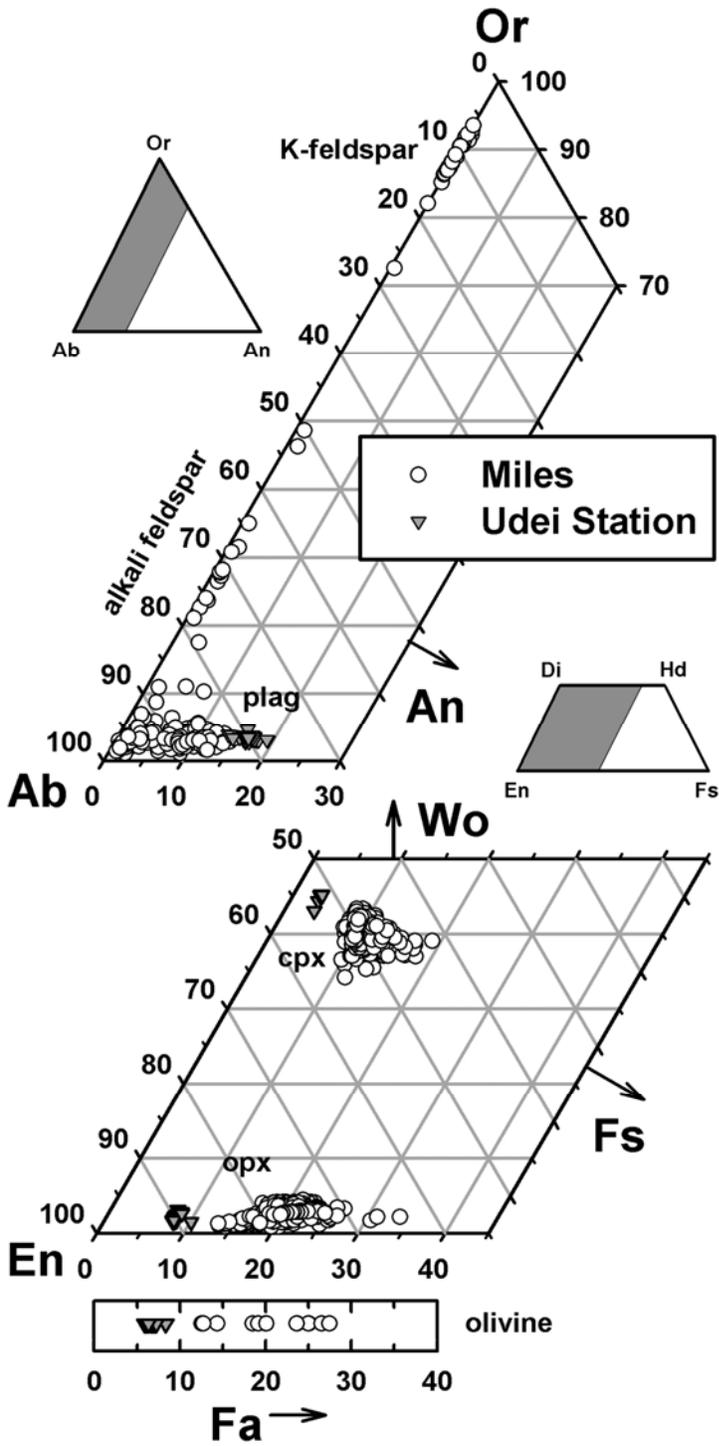
Fig. EA-1 Feldspar, pyroxene, and olivine compositions for Miles and Udei Station determined by EMPA shown on ternary and quadrilateral diagrams.
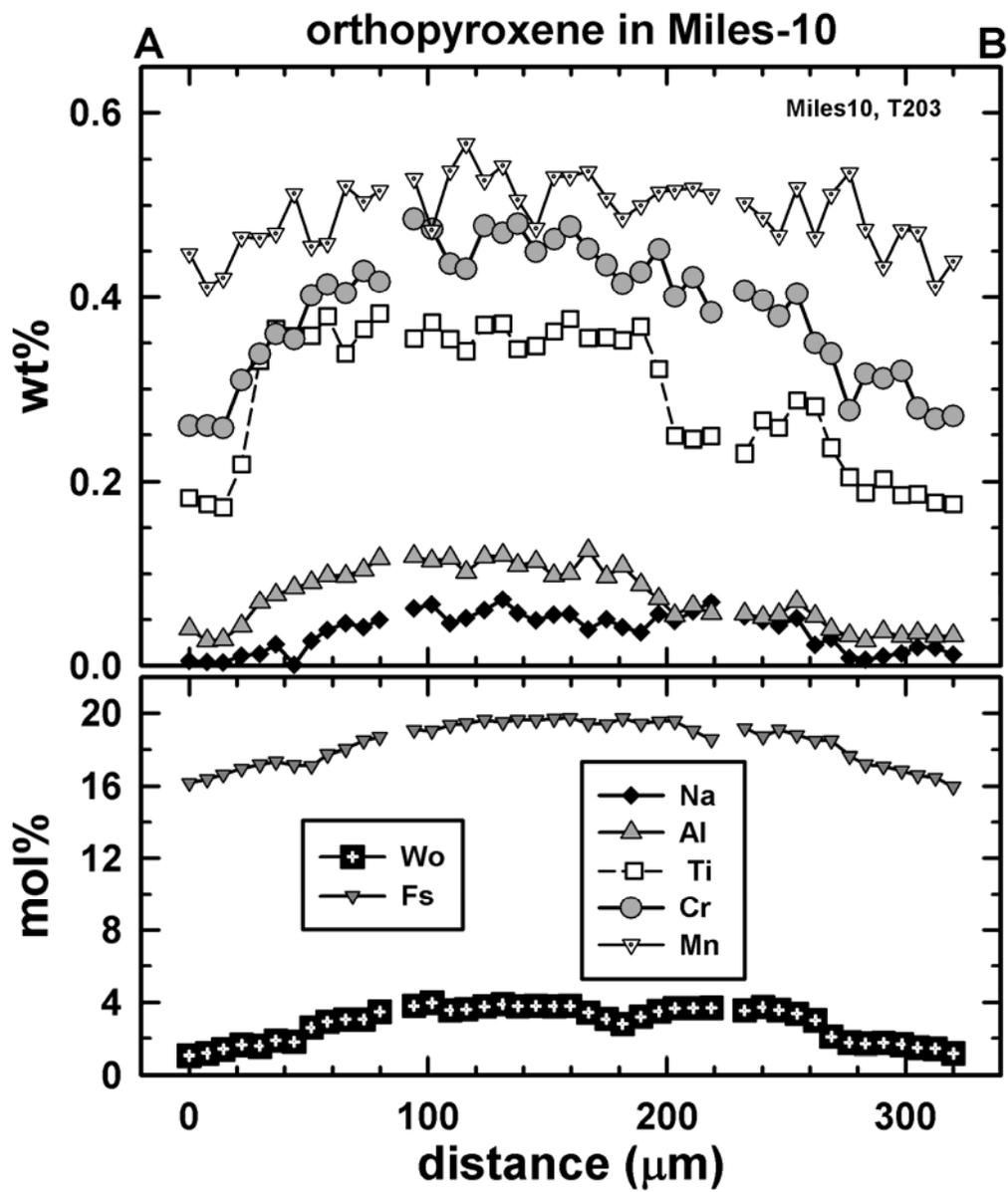
Fig. EA-2a Microprobe traverse data for orthopyroxene in Miles-10. The traverse location is shown in Fig. 3j.
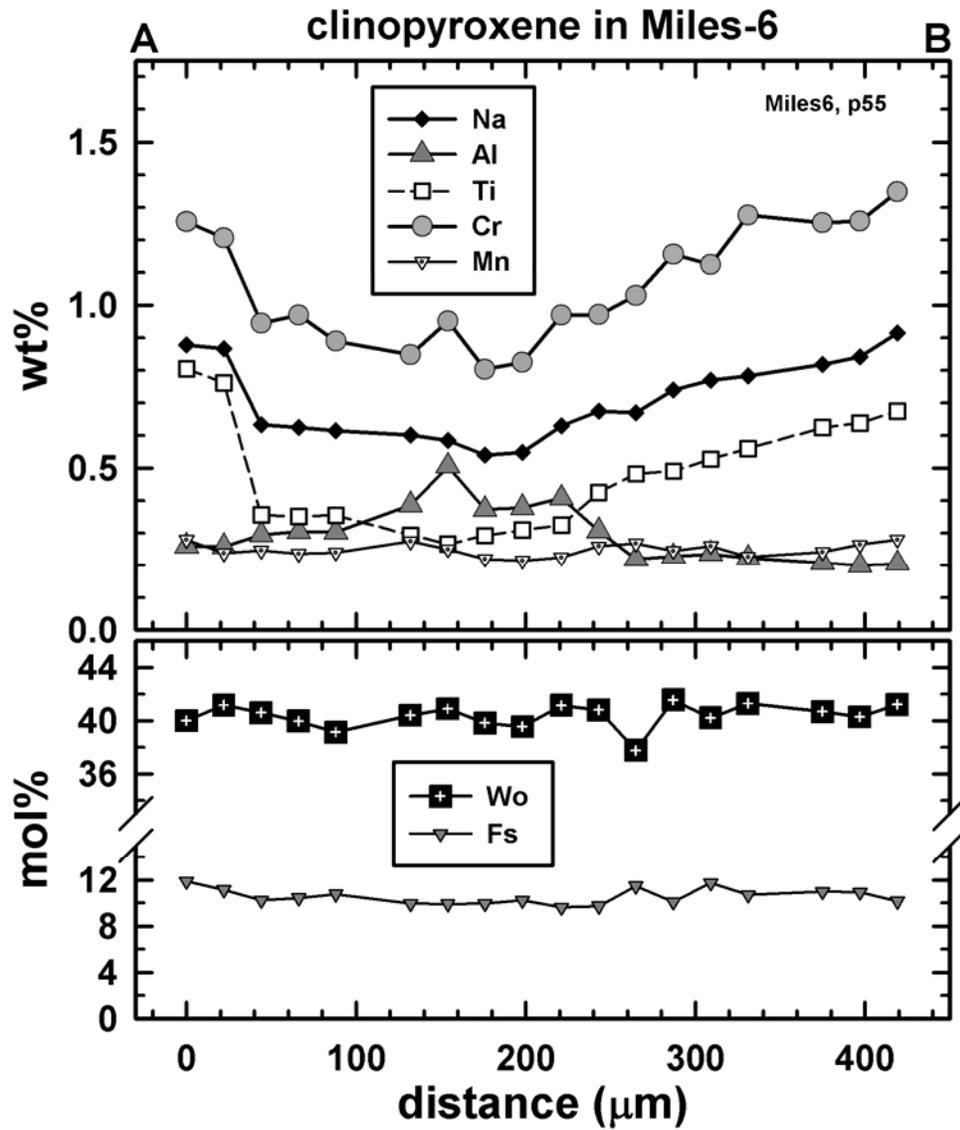
Fig. EA-2b. Microprobe traverse for clinopyroxene in Miles-6. The traverse location is shown in Fig. 3g.

Electronic Annex, Section 4: Bulk compositions of inclusions in Udei Station and Miles.

Table EA-2a. Bulk composition of Udei Station inclusions (silicate fraction), calculated by combining modal, EMPA, and LA-ICP-MS data

	Udei-1A-1	Udei-1A-3	Udei-1B	Udei-3B Poikilitic #1	Udei-3B Poikilitic #2	Udei-3B Granular #1 (finer)	Udei-3B Granular #2 (coarser)
EMPA Wt%							
SiO_2	53.98	60.27	60.56	61.67	59.97	51.52	51.79
TiO_2	0.18	0.17	0.32	0.14	0.17	0.14	0.14
Al_2O_3	3.60	9.87	13.36	12.70	8.85	0.73	0.22
Cr_2O_3	0.27	0.21	0.53	0.17	0.23	0.21	0.23
FeO	4.71	3.11	0.90	2.45	3.38	5.75	5.86
MnO	0.35	0.25	0.12	0.20	0.27	0.42	0.43
MgO	32.88	19.64	7.58	15.07	21.33	40.25	40.64
CaO	2.55	2.42	10.94	2.38	2.16	0.73	0.65
Na_2O	1.39	3.82	5.36	4.91	3.40	0.25	0.04
K_2O	0.08	0.25	0.33	0.32	0.22	0.01	0.00
	100	100	100	100	100	100	100
LA-ICP-MS CI-normalized*							
Al	2.23 (0.05)	6.09 (0.14)	8.26 (0.18)	7.83 (0.17)	5.46 (0.12)	0.45 (0.02)	0.15 (0.01)
Si	2.38 (0)	2.66 (0)	2.66 (0)	2.72 (0)	2.65 (0)	2.28 (0)	2.29 (0)
Ca	1.99 (0.14)	1.95 (0.16)	8.35 (0.40)	1.94 (0.17)	1.75 (0.09)	0.60 (0.07)	0.55 (0.07)
Sc	2.05 (0.19)	1.41 (0.14)	5.30 (0.45)	1.04 (0.12)	1.41 (0.05)	1.39 (0.14)	1.44 (0.14)
Ti	2.12 (0.13)	2.02 (0.11)	3.94 (0.28)	1.74 (0.10)	2.08 (0.03)	1.68 (0.10)	1.80 (0.10)
V	1.01 (0.12)	0.69 (0.07)	2.60 (0.39)	0.50 (0.05)	0.70 (0.02)	0.69 (0.06)	0.72 (0.07)
Cr	0.65 (0.03)	0.53 (0.03)	1.22 (0.05)	0.41 (0.02)	0.56 (0.00)	0.52 (0.03)	0.56 (0.03)
Mn	1.32 (0.03)	0.94 (0.02)	0.44 (0.03)	0.75 (0.01)	1.03 (0.00)	1.56 (0.04)	1.60 (0.04)
Co	5E-3 (1E-3)	5E-3 (2E-3)	3E-3 (2E-3)	5E-3 (2E-3)	5E-3 (1E-3)	6E-3 (1E-3)	6E-3 (1E-3)
Ga	0.21 (0.02)	0.50 (0.03)	0.66 (0.06)	0.62 (0.04)	0.45 (0.03)	0.07 (0.01)	0.05 (0.01)
Rb	0.61 (0.08)	1.67 (0.18)	2.23 (0.27)	2.14 (0.23)	1.50 (0.15)	0.13 (0.03)	0.04 (0.03)
Sr	2.24 (0.09)	6.21 (0.24)	8.65 (0.33)	8.02 (0.31)	5.55 (0.21)	0.37 (0.02)	0.04 (0.01)
Y	1.39 (0.10)	0.60 (0.07)	6.71 (0.35)	0.28 (0.05)	0.50 (0.03)	0.32 (0.05)	0.31 (0.05)
Zr	0.86 (0.34)	0.51 (0.17)	3.20 (1.55)	0.34 (0.09)	0.49 (0.06)	0.38 (0.10)	0.39 (0.10)
Nb	0.10 (0.05)	0.10 (0.06)	0.29 (0.13)	0.09 (0.06)	0.09 (0.04)	0.06 (0.03)	0.05 (0.03)
Ba	2.20 (0.12)	6.25 (0.32)	8.37 (0.43)	8.08 (0.41)	5.59 (0.28)	0.37 (0.03)	0.04 (0.01)
La	1.30	2.08	6.05 (1.33)	2.48	1.82 (0.57)	0.17	0.05
Ce	1.23	1.12	6.54 (0.77)	1.14	0.93 (0.27)	0.10	0.02
Pr	1.36 (0.18)	0.77 (0.24)	7.41 (0.76)	0.59 (0.27)	0.61 (0.19)	0.12 (0.05)	0.06 (0.04)
Nd	1.53 (0.17)	0.70 (0.17)	8.40 (0.71)	0.43 (0.17)	0.53 (0.12)	0.13 (0.05)	0.07 (0.05)
Sm	1.89 (0.38)	0.92 (0.31)	9.40 (1.44)	0.60 (0.29)	0.75 (0.18)	0.37 (0.15)	0.31 (0.15)
Eu	2.56 (0.43)	6.77 (1.05)	9.62 (1.55)	8.67 (1.34)	6.06 (0.91)	0.52 (0.12)	0.18 (0.06)
Gd	1.70 (0.20)	0.84 (0.25)	8.63 (0.51)	0.55 (0.27)	0.68 (0.16)	0.29 (0.13)	0.24 (0.12)
Tb	1.58 (0.21)	0.64 (0.15)	8.23 (0.80)	0.29 (0.11)	0.50 (0.06)	0.24 (0.09)	0.20 (0.09)
Dy	1.62 (0.22)	0.69 (0.15)	8.06 (0.81)	0.35 (0.12)	0.56 (0.07)	0.32 (0.10)	0.29 (0.10)

Ho	1.54 *(0.24)*	0.74 *(0.17)*	7.09 *(0.71)*	0.41 *(0.14)*	0.64 *(0.06)*	0.43 *(0.15)*	0.41 *(0.15)*
Er	1.43 *(0.20)*	0.74 *(0.14)*	6.24 *(0.74)*	0.45 *(0.11)*	0.66 *(0.06)*	0.46 *(0.09)*	0.45 *(0.09)*
Tm	1.58 *(0.32)*	1.03 *(0.30)*	5.77 *(0.76)*	0.75 *(0.26)*	0.97 *(0.09)*	0.72 *(0.22)*	0.73 *(0.24)*
Yb	1.62 *(0.28)*	1.08 *(0.25)*	5.33 *(0.58)*	0.78 *(0.21)*	1.04 *(0.07)*	0.85 *(0.22)*	0.89 *(0.22)*
Lu	1.79 *(0.49)*	1.30 *(0.45)*	5.45 *(1.07)*	1.02 *(0.40)*	1.27 *(0.16)*	1.04 *(0.37)*	1.07 *(0.38)*

* Normalized to mean CI-chondrite concentrations (Anders and Grevesse, 1989). Errors are shown in parentheses and reflect standard deviations of mean phase compositions.

Table EA-2b. Bulk composition of selected Miles inclusions (metal- and sulfide-free basis), calculated by combining modal, EMPA, and LA-ICP-MS data

	Miles-2	Miles-2A	Miles-3	Miles-5	Miles-6	Miles-8B	Miles-9 §	Miles-10	Miles 1-9 composite ‡
EMPA Wt%									
SiO_2	54.21	54.98	55.39	41.76	59.03	56.63	71.91	56.18	57.66
TiO_2	0.31	0.31	0.48	0.42	0.27	0.43	0.04	0.34	0.34
Al_2O_3	0.46	0.95	3.06	0.55	7.29	7.05	15.65	6.46	6.34
Cr_2O_3	0.39	0.39	0.95	0.83	0.40	0.92	0.00	0.69	0.68
FeO	13.89	13.55	8.28	7.58	9.76	4.97	0.70	8.17	7.59
MnO	0.60	0.59	0.38	0.34	0.32	0.25	0.00	0.34	0.30
MgO	27.46	27.29	18.06	16.18	14.88	11.90	0.02	15.65	14.46
CaO	1.94	1.42	11.14	20.93	3.63	12.65	0.22	7.78	8.44
Na_2O	0.22	0.48	1.82	0.57	3.75	4.01	4.89	3.19	3.36
K_2O	0.04	0.03	0.18	0.01	0.67	0.15	6.58	0.22	0.46
P_2O_5	0.43	0.00	0.27	9.59	0.00	1.00	0.00	0.87	0.35
Cl	0.05	0.00	0.00	1.23	0.00	0.05	0.00	0.12	0.03
	100	100	100	100	100	100	100	100	100
LA-ICP-MS CI-normalized*									
Ca	1.59	1.11	8.08	15.9	3.13	9.00	0.25	5.65	6.41
		(0.00)	(0.0)	(0.04)	(0.31)	(0.03)	(0.48)	(0.29)
Sc	1.95	1.94	6.58	5.47	3.07	6.30	0.30	3.43	4.74
		(0.13)	(0.10)	(0.35)	(0.22)	(0.87)	(0.16)	(0.71)	(0.68)
Ti	--	3.38	8.52	3.47	3.20	5.44	1.22	3.50	4.63
		(1.34)	(0.32)	(0.94)	(1.69)	(3.29)	(0.07)	(0.77)	(1.85)
V	1.04	1.42	3.16	3.26	1.37	2.83	0.02	2.69	2.27
		(0.14)	(0.05)	(0.28)	(0.12)	(0.17)	(4E-3)	(0.31)	(0.30)
Cr	1.10	1.44	3.15	2.14	1.30	2.28	2E-3	6.30	1.93
		(0.24)	(0.04)		(0.18)	(0.28)	(3E-4)	(0.41)	(0.26)
Mn	1.53	1.14	1.00	1.32	0.75	0.79	5E-3	1.12	0.80
		(0.10)	(0.17)		(0.21)	(0.18)	(2E-3)	(0.24)	(0.21)
Co	--	0.24	0.31	0.65	0.27	0.25	0.30	0.13	0.26
		(0.12)	(0.16)	(0.08)	(0.20)	(0.14)	(0.29)	(0.09)	(0.24)
Zn	0.60	0.39	0.26	0.23	0.18	0.09	5E-3	0.69	0.17
		(0.10)	(0.06)	(0.03)	(0.04)	(0.01)	(2E-3)	(0.11)	(0.04)
Ga	0.15	0.22	0.58	0.16	0.80	0.23	3.62	0.83	0.74
		(0.06)	(0.13)	(0.04)	(0.27)	(0.07)	(1.35)	(0.30)	(0.34)
Rb	0.08	0.38	6.62	0.40	6.79	0.70	162	1.94	7.51
		(0.13)	(4.57)	(0.15)	(1.17)	(0.37)	(64)	(1.01)	(5.36)
Sr	0.25	0.25	0.91	6.13	1.78	1.89	5.86	4.83	2.06
	(0.01)	(0.06)	(0.14)	(0.33)	(0.31)	(0.20)	(1.84)	(1.30)	(0.83)
Y	1.25	1.51	11.6	26.6	3.96	10.1	0.01	3.95	6.65
	(0.01)	(0.36)	(0.36)	(1.9)	(1.04)	(1.5)	(4E-3)	(1.00)	(2.05)
Zr	--	0.39	3.44	1.29	0.80	1.39	0.53	0.85	1.42
		(0.29)	(0.36)	(0.55)	(0.43)	(0.75)	(0.33)	(0.56)	(0.83)
Nb	0.12	0.25	0.35	0.64	0.16	0.46	0.11	0.33	0.33
		(0.04)	(0.16)	(0.04)	(0.10)	(0.31)	(0.07)	(0.23)	(0.31)

Cs	0.12	0.75 (0.35)	0.66 (0.38)	0.93 (0.25)	1.37 (0.77)	1.11 (0.48)	12.8 (5.0)	0.64 (0.48)	1.89 (1.88)
Ba	--	0.31 (0.07)	0.62 (0.23)	0.55 (0.24)	2.55 (0.57)	1.21 (0.40)	9.45 (3.41)	5.42 (1.10)	2.28 (1.02)
La	0.48 (0.02)	0.26 (0.20)	8.08 (0.40)	81.2 (3.8)	1.46 (0.75)	12.8 (2.5)	0.24 (0.04)	4.95 (1.49)	5.46 (2.18)
Ce	0.42 (0.01)	0.35 (0.26)	12.8 (0.8)	76.8 (4.9)	2.27 (1.15)	13.9 (2.9)	0.13 (0.03)	5.28 (1.85)	6.88 (2.92)
Pr	0.33 (0.01)	0.39 (0.21)	15.4 (1.0)	68.5 (4.2)	3.03 (1.40)	14.4 (3.2)	0.24 (0.23)	5.24 (1.97)	7.85 (3.35)
Nd	0.43 (0.01)	0.42 (0.23)	16.8 (1.2)	59.6 (3.8)	3.67 (1.49)	14.1 (2.8)	0.05 (4E-3)	5.16 (1.93)	8.34 (3.49)
Sm	0.48 (0.01)	0.71 (0.20)	16.5	45.8 (3.6)	4.39 (1.51)	13.6 (2.4)	0.04 (9E-3)	5.42 (1.76)	8.75 (3.28)
Eu	0.28 (0.02)	0.32 (0.09)	1.89 (0.22)	7.15 (0.47)	2.14 (0.47)	3.01 (0.22)	5.86 (2.29)	5.34 (1.42)	2.63 (0.95)
Gd	--	0.96 (0.16)	15.3 (0.4)	42.5 (3.3)	4.63 (1.34)	13.5 (2.1)	0.21 (0.07)	5.19 (1.45)	8.81 (3.00)
Tb	0.61 (4E-3)	1.09 (0.31)	14.3 (0.6)	34.8 (2.9)	4.41 (1.28)	12.5 (1.9)	0.08	4.84 (1.26)	8.13 (2.68)
Dy	0.98 (4E-3)	1.32 (0.37)	14.7 (0.5)	32.9 (2.8)	4.74 (1.25)	12.8 (2.2)	0.02 (5E-4)	5.04 (1.27)	8.41 (2.68)
Ho	1.05 (0.01)	1.58 (0.41)	13.4 (0.3)	28.8 (2.5)	4.56 (1.28)	11.3 (2.1)	0.04 (1E-3)	4.56 (1.13)	7.64 (2.49)
Er	1.42 (0.01)	1.86 (0.52)	13.0 (0.5)	26.2 (2.4)	4.63 (1.18)	10.9 (2.1)	0.04	4.51 (1.13)	7.33 (2.32)
Tm	1.48 (0.01)	2.14 (0.73)	12.6 (0.2)	22.1 (2.0)	4.66 (1.15)	9.63 (1.76)	0.07 (2E-3)	4.30 (1.11)	6.89 (2.15)
Yb	1.98 (3E-3)	2.29 (0.55)	11.8 (0.3)	17.6 (1.6)	4.72 (1.18)	8.76 (1.67)	0.07 (4E-3)	4.16 (1.14)	6.54 (2.00)
Lu	2.71 (0.01)	2.82 (0.36)	11.7 (0.6)	15.5 (1.7)	4.69 (1.16)	8.46 (1.71)	0.15 (0.01)	4.20 (1.17)	6.32 (1.93)
Hf	--	0.40 (0.09)	5.39 (0.98)	0.38 (0.09)	1.07 (0.59)	3.12 (1.88)	0.72 (0.44)	1.01 (0.54)	2.32 (1.48)
Th	1.90 (0.17)	0.48 (0.38)	--	63.3 (17.1)	0.48 (0.30)	7.83 (1.46)	1.00 (0.18)	2.18 (0.96)	3.18 (1.53)
U	3.68 (0.24)	0.68	--	56.9 (3.1)	0.25 (0.08)	2.80 (0.42)	0.37 (0.13)	4.41 (1.17)	2.00 (0.52)

* Same as Table 7a. § Renormalized to exclude 16.41 wt% of "FeO(OH)" corresponding to iron hydroxide weathering product. ‡ Area-weighted average of Miles inclusions 1, 2, 2A, 3, 4, 5, 6, 7, 8A, 8B and 9.

Electronic Annex, Section 5. Determination of equilibrium mineral compositions in polymineralic systems, using an exchange model.

These models assume equilibrium between phases described by mineral/melt partition coefficients (D-values) as well as mass balance. Mass balance requires:

$$C_i^{bulk} = \sum Xj \cdot C_i^j \qquad [1]$$

where C_i^{bulk} is the concentration of element i in the bulk system, Xj = mass fraction of phase j, C_i^j is the concentration of element i in the jth phase, and the summation is over all j phases. Concentration ratios between phases are assumed to be given by mineral/melt D-value ratios:

$$C_i^j = C_i^{ref} \cdot D_i^j/D_i^{ref} \qquad [2]$$

where ref = any reference mineral (e.g., cpx or plag). Substituting expression [2] into [1] and rearranging gives:

$$C_i^{ref} = [C_i^{bulk}] \, / \, [X_{ref} + \sum Xj \cdot D_i^j/D_i^{ref}] \qquad [3]$$

for the concentration of element i in the reference phase. Once this is determined, the composition of any other phase can be calculated relative to the reference mineral using expression [2]. If the system is fully solidified, mass fractions correspond to the mineral modes. If the system is partly crystallized, mass fractions correspond to the solidified proportions of the minerals. If melt is one of the phases present, its composition is easily determined relative to the reference mineral by:

$$C_i^{melt} = C_i^{ref}/D_i^{ref} \qquad [4]$$

or by a similar expression using any other co-existing mineral.